# SPACE VARIANT GUIDED MODE RESONANCE FILTERS

by

Zachary Alexander Roth

A dissertation submitted to the faculty of
The University of North Carolina at Charlotte
in partial fulfillment of the requirements
for the degree of Doctor of Philosophy in
Optical Science and Engineering

Charlotte

2012

Approved By:

______________________________
Dr. Eric Johnson

______________________________
Dr. Menelaos Poutous

______________________________
Dr. Thomas Suleski

______________________________
Dr. Faramarz Farahi

______________________________
Dr. Edward Stokes

©2012
Zachary Alexander Roth
ALL RIGHTS RESERVED

# ABSTRACT

ZACHARY ALEXANDER ROTH, Space variant guided mode resonance filters. (Under the direction of DR. ERIC G. JOHNSON)

Guided mode resonance filters (GMRF) combine subwavelength gratings and planar slab waveguides to create highly efficient, narrow linewidth spectral filters. Resonances between diffracted orders of the SWG and the waveguide provide the mechanism for spectral filtering. These resonance conditions are dependent on all of the structural and optical parameters of the GMRF structure. Microfabrication technologies are routinely used to fabricate these types of micro-optical structures as well as other types of micro-optical components such as diffractive optical elements. A spatially and spectrally varying optical element can be realized by spatially varying one or more of the structural parameters of a standard GMRF structure. This dissertation will show different methods of achieving a spatially and spectrally varying GMRF. These types devices have applications as beam shaping elements, feedback elements is laser systems, and as an alternate to graded reflectivity mirrors. Unlike graded reflectivity mirrors, the spatial variation in these space variant GMRFs is not limited to axial symmetries. This dissertation will focus on space variant GMRFs through a spatially variation in the fill-fraction of the SWG lattice structure as well as a spatial variation of the waveguiding layer. It will be shown what the effect of each of these variations has on the resonance conditions of a GMRF. Proposed devices for a spatially varying waveguide structure using a silicon oxide SWG with a silicon nitride waveguiding layer and a silicon nitride SWG with a silicon nitride waveguide layer will be discussed.

# DEDICATION

*This dissertation is dedicated to my friends and family.*

# ACKNOWLEDGEMENTS

I would like to thank my advisor, Dr. Eric Johnson, for his support, guidance and wisdom during my career as a graduate student. He provided the funding support, the research opportunities, and access to state-of-the-art facilities that made this dissertation possible. I would also like to thank my committee, Dr. Menelaos Poutous, Dr. Thomas Suleski, Dr. Faramarz Farahi, and Dr. Edward Stokes, for their time and effort. I would like to thank all of the past and present members of the Micro-Photonics Laboratory. Without their assistance, training, and humor this would not have been possible. I would like to thank Dr. Poutous for sharing his knowledge and experience in micro-fabrication and optics. I would like to thank the staff of the Center for Optoelectronics and Optical Communications at the University of North Carolina at Charlotte for maintaining the equipment necessary for the research in this dissertation. I would like to thank the various agencies that provided funding for me: State of North Carolina (GASP Fellowships 2007-2011), the National Science Foundation, the Office of Naval Research, the High Energy Laser – Joint Tactical Office, Lockheed Martin, Northrop Grumman, the AFOSR, the Directed Energy Professional society (DEPS Fellowships 2008, 2008), and CREOL at UCF (Schwartz Fellowship 2004).

# TABLE OF CONTENTS

CHAPTER 1: INTRODUCTION AND BACKGROUND 1

1.1. Introduction 1

1.2. Guided Mode Resonance Filters 3

1.2.1. Theory of Guided Mode Resonances 3

1.2.2. Resonance Regimes 8

1.2.3. Effect of Structural Parameters on Resonance 10

1.2.4. Angle of Incidence Effects 22

1.2.5. Polarization Dependence 24

1.3. Applications of Guided Mode Resonance Filters 27

1.3.1. GMRFs as Feedback Elements in Laser Cavities 28

1.3.2. Space Variant GMRF for Phase Front Control 32

1.3.3. Additional Applications of GMRFs 34

1.4. Graded Reflectivity Mirrors 36

CHAPTER 2: FABRICATION METHODS 38

2.1. Introduction 38

2.2. Conventional Lithography 39

2.2.1. Photoresist Response 40

2.2.2. Contact Lithography 43

2.2.3. Projection Lithography 44

2.3. Additive Lithography 46

2.4. Analog Lithography 48

2.4.1. Phase Mask Fabrication 52

2.5. Transfer Etching 54

2.5.1. Selectivity 58

2.6. Material Deposition 59

2.7. 16-Level Optical Vortex 61

2.8. Variable Fill Fraction Periodic Structures 66

CHAPTER 3: FABRICATED DEVICES 70

3.1. Introduction 70

3.2. Conventional Guided Mode Resonance Filters 71

3.2.1. GMRFs for Operation near 1550 nm 71

3.2.1. Over-Coated GMRF for Operation near 980 nm 76

3.3. Variable SWG Fill Fraction Space Variant GMRF 80

3.3.1. Concept 80

3.3.2. Device Fabrication 85

3.3.3. Simulated Beam Profiles 90

3.3.4. Experimental Results 94

3.4. Variable Waveguide Thickness Space Variant GMRF 97

3.4.1. Motivation and Concept 97

3.4.2. Over-Coated Silicon Nitride on Fused Silica SWG GMRF 98

3.4.3. Silicon Oxide SWG with Silicon Nitride Waveguide Layer 103

3.4.4. Silicon Nitride SWG with Silicon Nitride Waveguide Layer 108

CHAPTER 4: CONCLUSION 113

BIBLIOGRAPHY 115

APPENDIX A: PARAMETERS OF VARIOUS FABRICATION PROCESSES 120

APPENDIX B: MATLAB CODE 123

# CHAPTER 1: INTRODUCTION AND BACKGROUND

## 1.1. Introduction

With the advent of microfabrication technologies in the last several decades, it has become possible to fabricate new types of optical elements. These elements can provide new, useful means of controlling light. Micro-optical elements have shown the ability to create arbitrary phase profiles in surface relief dielectrics. Other types of these structures have also been used to create spectral filters. In this dissertation, novel optical components are presented that exploit the properties of optically resonant structures to make an azimuthally varying spectral filter. The optically resonant structures used in this dissertation are known as Guided Mode Resonance Filters (GMRFs). Microfabrication techniques can be utilized not only to create these resonant structures, but also to vary the resonance conditions across a device to create a spatially and spectrally varying optical component.

GMRFs combine subwavelength gratings (SWGs) and slab waveguides to create a spectral reflection filter that can have an arbitrarily small linewidth [1]. The reflectance or diffraction efficiency of these devices changes rapidly over a small parameter change and was first noticed by Wood in 1902 [2]. Since Wood first noticed this “anomaly,” there has been significant research into this phenomenon, which can be described by two types. The first type was explained by Lord Rayleigh in 1907 [3], and occurs when diffraction orders appear and disappear. The second type, and the one which is most

relevant to this dissertation, was presented by Hessel and Oliner in 1965 [4]. They published a new theory that describes this spectral characteristic as a resonance between a guided mode and a diffracted order of a grating. Since then, there have been significant efforts to understand the properties GMRFs [1-12]. In the literature, they are also referred to as High Contrast Gratings, Subwavelength Resonance Gratings, Resonant Grating Filters, and Guided Mode Resonance Filters. Here they will be collectively referred to as guided mode resonance filters (GMRFs).

In this chapter, the theory of guided mode resonance filters (GMRFs) will be discussed. The effect of the various structural parameters of these devices on their spectral behavior will be described. In addition, some examples of the applications of GMRFs will also be covered. Graded reflectivity mirrors (GRM) will be the last topic covered in this chapter. Space variant GMRFs provide a potential new approach to the realization of GRMs, and this dissertation will show that space variant GMRFs are not limited to the same axial symmetry that GRMs are.

In Chapter 2, the microfabrication methods used to create these types of optical elements will be covered. The lithographic methods used to create the SWGs as well as the spatially variant structures necessary to achieve a space variant GMRF will be covered. In addition, the techniques used to transfer these patterns into different materials will be discussed. The technologies used to deposit and create the dielectric stacks that comprise the SWG and the waveguide layers of a GMRF will also be described.

Chapter 3 will focus on the concept, design, fabrication, and testing of various fabricated devices relevant to this body of work. The concept of space variant GMRFs

will be further explained, as well as experimental results. In addition, new approaches to creating spatially varying GMRFs will be covered.

## 1.2. Guided Mode Resonance Filters

### 1.2.1. Theory of Guided Mode Resonances

GMRFs are comprised of two main components: a subwavelength grating (SWG) and a waveguiding layer. When the resonance conditions of the GMRF are met, diffraction orders from the subwavelength resonance grating will couple to the guided modes of the waveguide, and subsequently re-couple towards the source. When the incident light does not meet these resonance conditions, the reflection and transmission are determined by the thin film properties of the structure. The period of the SWG is chosen such that all of the diffracted orders, except the $0^{th}$, are evanescent in air. The resonance condition for a GMRF occurs when the transverse propagation constant of a diffracted order from the SWG matches the propagation constant of a guided mode in the waveguide. Figure 1.1 depicts the cross section of a simple GMRF; the waveguiding region also doubles as the grating region, denoted by $\varepsilon_2$ in the figure.

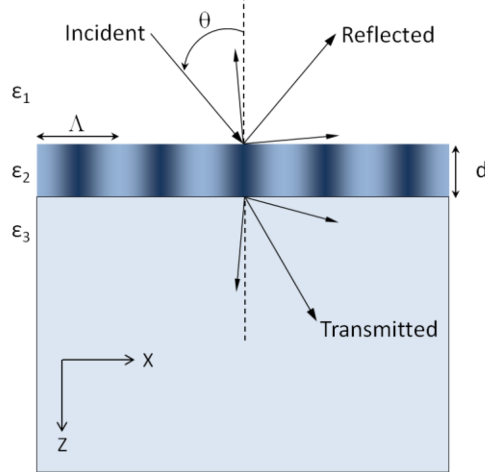


Figure 1.1. This schematic drawing of a 1D GMRF shows the relevant parameters. The TE points in the x-direction, normal to plane of incidence and perpendicular to the grating vector.

Consider the general case of light incident at an angle with multiple diffracted orders. The mathematical representation of the grating is described in Equation 1.1, where $\varepsilon_{wg}$ is the average index of the waveguide; $\Delta\varepsilon$ is the index contrast of the grating; and $\Lambda$ is the period of the grating. The grating is assumed to have a sinusoidal varying refractive index in this case. The permittivity of the superstrate, the region the light is incident from is given by $\varepsilon_1$, and the permittivity of the substrate is given by $\varepsilon_3$. The thickness of the grating is given by *d*. These optical and structural parameters fully describe the GMRF device shown in Figure 1.1.

$$\varepsilon_2 = \varepsilon_{wg} + \frac{\Delta\varepsilon}{2}\cos\left(\frac{2\pi}{\Lambda}x\right) \quad 1.1$$

Previously, the resonance condition was described as a phase matching between the diffracted orders of the grating with the guided modes of the waveguide. The spectral location of the resonance can be found by matching the transverse effective index of the diffracted order with the effective index of the guided mode. Equation 1.2 shows the dispersion relation for a diffraction grating of period $\Lambda$, diffraction order *m*, for refractive

index $n_{wg}$ in the material, and an angle of refraction θ' of the $0^{th}$ order [1]. From this, we can calculate an effective transverse refractive index of the diffracted order and is given by $n_{grat}=\beta_m/k$. Where

$$\beta_m = k(\sqrt{(\varepsilon_{wg})}\sin(\theta') - m\frac{\lambda}{\Lambda}) . \qquad 1.2$$

Equations 1.3 and 1.4 describe the Transverse Electric (TE) and Transverse Magnetic (TM) waveguide equations, respectively, for a non-periodic slab waveguide with thickness $d$, cladding permittivities $\varepsilon_1$ and $\varepsilon_3$, and core permittivity $\varepsilon_{wg}$. The parameters γ, δ, and κ are defined in Equations 1.5, 1.6, and 1.7, respectively. In these equations, β is the propagation constant of the guided mode and is related to the effective index of the guided mode by $\beta_m=k_o*n_{eff}$. It should be noted that the resonance location for this simple GMRF found using this method is not a function of the index contrast, Δε, of the grating.

$$\tan(\kappa d) = \frac{\kappa_m(\gamma-\delta)}{\kappa^2-\gamma\delta} \qquad 1.3$$

$$\tan(\kappa d) = \frac{\epsilon_{wg}\kappa(\epsilon_3\gamma-\delta)}{\epsilon_1\epsilon_3\kappa^2-\gamma\delta} \qquad 1.4$$

$$\gamma = \sqrt{\beta^2 - \varepsilon_1 k^2} \qquad 1.5$$

$$\delta = \sqrt{\beta^2 - \varepsilon_3 k^2} \qquad 1.6$$

$$\kappa = \sqrt{\varepsilon_{wg}k^2 - \beta^2} \qquad 1.7$$

As an example, consider the GMRF shown in Figure 1.1. Table 1.1 gives the structural and optical parameters used for the following calculations.

Table 1.1. Optical and structural parameters of single layer GMRF example

| Parameter | Value |
|---|---|
| $\varepsilon_1$ | 1.0 |
| $\varepsilon_3$ | 2.1437 |
| $\varepsilon_{wg}$ | 2.9969 |
| $\Delta\varepsilon$ | 0.2 |
| $\Lambda$ | 0.33 μm |
| d | 0.33 μm |

In order to find the location of the resonance for the TE case (the polarization parallel to the grating groves), Equation 1.3 must be solved for $n_{eff}$. MATLAB was used to find a numerical solution for $n_{eff}$ as a function of wavelength. The dispersion curve of the waveguide is shown in Figure 1.2 along with the dispersion curve for the grating; both dispersion curves are plotted as the effective index against the wavelength. The intersection of these two curves indicates when energy from the diffracted orders can couple into the leaky-mode of the waveguide. From this graph, the location of the spectral resonance is found to be approximately 541.7 nm.

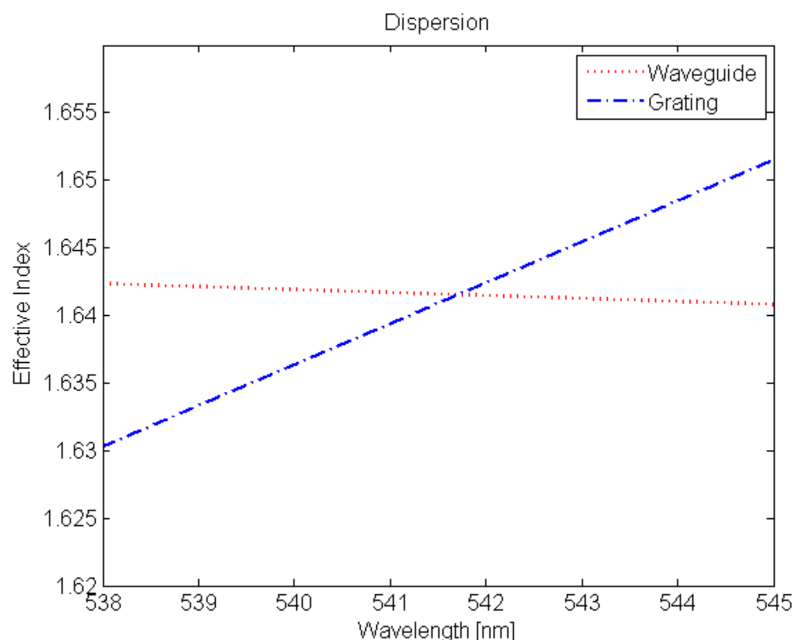


Figure 1.2. Dispersion relationship for the waveguide and grating of a simple GMRF. The intersection of the two curves shows the spectral location of the resonance

The resonance location found using this method is only an approximation because it assumes an average index for the core of the waveguiding region, and neglects the effects of the index contrast of the grating. This method provides only the resonance location, not the correlating linewidth, efficiency, nor the relative strength of the sidebands. In order to determine other characteristics of the resonance, Rigorous Coupled Wave Analysis (RCWA) will be used [13-15]. RCWA is a semi-analytical model used to analyze infinitely periodic, all dielectric structures. Furthermore, RCWA can model three dimensional vector fields incident at oblique angles on a periodic structure. The periodic structure and the incident field are decomposed into spatial harmonics and are solved as eigenvalue problems. A full description of the RCWA method is beyond the scope of this dissertation.

RCWA was utilized to simulate the structure shown in Figure 1.1. The structural parameters are the same as described above, in addition the index contrast, $\Delta\varepsilon$, is 0.2.

Results from the RCWA simulation are shown in Figure 1.3, along with the dispersion relationships. The simulations show the complete reflection spectrum and are not limited to an approximate resonance location. The predicted resonance is shown to be located at 541.5 nm, a difference of only 0.2 nm from the resonance condition found using the dispersion relations.

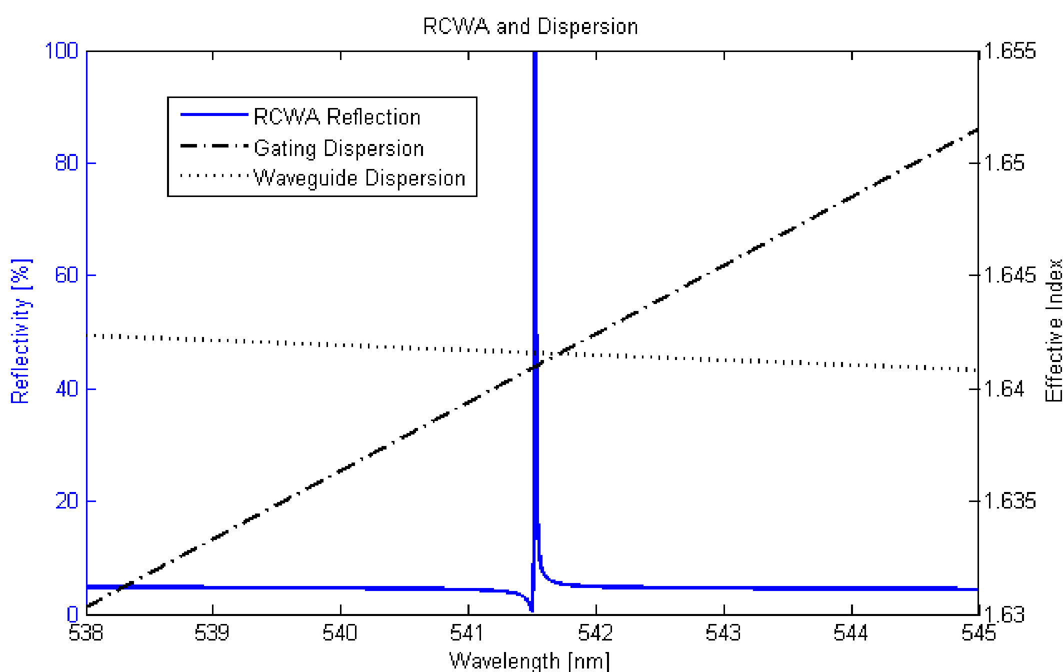


Figure 1.3. RCWA simulation results compared with theoretical resonance location. The axis on the left corresponds to the Reflectivity while the axis on the right corresponds to the effective index values. These are for the TE mode.

### 1.2.2. Resonance Regimes

Coupling between the diffracted orders of a SWG and the guided modes in a waveguide leads to restrictions as to where resonances can occur. For example, the effective index of a guided mode will lie between the refractive index of the core and the higher index value of one of the claddings. This relationship is shown in Inequality 1.8.

$$\mathrm{MAX}(\sqrt{\varepsilon_1}, \sqrt{\varepsilon_3}) \leq \mathrm{n_{eff}} \leq \sqrt{\varepsilon_{\mathrm{wg}}} \qquad 1.8$$

This inequality limits the allowed transverse propagation constants of the diffracted orders that can be coupled into the waveguide. If Equation 1.2 is solved in terms of the transverse effective index of the diffracted order and substituted into Inequality 1.8, a relationship between the allowed resonances can be achieved, as shown in Inequality 1.9. In the case of normally incidence light for a GMRF with an air superstrate, the period must lie between $\lambda/n_3$ and $\lambda/n_{wg}$.

$$\mathrm{MAX}(\sqrt{\varepsilon_1}, \sqrt{\varepsilon_3}) \leq \left| \sqrt{(\varepsilon_{wg})} \sin(\theta) - m\frac{\lambda}{\Lambda}) \right| \leq \sqrt{\varepsilon_{\mathrm{wg}}} \qquad 1.9$$

Using Inequality 1.9, the resonance regime across angle of incidence and wavelength can be determined. These results are shown in Figure 1.4. The shaded regions are where resonances are allowed to occur. The blue shaded region represents resonances occurring from the -1 diffracted order, and the red shaded region represents resonances from the +1 diffracted order. The dashed lines represent the curve created when the left hand side of Inequality 1.9 is solved for λ, and the period is kept constant. The solid lines represent the curve created when the same process is applied to the right hand side.

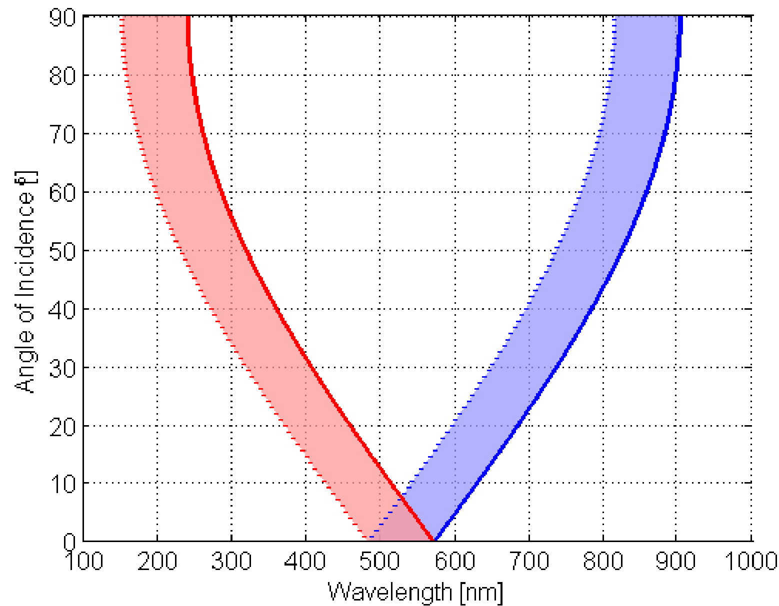


Figure 1.4. Resonance regime for the GMRF described above. The shaded regions represent the range of parameters where resonances can occur. This resonance regime is for a structure with a waveguide permittivity, $\varepsilon_{wg}$, of 2.9969; a substrate permittivity, $\varepsilon_3$, of 2.1437, and a period 0.33 µm. The red shaded region represents the -1 diffracted order, and the blue shaded region represent the +1 diffracted order.

Furthermore, Figure 1.4 illustrates that as the angle of incidence is increased, there is a rapid change in the resonance regime. It should be noted that at normal incidence, the resonance regime is the same for both the +1 and -1 diffracted orders, which is expected considering they will have the same internal angle within the GMRF structure.

### 1.2.3. Effect of Structural Parameters on Resonance

In the previous section, the resonance conditions and resonance regimes of a GMRF were discussed. However, this is not a full description of the spectral behavior of these devices; the spectral characteristics of a GMRF are largely dependent on all the structural parameters and optical material properties of the device. The sensitivity of GMRFs to the various structural and optical parameters has been exploited to create

various types of GMRFs where the resonance condition can be tuned by modifying one or more of these parameters [16-19]. RCWA will be used to investigate the effect of these structural parameters on the spectral characteristics of the GMRF.

The GMRF structure described in the example above is sufficient to explain the theory behind the operation of GMRF's; however, fabricating the structure is difficult. Therefore, it is more advantageous to discuss the spectral characteristics of a device that can be fabricated. Figure 1.5 depicts the one-dimensional GMRF schematic that will be used for the remainder of this section. This GMRF consists of a one dimensional binary SWG on a waveguiding layer. In addition, the refractive index values that will be used will correspond to materials that will be used later in this dissertation.

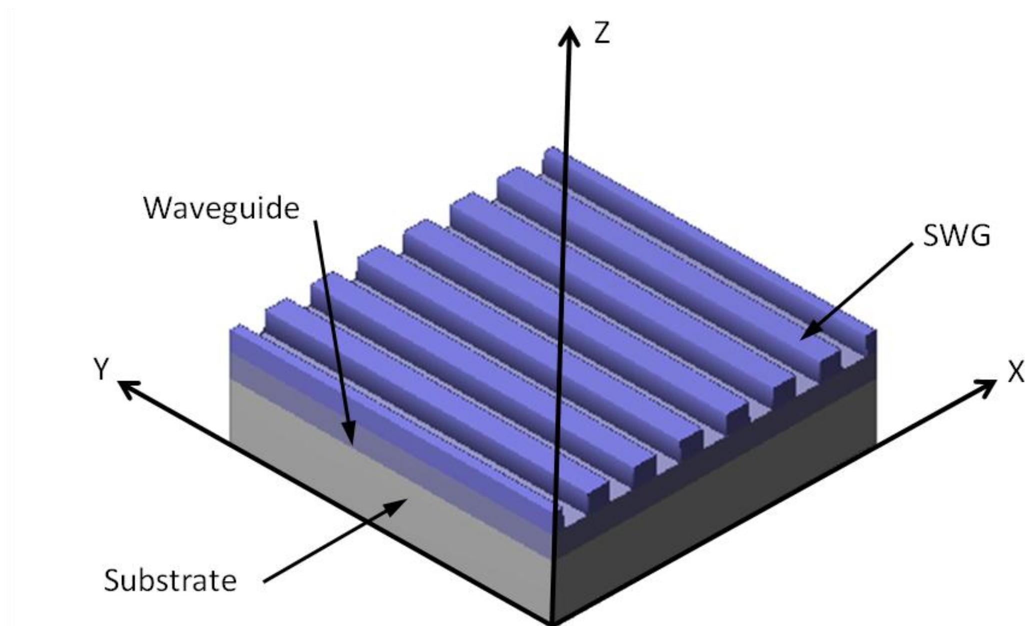


Figure 1.5. Schematic drawing of a 1D GMRF

Table 1.2 lists the materials and refractive indices used for the one dimensional GMRF shown in Figure 1.5. These refractive index values are for a wavelength of 1550 nm, and resonance conditions around 1550 nm will be discussed.

Table 1.2. Materials used in 1D GMRF simulations

| Layer | Material | Refractive Index |
|---|---|---|
| SWG | Silicon Oxide ($SiO_x$) | 1.4592 |
| Waveguide | Silicon Nitride ($Si_xN_y$) | 1.9489 |
| Substrate | Fused Silica | 1.4433 |

Using the values in Table 1.2 and the relationships described in Inequality 1.9, we can determine the resonance regimes of the angle of incidence and the SWG period for a constant wavelength. Figure 1.6 shows the resonance regimes of the period and angle of incidence for the materials in Table 1.2 and a wavelength of 1550 nm. From this figure, it can be determined that at normal incidence resonances can occur at 1550 nm for gratings with periods ranging from 795 nm to 1075 nm.

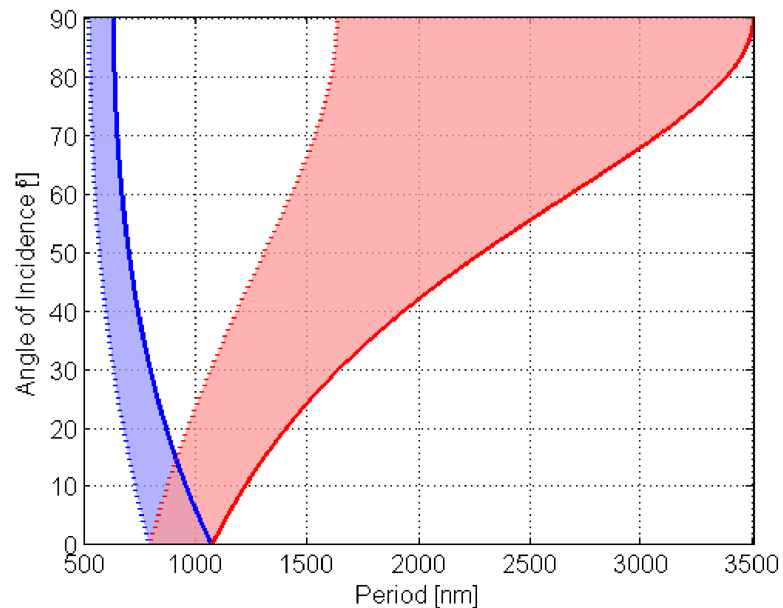


Figure 1.6. Period and Angle of Incidence resonance regime for a wavelength of 1550 nm and for an Air, Silicon Nitride, and Fused Silica material system

From Figure 1.6, a suitable period can be chosen to begin the simulations. A period of 1.0 μm is chosen as an initial value for the following discussion. This value was chosen, because if this GMRF were to fabricated it would be advantageous to choose the largest 'round' period possible. The first structural parameter to be investigated is the thickness of the waveguiding layer. Figure 1.7 displays the results from the RCWA simulations. The waveguiding layer was varied between 200 nm and 500 nm, while the SWG thickness and duty cycle were kept constant at 500 nm and 50%, respectively. Both the TE (parallel to the groves) and the TM (parallel to the grating vector) polarizations are considered.

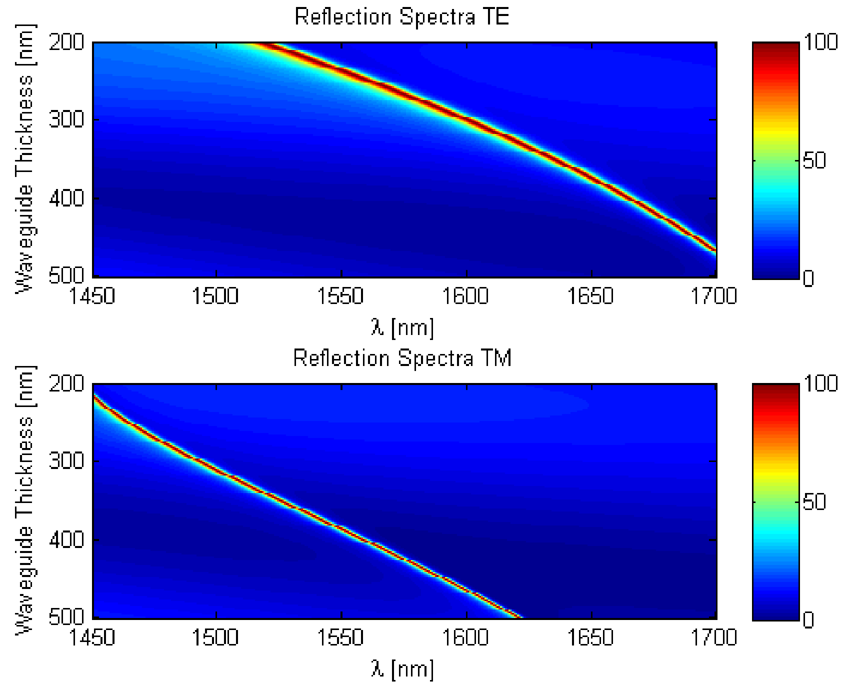


Figure 1.7. RCWA simulation results for a 1D GMRF. The Thickness in the waveguiding layer is varied between 200 nm and 500nm. The period is 1.0 µm, and the SWG is 500 nm thick with 50% duty cycle.

. From Figure 1.7, it can be seen that the resonance will red-shift as the waveguide thickness increases. An increase in the thickness of the core of a waveguide will cause the effective index of the guided modes to decrease. This, in turn, will cause the resonance to red-shift in order to match the SWG dispersion. From these graphs, it can be shown that a variation of approximately 300 nm of waveguide thickness will result in approximately 300 nm of resonance shift.

Also, notice that there is a minimum in the sidebands (off resonance wavelengths) at 1550 nm when the waveguide thickness is approximately 400 nm. The side band reflection and transmission values are strongly dependent on the thin film stack that comprises a GMRF. The waveguide layer is between two lower index materials, and when it is at a value of $\lambda/(2n_{wg})$, it will dampen the reflection from the thin film stack; for

silicon nitride, this corresponds to a thickness of 397 nm. This illustrates that careful selection of the thin film thicknesses can increase the suppression of the sidebands in the reflection spectrum.

Figure 1.8 shows the linewidth of the resonances shown in Figure 1.7. The linewidths are measured at the Full Width Half Maximum (FWHM) of the resonance peak. In this figure, when the linewidth falls to zero, it corresponds to resonances that fall outside of the simulation window of 1450 nm to 1700 nm. This figure shows that for the TM polarization linewidth change is small over the simulation window.

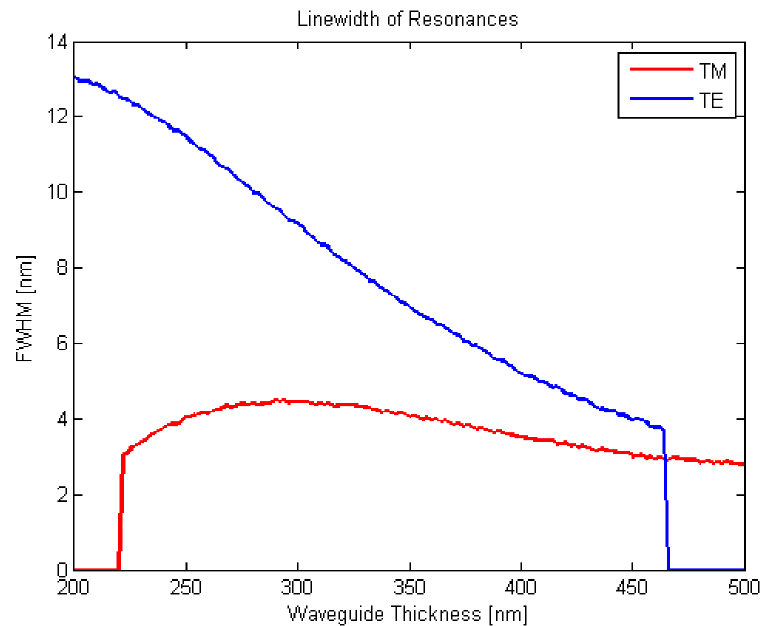


Figure 1.8. Linewidth variation of a 1D GMRF as a function of waveguide thickness. Linewidths corresponding to 0 nm are from resonances outside the simulation domain of 1450 n to 1700 nm wavelength. The Thickness in the waveguiding layer is varied between 200 nm and 500nm. The period is 1.0 µm, and the SWG is 0.5 µm thick with 50% duty cycle.

The SWG forms a portion of the upper cladding of the waveguide in the GMRF, and as such, variations to its structural parameters will affect the spectral characteristics

of the resonance. Figure 1.9 displays the RCWA results from varying the SWG thickness between 50 and 700nm. For this structure, the period is still 1.0 μm; the duty cycle is 50%; and the waveguide is 400 nm thick. This figure shows that after the thickness of the SWG approaches approximately 400 nm, further increases in the thickness has a limited effect on the resonance in terms of linewidth and spectral location. As the SWG thickness is increased, the effect it has on the guided mode diminishes.

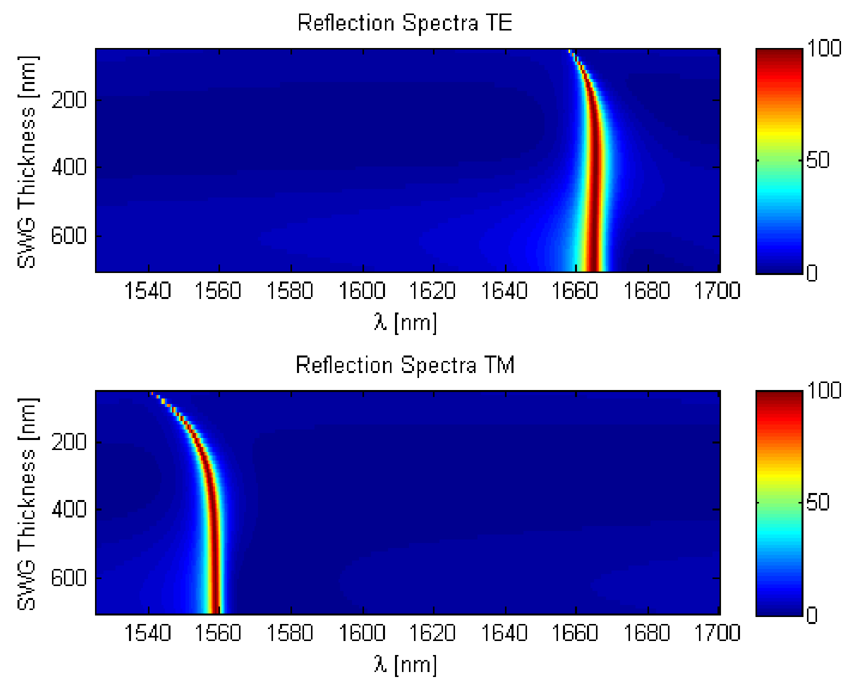


Figure 1.9. RCWA simulation results for a 1D GMRF. The thickness of the SWG is varied between 50 nm and 700nm. The period is 1.0 μm, and the SWG has a 50% duty cycle and the waveguiding layer is 400 nm thick.

For example, consider a SWG that has sufficient thickness such that the evanescent tail of the guided mode vanishes completely within the SWG. If the SWG thickness is increased beyond this point, it will have no effect on the guided mode conditions; the cladding of the waveguide is comprised of only the SWG at this point.

Below this thickness, the cladding of the waveguide will be comprised of the SWG and the air superstrate. When the SWG thickness is varied within this regime, the cladding conditions will also vary, leading to a variation the guided mode properties. When the SWG thickness increases to the point that it becomes the entire cladding; further increases in SWG will not affect the resonance behavior, and the air superstrate has become decoupled from the GMRF device.

Figure 1.10 shows that as the thickness of the SWG approaches zeros, so does the linewidth. This occurs because as the SWG thickness goes to zero the conditions for resonance vanish. At very small SWG thicknesses, the resonance conditions still exist; which implies that a highly efficient reflection should still occur [1]. For the reflection peak to vanish as the SWG vanishes, then the linewidth of the device needs to vanish as well. This linewidth behavior can be expected to occur over any structural or optical parameter that would cause the SWG to vanish. While the effect of the SWG has some influence on the resonance conditions, it has a larger effect on the control of the linewidth of the resonance.

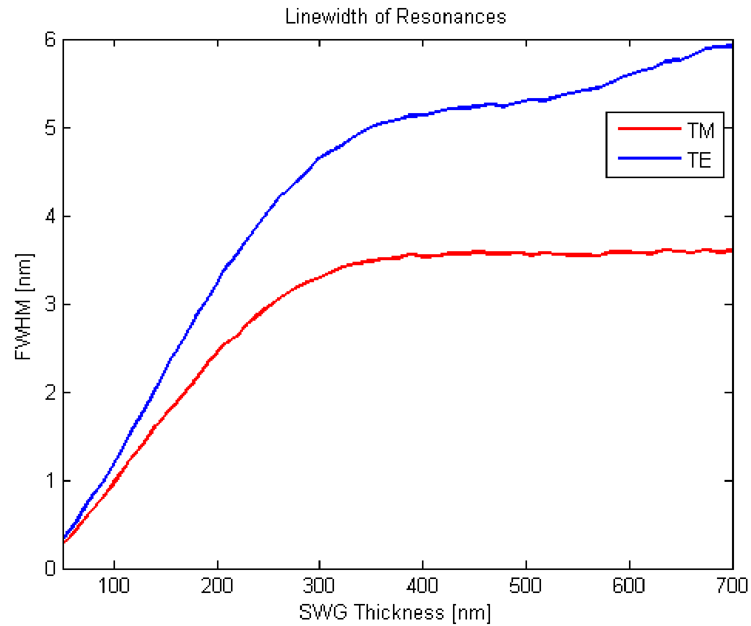


Figure 1.10. Linewidth variation as a function of SWG thickness. The thickness of the SWG is varied between 50 nm and 700nm. The period is 1.0 µm, and the SWG has a 50% duty cycle and the waveguiding layer is 400 nm thick.

Figure 1.11 shows the simulation results for a variation in the duty cycle of the SWG between 10% (0.1) and 90% (0.9). For these simulations, the SWG period is 1.0 µm; the SWG and waveguide layer thicknesses are 500 nm and 400 nm, respectively. Because the SWG forms, at least, a portion of the cladding of the waveguide, variations in the duty cycle of the SWG will affect the effective index of the cladding region and thus lead to a change in the resonance conditions. These simulations show that the effect of the SWG duty cycle variation on the location of the resonance is much smaller than that of the waveguide thickness variation.

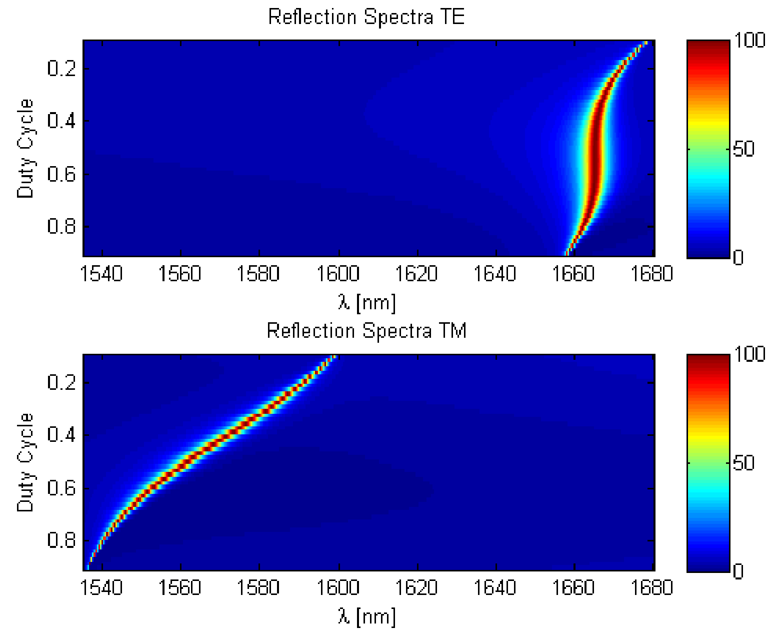


Figure 1.11. RCWA simulation results for a 1D GMRF. The duty of the SWG is varied between 10% and 90%. The period is 1.0 µm, and the SWG and the waveguiding layer are 500 nm and 400 nm thick, respectively.

Figure 1.12 shows the linewidth variations that occur when the duty cycle of the SWG is changed. As with the variation in the SWG thickness, as the duty cycle approaches 0% or 100% the structure approaches one without resonances conditions. This causes the linewidth of the resonance to decrease as the duty cycle approaches 0% or 100%. This figure shows that it is possible to reduce the linewidth approximately 80% for the TE case and 75% for the TM case. The simulation results from the variations in the SWG thickness and the SWG duty cycle imply that there is a maximum linewidth that can be achieved with this material system and general GMRF structure.

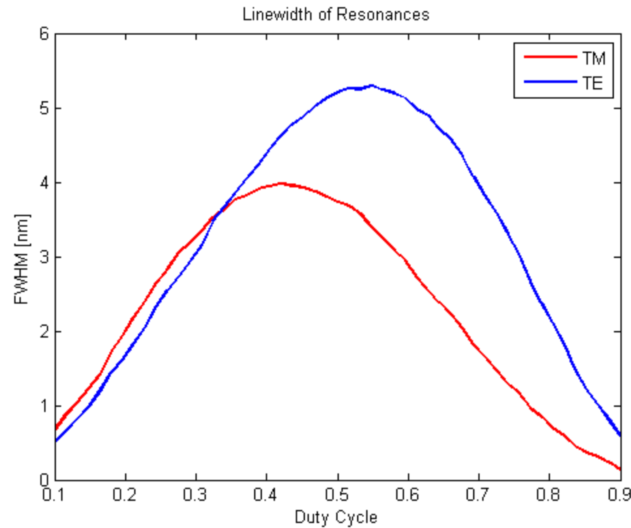


Figure 1.12. Linewidth variation as a function of the duty cycle of the SWG. The duty of the SWG is varied between 10% and 90%. The period is 1.0 µm, and the SWG and the waveguiding layer are 500 nm and 400 nm thick, respectively.

Figure 1.13 shows the results of the simulations that vary the period of the SWG. The period is varied between 900 nm and 1050 nm. The resonance varies linearly with the SWG period, and approximately 175 nm of resonance shift occurs.

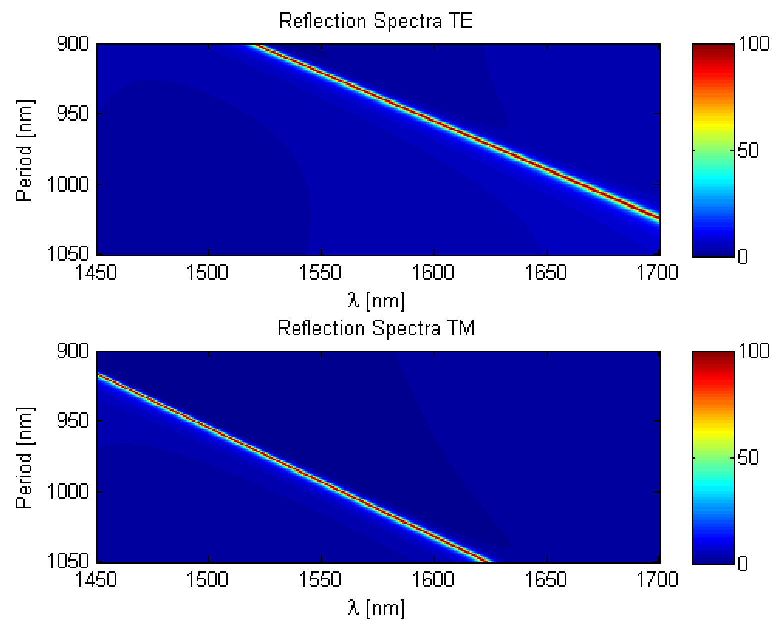


Figure 1.13. RCWA simulation results for a 1D GMRF. The period SWG is varied between 900 nm and 1050 nm. The duty cycle is 0.5%, and the SWG and the waveguiding layer are 500 nm and 400 nm thick, respectively

As stated previously, the resonance condition is a matching between propagation constants associated with the SWG and the waveguide. The structural parameters discussed previously only altered the resonance conditions by changing the properties of the guided modes. The period of the SWG is the only structural parameter to affect the resonance conditions by altering the propagation constant of the diffracted orders.

Figure 1.14 shows the spectral response for a 1D GMRF for the TE and TM polarization states. Table 1.3 lists the structural parameters of this design. This figure shows that the TE polarization has a resonance located at 1665 nm with a linewidth of 5.3 nm, and the TM polarization resonance is located at 1559 nm with a linewidth of 3.6 nm. The sideband level for the TM polarization is approximately 2.9% and the level for the TE case is approximately 4.5%

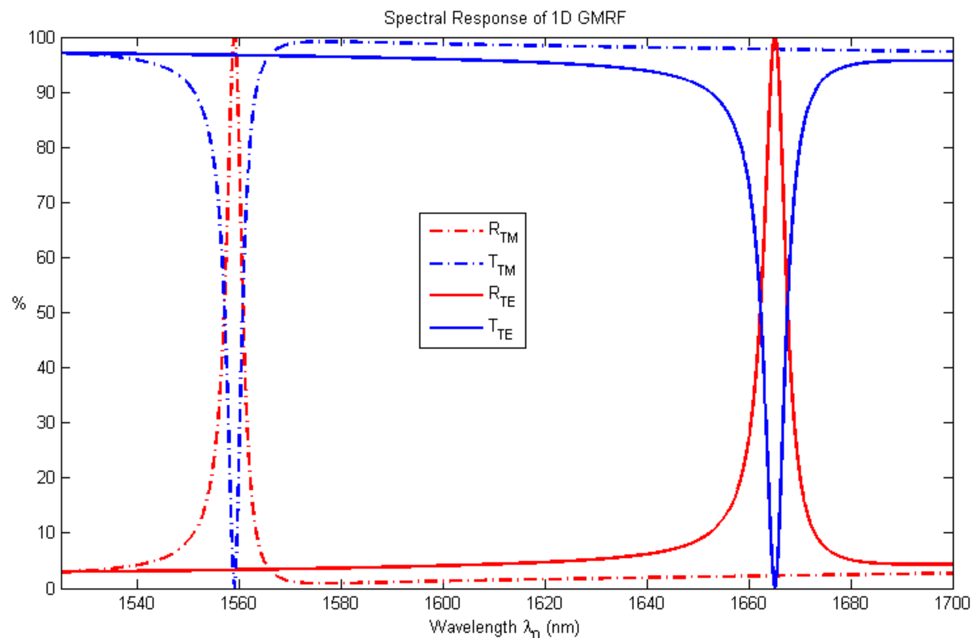


Figure 1.14. RCWA simulation results for a 1D GMRF. The period SWG is 1.0 µm with a duty cycle is 50%, and the SWG and the waveguiding layer are 500 nm and 400 nm thick, respectively

Table 1.3. Structural parameters of 1D GMRF used in the simulation.

| Parameter | Value |
|---|---|
| $d_{WG}$ (Waveguide Thickness) | 400 nm |
| $d_{SWG}$ (SWG Thickness) | 500 nm |
| $\Lambda$ (SWG Period) | 1.0 µm |
| Duty Cycle | 50% |

Of all the structural parameters considered, it is the period of the SWG that will limit the wavelength range that can contain a resonance. Oftentimes, the period of the SWG is the first structural parameter to be considered when designing a GMRF. These simulations show that the SWG period and the waveguiding layer thickness can be used in conjunction to roughly place a resonance location. The SWG thickness and the SWG duty cycle can be used reduce the linewidth and tune the resonance location. The layer thicknesses and SWG duty cycle can be varied to achieve the desired sideband levels, if necessary. All of the structural parameters must be considered when designing a GMRF; this often requires an iterative process to balance these structural parameters to achieve the desired spectral characteristics. When fabrication tolerances and limitations are also considered, the difficulty of designing a GMRF can increase. In response to this, researchers have begun to turn to more sophisticated modeling techniques in order to easily explore the parameters of any general structural design [20]. These techniques were not used in this research.

1.2.4. Angle of Incidence Effects

The previous simulations were all performed with the incident field at normal incidence to the GMRF. It is important to note that, while a specific angle of incidence is considered when designing and using a GMRF, the overall spectral change as a function angle of incidence should not be overlooked. Equation 1.2 shows that the transverse

propagation constant of the diffracted orders is also a function of the angle of incidence, and it can be expected that the spectral response of a GMRF will be highly dependent of the angle at which the incidence plane wave illuminates the device. Researchers have exploited this relationship to create tunable GMRFs [21, 22]. Figure 1.15 illustrates the simulated spectral response of the GMRF describe in Table 1.3. The angle of incidence is varied in the XZ plane (see Figure 1.5), the plane perpendicular to the grating grooves. These simulations show that for a few degrees off normal incidence, the spectral response of a GMRF changes rapidly. The resonance not only shifts rapidly, but additional resonances also develop. These additional resonances are created when the positive and negative diffractive orders have different propagation constants away from normal incidence and each one satisfies the resonance conditions at different wavelengths.

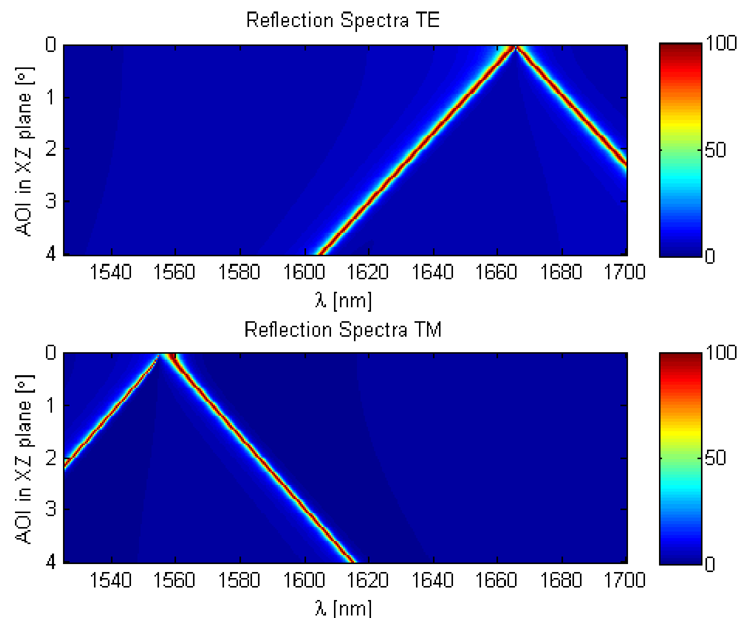


Figure 1.15. RCWA simulation results for a 1D GMRF. The angle of incidence is varied in the XZ plane between $0^{o}$ and $4^{o}$. The structural parameters are listed in Table1.3

The variation in resonance conditions with the angle of incidence creates practical concerns for the implementation of GMRFs in an optical system. The simulations show

that the alignment, for this structure, between the incident light and GMR will be extremely sensitive. This can be a limiting factor in some applications, and researchers have studied solutions to the problem of the strong angular intolerance of GMRF's [23-25].

1.2.5. Polarization Dependence

The polarization dependence of the 1D GMRF can be explained by coupling of the incident TE and TM fields to TE and TM guided modes. While it is expected that the propagation constant for the TE and TM diffracted orders be similar, orthogonal guided mode polarizations typically have different propagation constants and mode profiles. It is also possible to explain the polarization dependence from a structural symmetry standpoint. The structure of the 1D grating shown above has only $180^0$ symmetry and each orthogonal polarization "sees" a different structure. If a structure had symmetry such that both the orthogonal polarizations could not be discerned from each other in any meaningful way, then that structure could be said to be polarization independent. This applies to normally incidence light. For example, take the 2D GMRF shown in Figure 1.16. At normal incidence, there is no discernible difference in the structure between the two orthogonal polarization states. This leads to a polarization independent response at normal incidences.

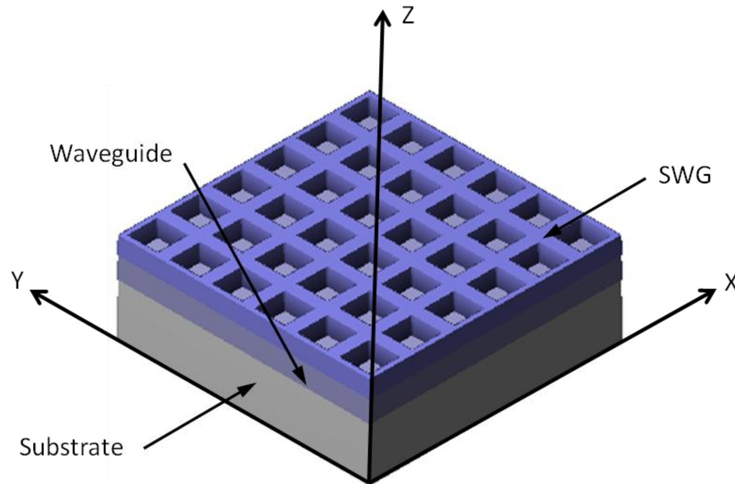


Figure 1.16. Schematic drawing of a 2D GMRF

Figure 1.17 shows the simulation results for the 2D GMRF shown in Figure 1.16. The layer thicknesses and SWG period are the same for the 1D case described in Table 1.3. The SWG period is the same in the X and Y directions. The fill fraction of the SWG was chosen to match the duty cycle of the 1D GMRF; the fill fraction of the SWG is 50% which corresponds to openings 707 nm wide in the X and Y directions. Figure 1.17 shows that the spectral response for this structure is polarization independent at normal incidence. If this response is compared to the spectral response of a 1D GMRF shown in Figure 1.14, it shows that both incident polarization states will couple to both orthogonal polarization states in the waveguide. There are resonances that occur at 1560.8 nm and 1669.5 nm with linewidths of 0.68 nm and 2.29 nm, respectively. The 2D GRMF has resonances that occur in roughly the same locations as the TM and TE 1D GMRF resonances, respectively (see Figure 1.14).

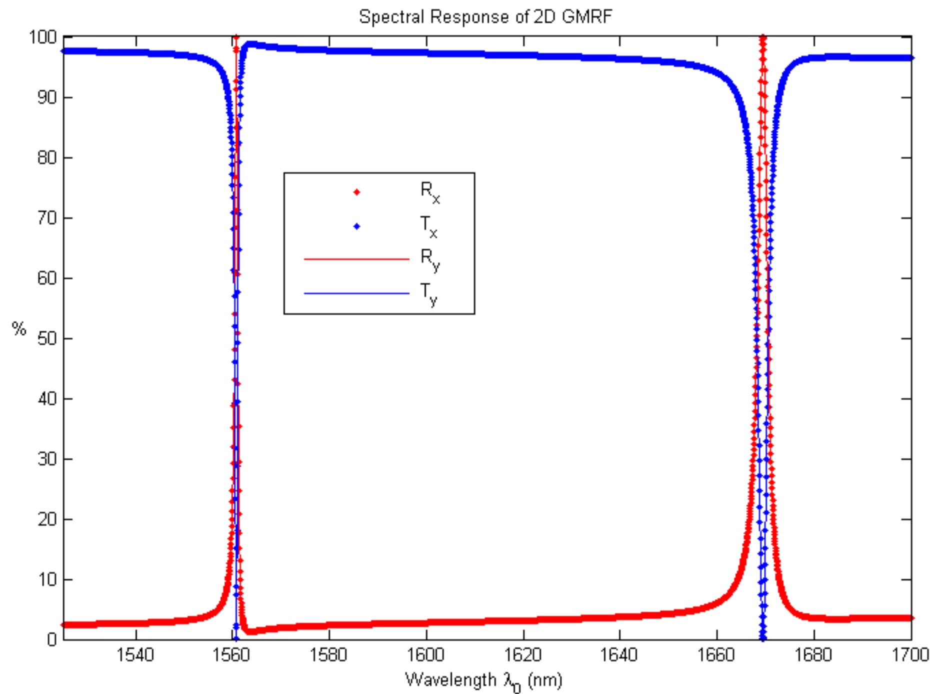


Figure 1.17. RCWA simulation results for a 2D GMRF. The period SWG is 1.0 μm in both X and Y directions with a fill fraction of 50%, and the SWG and the waveguiding layer are 500 nm and 400 nm thick, respectively. The reflection and transmission spectra shown here are polarization independent.

The effect of SWG symmetry on the polarization dependence of the GMRF can be further explored. While the previous 2D SWG had $90^0$ rotational symmetry, there are other symmetries that will also result in a polarization independent response at normal incidence. Consider the lattice structure shown in Figure 1.18. This is an example of a hexagonal lattice with circular openings. An opening in a hexagonal lattice will have the nearest openings occurring every $60^0$ and at the same distance from its center. The distance between these nearest neighbors is referred to as the lattice constant of the grating. This pattern creates a lattice symmetry such that if the lattice is rotated $60^0$ is will be an exact copy of the original. Thus, it can be expected that any two polarizations states that are rotated by $60^0$ will have identical spectral responses. These two polarization states are presented by vectors **A** and **C** in Figure 1.18. Furthermore, vector

**C** can be decomposed into the two orthogonal vectors **A** and **B**, and thus so can its spectral response. Therefore, if vectors **A** and **C** have the same resonance conditions then so must vector **B**. This results in creating a SWG lattice that is polarization independent at normal incidence [26, 27].

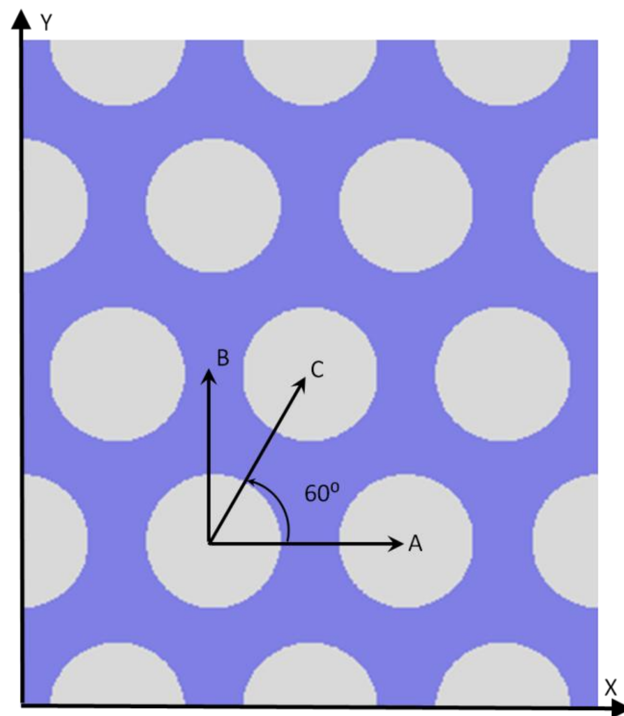


Figure 1.18. Hexagonal SWG showing different polarization states. Polarizations A and C will have the same resonance conditions and as a result, so will B.

## 1.3. Applications of Guided Mode Resonance Filters

The previous section focused on the theory and behavior of GMRFs. These types of wavelength filters can have several different applications depending on which of the properties of the GMRF are exploited. For example, laser systems could take advantage of the spectral response; the sensitivities to certain structural and optical parameters could

lead to new types of sensors; and the polarization response could be exploited for polarization filtering applications.

### 1.3.1. GMRFs as Feedback Elements in Laser Cavities

The spectral properties of GMRFs make them ideal for use in laser cavities. They can operate with very high reflectivities, narrow linewidths, and low sidebands. These characteristics make them highly useful in optical systems where wavelength stability is a priority. A GMRF can be used to replace a highly reflective mirror while simultaneously providing wavelength filtering.

The first reported use of GMRF as a feedback element in a laser system was by Mehta et al. in 2007 [28]. In this application, the GMRF was used as a spectrally selective feedback element in a fiber laser system operating near 1550 nm, in the c-band (1530 nm to 1565 nm). The gain material used was an Ytterbium/Erbium doped double cladding fiber. The fiber laser was optically pumped using a fiber pigtailed diode laser operating at 973 nm and coupled into the outer cladding of the fiber gain material. Figure 1.19 is a schematic representation of the fiber laser set up. The GMRF was operated in free-space, and the spectral characteristics allowed it to transmit the pump wavelength. This setup allowed the collimating or coupling optics to be used for both the GMRF retro-coupling and the pump coupling.

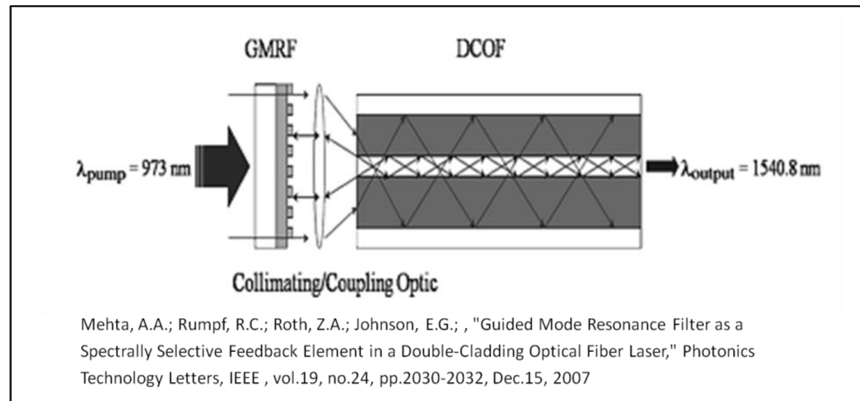


Mehta, A.A.; Rumpf, R.C.; Roth, Z.A.; Johnson, E.G.; , "Guided Mode Resonance Filter as a Spectrally Selective Feedback Element in a Double-Cladding Optical Fiber Laser," Photonics Technology Letters, IEEE , vol.19, no.24, pp.2030-2032, Dec.15, 2007

Figure 1.19. Schematic drawing of application of GMRF as a feedback mirror in a fiber laser operating in the C-band. [28]

The GMRF used in this system had a hexagonal lattice, for polarization independent reflection and transmission properties. Figure 1.20 shows a schematic of the GMRF used in the fiber laser, while Table 1.4 lists the specific structural parameters of the GMRF.

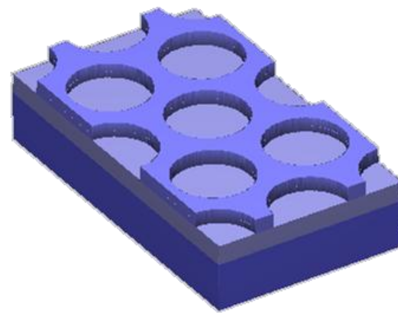

Figure 1.20. three-dimensional drawing of a hexagonal GMRF structure used in 1550 nm fiber laser.

Table 1.4. Structural parameters of GMRF used in [28].

| Parameter | Value |
|---|---|
| $d_N$ | 345 nm |
| $d_O$ | 245 nm |
| $d_E$ | 270 nm |
| Λ | 1.15 μm |
| D | 0.7 μm |

Figure 1.21 shows the simulated spectral response of the GMRF and Figure 1.22 shows the output of the fiber laser with the GMRF as a spectrally selective feedback element. Figure 1.21 shows that the expected resonance peak is located at 1540.8 nm which agrees with the measured spectral out of the fiber laser of 1540.8 nm shown in Figure 1.22.

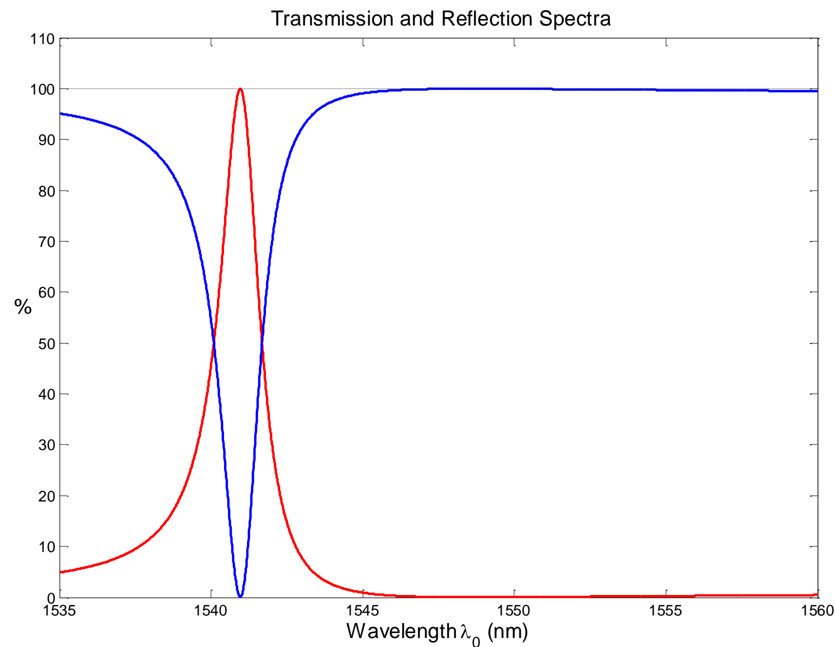


Figure 1.21. RCWA Simulation of GMRF used in 1550nm fiber laser. The blue curve is the transmission spectra and the red curve is the reflection spectra. [28]

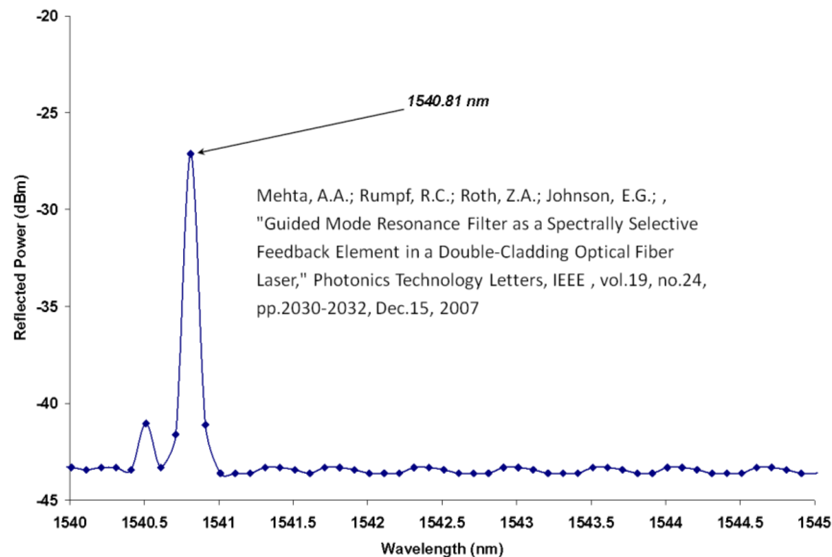


Figure 1.22. Experimental characterization of GMRF in fiber laser. [28]

The authors demonstrated that a GMRF was capable of providing wavelength stabilization of the fiber laser. This is accomplished by having highly efficient reflections, with low sidebands. A narrow linewidth reflection peak caused selective feedback of a narrow range of longitudinal cavity modes, providing wavelength stabilization. Output power of 900 mW at 1540.8 nm with a 0.18 nm linewidth was achieved using a GMRF as a spectrally selective feedback element.

Fiber laser systems operating near a 2.0 μm wavelength using GMRF as a wavelength stabilizing feedback mirror have also been demonstrated [29-31]. The gain material for this laser system is Thulium based. In this system, the fiber is, again, optically pumped. However, the pump light and the GMRF feedback element are on opposite ends of the laser cavity. The GMRF used in this system is similar in structure to the one shown in Figure 1.20. It uses a hexagonal lattice with a silicon oxide, silicon

nitride, and fused silica material system. The structural parameters of this GRMF are listed in Table 1.5.

Table 1.5. Structural parameters of the GMRF used for the 2.0 μm fiber laser

| Parameter | Value |
| --- | --- |
| $d_N$ | 540 nm |
| $d_O$ | 130 nm |
| $d_E$ | 130 nm |
| $\Lambda$ | 1.514 μm |
| D | 1.0 μm |

1.3.2. Space Variant GMRF for Phase Front Control

Previously, the resonance condition as a function of different structural parameters has been discussed. It was shown that the amplitude of the reflectivity or transmissivity of a GMRF will change rapidly across a resonance; in addition to this, the phase of the reflectivity or transmissivity can also change rapidly across a resonance. Normally, this will add a piston phase to the wavefront of the incoming wave. However, researchers have experimented with creating GMRFs with high index space variant structures to exploit properties of this effect [32, 33]. Their use of high index contrast SWGs creates a device with large linewidth resonances. Fattal et al. designed a GMRF on a fused silica substrate with a 1D SWG that went completely through a silicon dioxide and a silicon layer. Figure 1.23 shows the simulated reflection spectrum for TM polarized light at normal incidence; this simulation is of a structure similar to the one discussed in [32]. The SWG period is 650 nm with a 50% duty cycle; the silicon layer is 450 nm; and the silicon dioxide layer is 100 nm and lies on top of the silicon layer. Figure 1.23 also shows the phase change upon reflection from the GMRF. The resonance shown in this figure shows a linewidth with a FWHM of approximately 500 nm. It also shows the phase variation of the reflected light across the resonance.

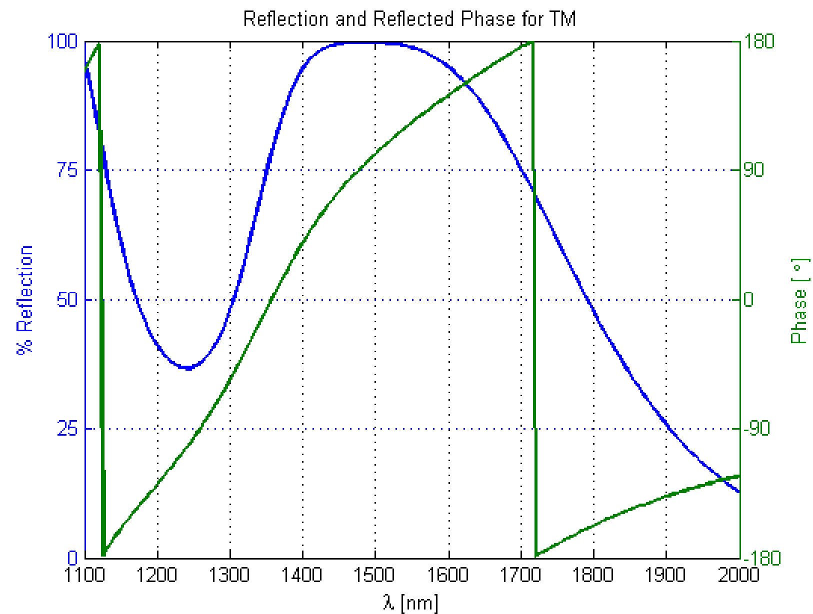


Figure 1.23. RCWA simulation results for a 1D GMRF. The period SWG is 0.65 μm in the X direction with a duty cycle of 0.5. The SWG is completely through a 100 nm Silicon Oxide layer and a 450 nm Silicon layer. The substrate is fused silica.

Figure 1.24 shows the variation in the reflectivity as well as the phase as function of both duty cycle and wavelength. The structure is the same as that of the previous figure. This shows that nearly $2\pi$ radians (rad) of phase change can occur across a resonance by varying only the duty cycle. Researchers have exploited this by slowly varying the duty cycle of the GMRF across the device area. This results in an optical element with a spatially varying phase.

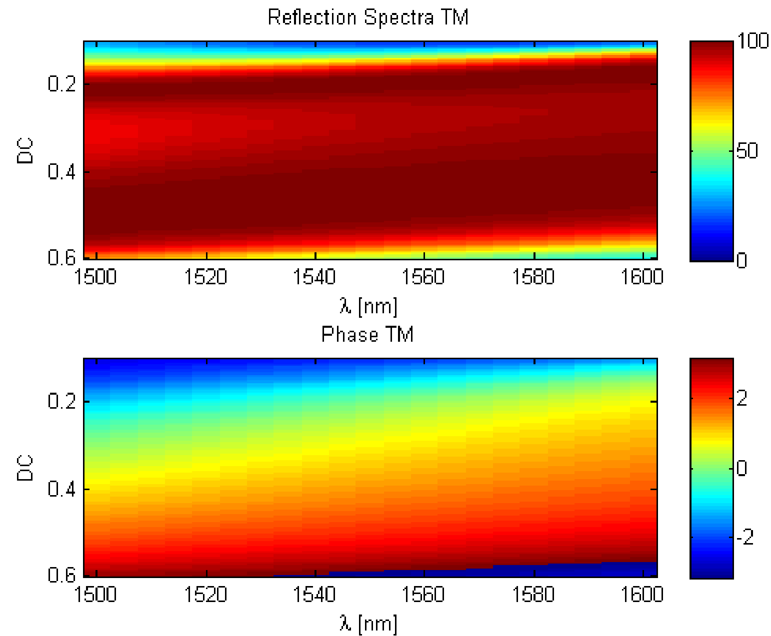


Figure 1.24. RCWA simulation results for a 2D GMRF. The period SWG is 0.65 µm in the X direction with a duty cycle varying from 0.15 to 0.6. The SWG is completely through a 150 nm Silicon Oxide layer and a 450 nm Silicon layer. The substrate is fused silica.

Fattal et al. demonstrated a space variant GMRF with a phase modulation that approximated a 20 mm focal length lens [32]. The authors measured the efficiency between 80% and 90%. Lu et al. used a similar method to design a lens with a numerical aperture of 0.86 and 0.96 with expected losses of 0.3 and 0.2 dB, respectively [33]. These researches designed a device using non-periodic high contrast gratings (HCG), where the period and the duty-cycle of the gratings were spatially varied.

1.3.3. Additional Applications of GMRFs

It has already been shown that the spectral characteristics of GMRF's can be used by laser systems, but there are other properties of GMRF's that can be exploited in other applications [34]. For example, researchers have used the angular dependence of GMRFs to create a tunable reflection filter that can be used in telecommunications applications [21]. The GMRF is designed to operate in the c-band, (1530 nm to 1565

nm) at angle of incidences around $45^0$. The resonance of the GMRF, in this application, is tuned by changing the angle of incidence that the source makes with the device. This has the effect of "dropping-out" different wavelengths from the source at different angles. The GMRF can be designed to have very low reflection at non-resonant wavelengths, which makes this a good candidate in optical telecommunication systems. The device can function as a tunable 'add/drop' component.

GMRFs can be used in other ways for optical switching. For example, if one of the materials used in the GMRF is a non-linear material it can be used as an optical switch. In Boye et al., they study the effect of using a non-linear material for the waveguide layer of a GMRF [35]. The authors simulate the effects of using a semiconductor-doped glass as the waveguide material, and show that when the incident power is high enough, the refractive index of the waveguide layer undergoes enough modulation to shift the resonance of the GMRF away from the incident wavelength. When the resonance is shifted away from the incident wavelength, the field intensities within the GMRF decrease, causing the refractive index change from the non-linear effect to decrease. This results in a return to the original resonance conditions. This has the effect of creating a temporally modulated device.

In addition, the sensitivity of the resonance condition of GMRFs to the structural and optical parameters can be applied to sensors [36]. GMRFs have also been used as biosensors and chemical sensors [37]. These sensors are used to monitor or detect different types of cellular reactions or chemicals. In one example, a GMRF consisting of a substrate, waveguide, SWG and a cladding region is used as a biosensor. As discussed previously, the GMRF resonance is a function of all of the structural and optical

properties of the device. In these types of sensors, the cladding or the SWG region is affected by either a chemical or a biological reaction that changes the refractive index of that region. This has the effect of changing the resonance conditions of the GMRF. If the GMRF is probed with light at the initial resonant wavelength, a shift in the resonance can be observed and a chemical or biological reaction can then be detected [37]. These types of sensors and applications can be made possible by the sensitivity to the structural and optical parameters that GMRFs show.

## 1.4. Graded Reflectivity Mirrors

Graded Reflectivity Mirrors (GRMs) are mirrors with a spatially varying reflectance profile [38, 39]. They have applications as feedback mirrors in unstable laser resonators [40, 41] and to control the shape of optical beams exiting laser cavities [41, 42]. The first GRM was demonstrated in 1985 by Lavigne et al. [38]. The fabrication method used to create these GRMs limits the devices to axial symmetry; commercially available GRMs cannot be made with arbitrary spatial reflectance profiles. The devices proposed and described in this dissertation offer an alternative solution to conventional GRMs and they are also capable of non-axially symmetric reflectance and transmittance profiles.

Conventional GRMs consist of a spatially varying thin film dielectric that is deposited onto a substrate. The substrate is usually prepared with an AR coating operating at the wavelength of interest. The reflectance or transmittance of any thin film dielectric is a function of the thin film's refractive index and its thickness. A spatially varying reflectance profile can be achieved by spatially varying the thickness of the thin film. This is done during the deposition process of the thin film. Figure 1.25 shows a

simple schematic diagram of the deposition process. The thin film is deposited using standard deposition techniques with one exception; a mask is placed close to the substrate that the thin film will be deposited onto. The mask has the effect of creating a “shadow” during the deposition; the deposition becomes non-uniform and the deposition rate decreases from the center of the masking area [43]. This creates an axial symmetric deposition with a radially varying thin film thickness.

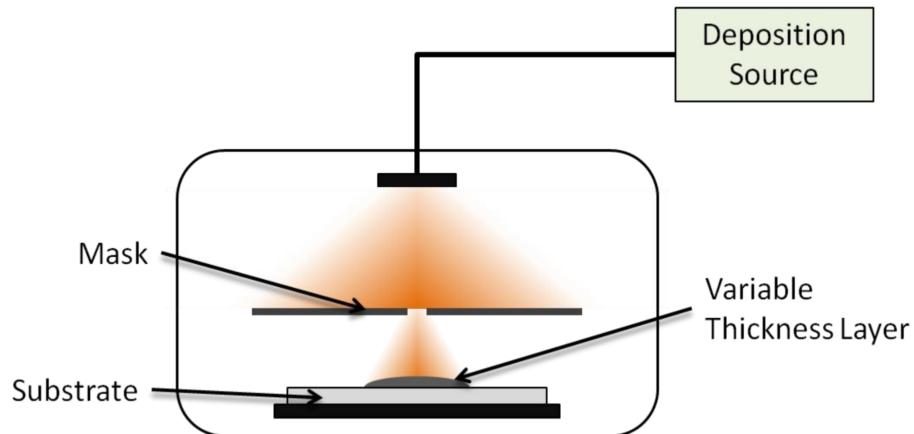


Figure 1.25. Schematic diagram showing the deposition process of a GRM.

# CHAPTER 2: FABRICATION METHODS

## 2.1. Introduction

The guided mode resonance filters (GMRFs) presented in the previous example present an ideal device to be fabricated with microfabrication technologies. The period of the subwavelength grating (SWG), for use in the near infrared and infrared wavelengths, is on the scale of features routinely fabricated with microfabrication technologies. The thicknesses and materials used in the dielectric layers of the GMRFs presented in this dissertation can also be fabricated using deposition technologies shared by the microfabrication industry. In addition, it will be shown that the desired spatial variations in the structural parameters of the devices proposed in this dissertation can be fabricated using novel techniques compatible with the methods used in microfabrication technologies.

Microfabrication technologies and techniques are used to fabricate the micro-optical devices described in this dissertation. These processes fall into three main categories: lithography, transfer etching, and material deposition. Lithography is used to create the micron-scale patterns that create the SWGs, while transfer etching is a process that transfers that pattern into different materials. Occasionally, thin film dielectrics and metals are needed in micro-optical devices, and various deposition methods are used to accomplish this.

Microfabrication technologies have been around for decades, and are primarily used to create computer chips and integrated circuits (IC). However, these fabrications technologies have also been used to make MEMS (Micro-Electro-Mechanical Systems), Micro-Optic and Micro-Photonics Devices, displays, and more. Microfabrication techniques are used to create various types of structures on or in a substrate material [44] with feature sizes on the order of a micron.

## 2.2. Conventional Lithography

Lithography is the process by which micron scale patterns are created and used in micro-optical and micro-photonic devices. Without lithography, we would not be able to make computer chips, MEMS, or micro-optics devices. Conventional lithography focuses on the creation of binary patterns; however, it is possible to use the same lithographic systems used in IC fabrication to create three-dimensional structures. A brief overview of conventional lithography is then necessary to describe these advanced techniques.

While there are many different types of lithography, this dissertation will only cover photolithography. Photolithography is the method of creating patterns or structures in a photosensitive material using a structured pattern of light. The photosensitive material is often referred to as "photoresist", and occurs in two types: positive tone resist and negative tone resist. Furthermore, there are two main types of conventional photolithography that will be covered: contact lithography and projection lithography.

Generally, the photolithographic process begins by applying a layer of photoresist to a substrate material. These substrates come in various sizes and are referred to as "wafers". Typically, a binary amplitude mask is used in conjunction with a light source

and an optical system to image patterns from the photomask into the photoresist. After the photoresist is exposed, the photoactive compound is developed, often by means of a commercially available liquid developer. Pattern development and transfer is completed by removing the exposed portions of positive tone photoresist and the unexposed portions of negative tone photoresist through a chemical reaction.

### 2.2.1. Photoresist Response

Photoresist is a key element in lithography; its properties and photoactive response are crucial to the fabrication of the three-dimensional micro-photonic devices presented in this dissertation. Photoresist is a photosensitive material, undergoing a chemical reaction when exposed to light. Photoresists consist of two main components, a solvent and a photoactive compound (PAC). Photoresists are typically applied to a substrate using a spinning technique. After the substrate is centered on a vacuum chuck, a small amount of liquid photoresist is poured onto the wafer. The wafer is then spun at a relatively high speed between 1000 and 6000 rpms. The spin-coating technique casts off excess photoresist while simultaneously causing the solvent in the photoresist to begin evaporating, leaving a thin layer of photoresist. The substrate is subsequently baked to dry the resist of solvent. This baking step is referred to as the post-application bake (PAB). The parameters of the spin-coating and baking process are dependent on the specific photoresist being used, the desired thickness of photoresist, and other parameters in the lithographic process.

After the application of the photoresist, the device pattern can then be exposed into the photoresist using one of several lithographic methods described in later sections. As the photoresist is exposed, it causes chemical reactions to occur within the photoresist.

These chemical reactions are strongly localized to the area of exposure and begin at the surface of the photoresist nearest to the direction of illumination. The amount of energy applied to the photoresist can be varied by altering the time of the exposure, referred to as the "dose". After the exposure, the wafer can be baked an additional time to help fix the pattern; depending on the photoresist, the bake can also change the rates of the chemical reactions taking place. This additional bake is often termed the post-exposure bake (PEB).

Once the PEB is completed, the wafer is allowed to cool to room temperature before further processing. While there exist various ways of developing photoresist, all of the devices fabricated in this dissertation were made using an immersion method. In the immersion method, the wafer is submerged for a specific time in a commercially available developer. For every photoresist used in this dissertation, there is at least one commercially available developer that can be used with it. In the case of positive tone photoresists, the developer will etch the areas of the photoresist that have been adequately exposed. At this point, the lithography process is usually complete.

Previously, it was stated that the exposure begins at the surface of the photoresist. Considering the top-down nature of the exposure process, the exposure of resist is not a binary reaction. In other words, we can expect a partial exposure to remove a portion of the photoresist during development. This subtle fact has practical applications to the fabrication of three-dimensional micro-photonic devices, and it will be described in further detail. In Figure 2.1, we can see the exposure response curve for a typical photoresist used by our research group.

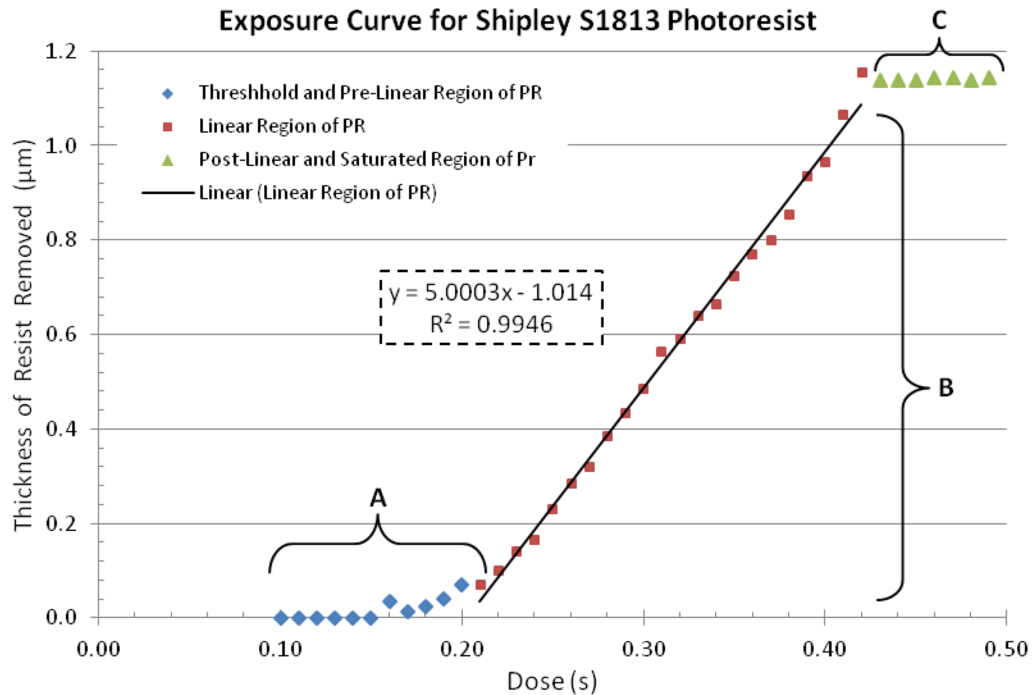


Figure 2.1. Exposure Response Curve for positive tone Shipley S1813 photoresist spun at 2.5 krpm.

Figure 2.1 is an example of an exposure dose curve for a linear photoresist, where the partial exposure regime is linear. In Figure 2.1, there are three main regions to the photoresist response curve. The threshold and pre-linear regions of the photoresist is the portion of the response curve labeled "**A**" and includes the doses that fall below the threshold of the resist. The threshold energy is the dose at which the photoresist will begin to be removed by the developer. The partial exposure region of the exposure curve is labeled "**B**", for the resist shown here this region is linear. However, it should be noted that not all photoresists have a linear partial exposure region. The saturation region of the photoresist response curve, labeled as "**C**", begins with the minimum dose required to remove all of the resist in an exposed area. This minimum dose is referred to as the 'dose to clear." This dose is typically defined for features sizes much greater than the resolution limit of the lithographic system being used.

Figure 2.1 was made by varying the exposure dose of an open box across a single wafer, and measuring the depths of the resulting boxes using a Tencor Alpha-Step Profilometer. Linear responses of photoresists are often seen with thin resists; however, the exposure response of thicker resists tends to be logarithmic. This is to be expected, because the response curve is a function of the amount of optical energy that is absorbed in the photoresist.

2.2.2. Contact Lithography

Contact lithography is a photolithographic method where a photomask containing a pattern is placed either near to, or in direct contact with the photoresist on the wafer to be patterned. Figure 2.2 shows a general layout of this setup. Contact lithography creates a 1:1 image of the photomask in the photoresist.

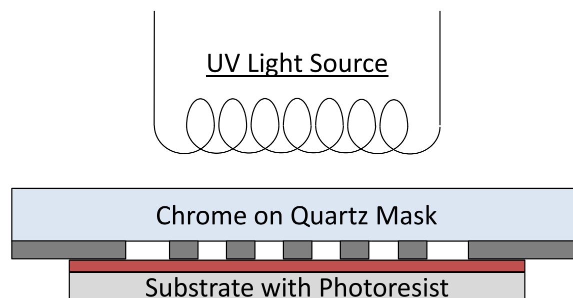


Figure 2.2. Diagram showing the schematic setup of contact lithography

The smallest resolvable feature that can be created is typically called the resolution limit. The smallest line or space on a mask is typically called the critical dimension or C.D. The resolution limit for contact lithography is:

$$b = \frac{3}{2}\sqrt{\frac{\lambda d}{2}} \qquad 2.1$$

In Equation 2., the resolution limit is a function of the wavelength of the light source, $\lambda$, and the thickness of the photoresist, $d$ [44]. This limitation is primarily caused by the near-field diffraction of the mask, and it assumes that the photoresist is in contact with the mask. For an I-line source ($\lambda$ = 365 nm) and a resist thickness of 350 nm, the smallest patternable feature is 379 nm. Imperfections in the resist or the photomask, as well as non-uniform contact between the mask and the photoresist will cause the resolution limit to increase.

Typically, contact lithography is performed on the entire wafer. The large exposure region allows for large area devices to be created. Furthermore, degradation of the photomask occurs due to its contact with the photoresist, limiting the photomask's use in large volume production.

### 2.2.3. Projection Lithography

Projection lithography creates a pattern in the photoresist by forming an image of a binary amplitude photomask in the photoresist. In many systems, this image is a demagnification of the mask. The advantages of this are to decrease the cost of obtaining photomasks by increasing the size of the features on the photomask and also to create multiple instances (dies) of the same pattern in the photoresist. In these systems, the patterns on the photomask are imaged or "stepped" across the wafer to create multiple copies of the same pattern or device.

Figure 2.3 shows a simplified projection lithography system. The projection lithography tool used in this dissertation is a GCA G-Line Stepper 6500. This system is referred to as a stepper system, because the wafer is placed on a motorized stage, and during normal operation the mask pattern is exposed numerous times (i.e. stepped) across

the wafer. Ultra-violet (UV) Light is emitted from a mercury lamp. It is conditioned and filtered in the condenser optics, uniformly illuminating the mask.

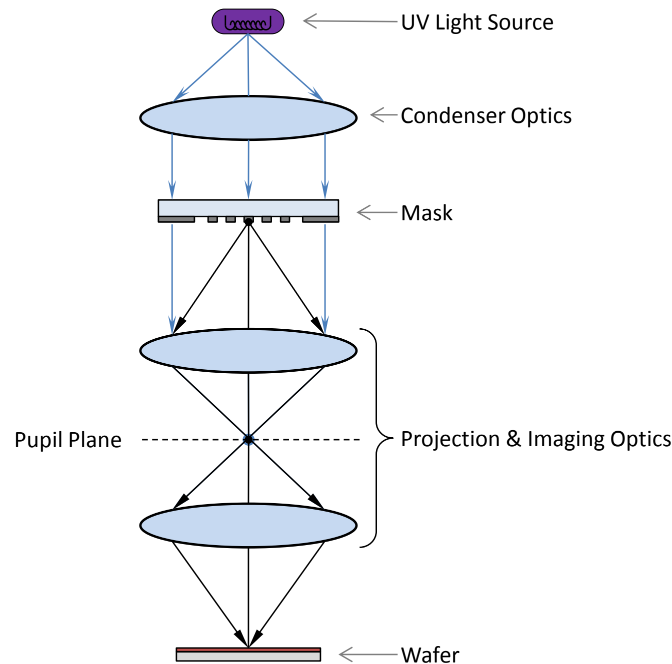


Figure 2.3. Simplified schematic diagram of a projection lithography system

The maximum field size that can be generated is 10 cm by 10 cm in the mask plane. The projection optics form a 5X demagnified image in the wafer plane to create a maximum field size of approximately 20 mm by 20 mm in the wafer plane.

The positioning of the stage is accurate and repeatable, permitting alignment between patterns to better than 0.25 μm using this tool. Additional alignment techniques can be used to increase this alignment to around 0.1 μm. The dose and focus level of the image can also be varied across the wafer to optimize the pattern. In contrast to contact lithography, the devices made using stepper lithography tools have a smaller footprint.

The resolution of this stepper system is a function of the quality of the images it produces and various other parameters in the photolithographic process. The resolution limit of a projection lithography system can be described by Equation 2.2 [44].

$$b = \frac{k_1 \lambda}{NA} \tag{2.2}$$

The C.D. for a stepper system is not as easily calculated as a contact lithography system because $k_1$ is a function of the stepper system as well as other elements in the photolithographic process. The actually value of these parameters are often found empirically, and is beyond the scope of this dissertation. In Equation 2.2, $\lambda$ represents the system wavelength and NA is the numerical aperture of the lens system. The resolution for the system used in this dissertation is around 0.8-1.0 μm. A decrease in wavelength and an increase in the numerical aperture will result in a decrease of resolution limit. Current state of the art projection systems exploit this relationship by employing extreme ultra-violet sources and high numerical aperture immersion lenses to decrease the system resolution limit, enabling the creation of smaller integrated circuits (ICs).

## 2.3. Additive Lithography

While conventional lithography primarily focuses on creating binary patterns or structures, micro-optical devices require complex geometries. To construct these devices, multiple techniques may be used in conjunction with the lithographic tools available in conventional lithography. Additive lithography is one of these techniques, creating a series of multiple steps in photoresist [45-48]. These multilevel structures are often used to approximate various types of optical phase functions for three-dimensional micro-optics. This type of three-dimensional multilevel element is often referred to as a Diffractive Optical Element (DOE).

Additive lithography makes use of the partial exposure portion of the photoresist response curve (see Figure 2.1 for an example), and works best with linear regions of the curve. It uses a series of N conventional binary amplitude photomasks to create a multilevel structure with $2^N$ levels. The photoresist will be exposed using each of these photomasks, at different partial exposure doses, including overlapping areas between the various masks. Figure 2.4 shows an illustrative example of how this is done. The combination of different doses and different overlaps allows the creation of $2^N$ levels from N masks. For example, to create an N=3, 8-level element, three masks are needed, in addition to a bias photomask containing only an open area corresponding to the size of the device. The purpose of the bias photomask is to bias the resist to the linear response region of the photoresist shown in Figure 2.1.

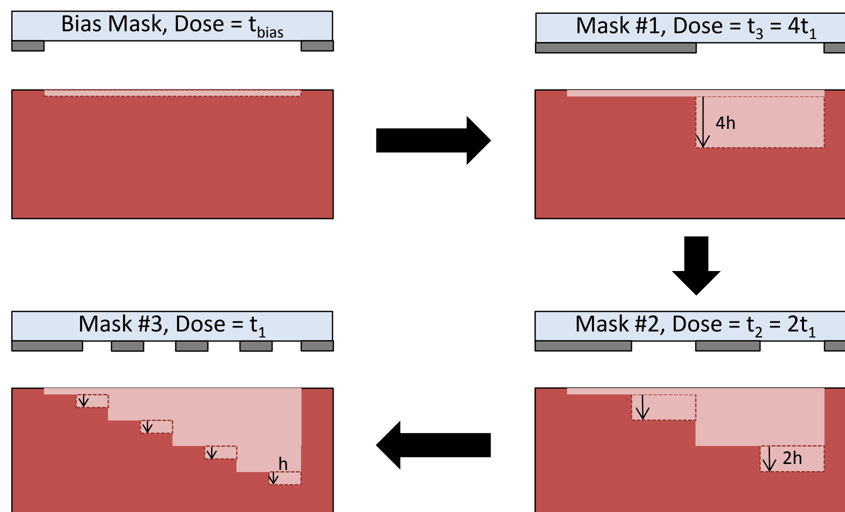


Figure 2.4. Schematic Diagram representing Additive Lithography for a N=3, 8 Level element

As shown in Figure 2.4, a multilevel element with a step height of *h* may be created using three photomasks, where exposure doses for the various photomasks

correspond to step heights of *h*, *2h,* and *4h*. Overlapping combinations of these masks will create a structure of eight levels with a total height of *7h*. These combinations are shown in Table 2.6, where ● represents a closed (non-transmitting) portion of the photomask, and ○ represents an open area in the photomask. All of the patterns are first exposed in the photoresist, and then the lithography is concluded with the development cycle. Depending on the photoresist used and specific process parameters, a PEB can be included. The exposed multi-level pattern is revealed in the photoresist after the development cycle.

Table 2.6. Overlap combinations to create an N=3, 8-Level Multilevel Element

| Level | Height | Mask #1 | Mask #2 | Mask #3 |
|---|---|---|---|---|
| 1 | 0 | ● | ● | ● |
| 2 | 1h | ● | ● | ○ |
| 3 | 2h | ● | ○ | ● |
| 4 | 3h | ● | ○ | ○ |
| 5 | 4h | ○ | ● | ● |
| 6 | 5h | ○ | ● | ○ |
| 7 | 6h | ○ | ○ | ● |
| 8 | 7h | ○ | ○ | ○ |

## 2.4. Analog Lithography

In the previous section, it was shown that additive lithography can be used to create three-dimensional micro-optics but is limited to creating structures with discrete levels. Three-dimensional micro-optics can have unwanted diffracted orders associated with the multi-level nature of the structure, and will also result in an optical throughput loss. Analog Lithography is a technique that can create continuous, arbitrary three-

dimensional structures [49]. As with additive lithography, analog lithography makes use of the partial exposure portion of the photoresist response curve. It will also be shown that Analog Lithography can be used with non-linear photoresists.

Unlike Additive Lithography, Analog Lithography utilizes a different type of photomask than conventional lithography. A sub-resolution phase mask comprised of a phase grating, with a $\pi$ phase shift, that has a slowly and spatially varying duty cycle or fill fraction. It is important that the phase grating period be shorter than twice the resolution limit of the lithographic system. When this phase grating is sub-resolution, the higher diffraction orders can be blocked by the system. An analog irradiance pattern can be made by slowly varying the fill-fraction of the phase grating across the phase mask. The diffraction efficiency of the $0^{th}$ order, the only order to make it through the system, is a function of the fill fraction. Figure 2.5 shows a schematic diagram of analog lithography, with the higher order diffraction orders blocked by the stepper system. It should be noted that this fabrication method can only be used with projection lithography systems due to the requirement of filtering out the higher diffracted orders.

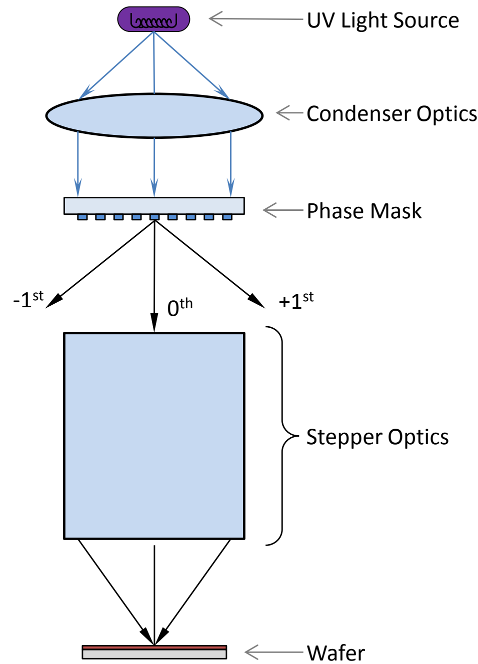


Figure 2.5. Schematic diagram of Analog lithography.

The smallest period of a projection lithography system is typically twice the resolution limit and can be found by using Equation 2.3 [50].

$$\Lambda_{min} = \frac{M\lambda}{NA(1+\sigma)} \quad 2.3$$

In Equation 2.3, *M* is the demagnification factor, λ is the system wavelength; *NA* is the numerical aperture of the system; and σ is the partial coherence of the source. For the stepper system described used in this dissertation, *M* = 5; λ = 436 nm (G-line); the NA = 0.35; and σ = 0.6 [49]. This results in a period of 3.89 μm in the mask plane. The period of the phase grating will need to be less than this so that only the $0^{th}$ order propagates through the system.

Figure 2.6 depicts a 2D phase grating with a period of Λ, and a width and length of *a*. The fill fraction of this grating would be $a^2/\Lambda^2$. The phase gratings used in analog

lithography all have a π phase depth, a phase difference of π radians between top and bottom of the grating structure. This allows for a full intensity modulation.

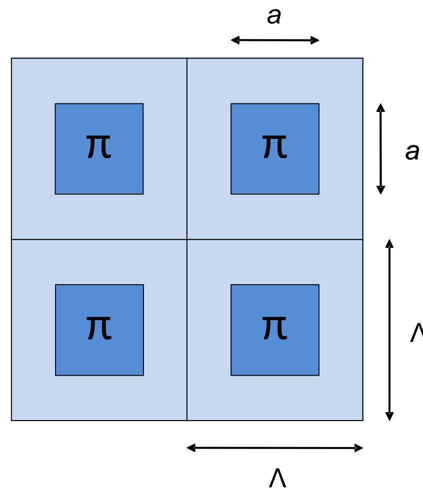


Figure 2.6. Depiction of the top-down view of a phase grating [49]

Equation 2.4 describes the transmittance function of a general non-space varying phase grating with a phase depth of π radians. The Fourier Transform in the far-field yields a term representing the intensity in the $0^{th}$ order, described by Equation 2.5. In Equation 2.5, $w$ is the fill fraction ($a^2/\Lambda^2$) for a 2D phase grating, as well as the duty cycle ($a/\Lambda$) for a 1D grating. Furthermore, the diffraction efficiency of the $0^{th}$ order is a function of the fill fraction or duty cycle.

$$t(x,y) = [2rect(\frac{x-a/2}{a},\frac{y-a/2}{a}) \otimes \frac{1}{\Lambda^2} comb(\frac{x}{\Lambda},\frac{y}{\Lambda})] - 1 \qquad 2.4$$

$$DE(w) = 1 - 4w^2 + 4w^4 \qquad 2.5$$

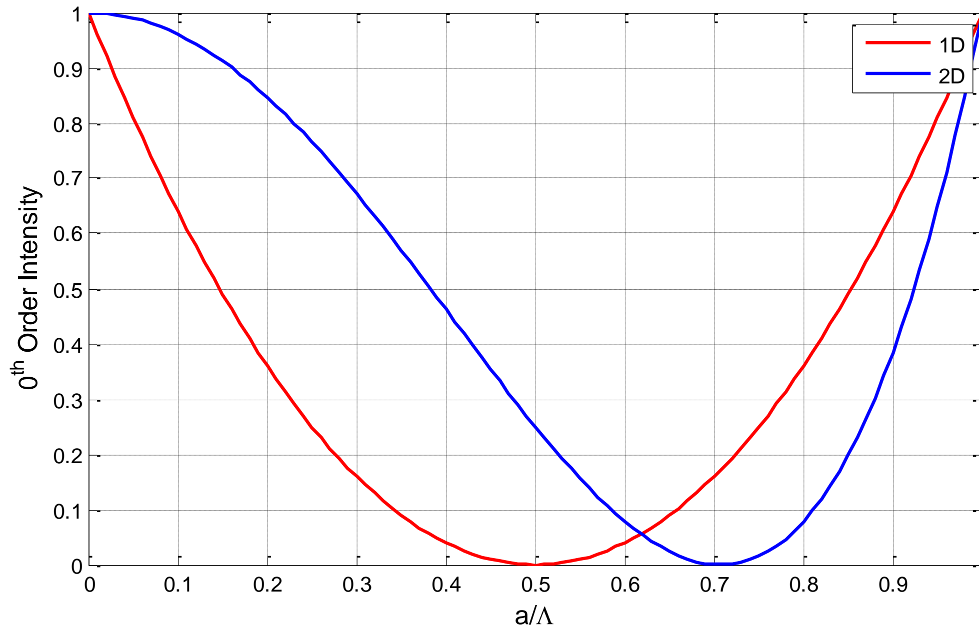


Figure 2.7. Diffraction efficiency of the $0^{th}$ order for 1D and 2D phase grating.

In Figure 2.7, the $0^{th}$ order diffraction efficiency is plotted for a one-dimensional phase grating and a two-dimensional phase grating. It is plotted versus the parameter *a/*Λ, which is the duty cycle for the one-dimensional grating and it is the square root of the fill fraction. The reason for plotting it against *a/*Λ has to do with limitations in the lateral size of the phase grating and not the area of a unit cell. From Figure 2.7, a larger variation in the lateral extent of the unit cell of the 2D grating is needed to create the same intensity modulation as the 1D cell. This is advantageous, because creating a slowly varying intensity distribution is often desired. Having a larger *a/*Λ range to work with will be beneficial to the fabrication of the phase mask.

2.4.1. Phase Mask Fabrication

To create a phase mask, the width of the opening of the gratings in the phase mask needs to be changed by a small amount. While the size of the features in the phase mask may be large, the amount by which they change needs to be small. This greatly

increases the tolerance of the C.D. of the phase masks, and necessitates a more expensive option to have the phase mask fabricated over that of conventional masks.

The phase masks used in analog lithography are often fabricated using electron beam (e-beam) lithography. E-beam lithography differs from photolithography in that it uses an electron beam to expose an electron sensitive resist, and that it is a direct write method. A direct write method is one in which the pattern is written in a serial fashion. In conventional photolithography, the photomask is exposed over a larger area and that area is written into the photoresist all at once. E-beam lithography is mask-less, and it scans a small electron beam across the substrate or sample point-by-point, or pixel by pixel to expose the pattern. This greatly increases the time it takes to create a pattern; however, because a stream of electrons is being used versus a large beam of photons, the smallest feature that can be created is much less than that of photolithography.

In electron beam lithography, the desired pattern is fractured or broken up by software in pixels that correspond to the size of the electron beam being used. Thus for a slowly varying pattern like the spatially varying phase gratings discussed above, individual unit cells will be “snapped” to the nearest integer sized beam. In large area devices with an extremely slow height variation, this can create areas where the unit cells are snapped to the same widths and do not change. If these areas are too large, then the height of the element that is fabricated transitions from being a continuous height to being a multilevel element similar to those created by additive lithography. The solution to this is to decrease the beam size and thus the pixel size of the mask during fabrication. However, this will greatly increase the time it takes to write the phase mask and that will drive up the cost considerably.

Considering this, it is advantageous to use a two-dimensional phase grating, as that would increase the range over which the width of the π phase shift, $a$, is varied. This allows for a greater number of snaps to occur and thus the phase mask will better approximate an analog pattern.

Typically, the e-beam systems accept a data file that contains the patterns to be fabricated. Most mask-layout software packages do not contain options that allow the creation of a grating with a varying fill fraction. To accommodate this, proprietary software is used for the creation of the data files used to obtain a phase mask. This software uses the relationship between the fill-fraction of the phase grating and the resultant diffraction efficiency to create a data file that is readily accepted by most commercial software packages. Section 2.2.1 shows that the height of the photoresist as a function of irradiance can be found. If the phase mask is designed with a specific photoresist and exposure curve in mind, then it is possible to tailor the desired intensity distribution to the photoresist response. In doing this, the fill fraction variation will be modulated so that the desired continuous photoresist cross section is created. This allows for the compensation of a non-linear photoresist response. It should also be noted that if the continuous photoresist cross section is then transferred into another material, then the parameters of that transfer should also be considered in the phase mask design process.

## 2.5. Transfer Etching

The previous sections in this chapter focused on the creation of structures in photoresist. However, photoresist is generally not a suitable material to use for optical materials considering that it is photosensitive and prone to scratches. Also, because most photoresists are organic polymers, they will be typically removed by the same chemicals

(Acetone, Isopropanol, and Methanol) that are used to clean glass based optical elements. In addition, for some of the devices presented in this dissertation, it is necessary for the desired patterns to be in a specific material with specific optical properties. Considering these factors, it is necessary to transfer these patterns and structures into other materials. There are many microfabrication processes and methods of transferring patterns and structures, but this discussion will focus on plasma etching, more specifically Inductively Coupled Plasma (ICP) etching. A complete discussion of the characteristics of this etching technique is beyond the scope of this dissertation, but a brief overview will be provided.

Etching is the term applied to the processes that are used to remove material from a device or substrate [44]. These processes can be either physical or chemical in nature. In a physical etch process, material is removed through a physical mechanism such as ion bombardment in ion milling, while in chemical etching, the material is removed through a chemical reaction. In both of these cases, a masking material is used (e.g. a patterned photoresist) that can obscure portions of the material to be etched. This results in a transfer of the pattern from the masking material into the etched material. The material can be removed in a number of ways. Material can be removed isotropicaly, etching at a constant rate in all directions. This creates curved etch profiles and enlarged features. Alternatively, the etch process can be anisotropic and the etch rates will vary with direction. Anisotropic etches can create high fidelity, high aspect ratio transfers of patterns. Figure 2.8 shows a simple representation of these two types of etches. With isotropic etching, material is removed beneath the masking layer. This is referred to as "undercutting", and it can limit how deep a feature can be patterned into a substrate.

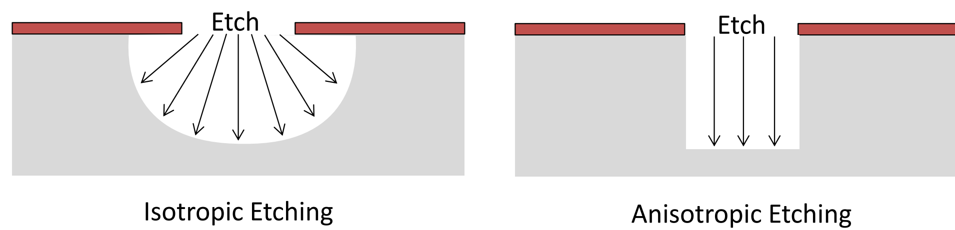


Figure 2.8. A simple diagram showing the difference between anisotropic and isotropic etching

ICP etching is a combination of physical and chemical etching methods. Plasma is a combination of neutral gas species, ions, and radical gas species. Radical gas species are typically responsible for the chemical etching in a plasma process, while ions are typically responsible for the physical aspects. The plasma is created in a plasma chamber. Typically, the chamber is pumped down to low vacuum levels, prior to the injection of a suitable gas. While the gas is flowing in, a vacuum pump is still operating on the chamber to keep the pressure low. An electric field is then applied to this chamber. Once this field becomes large enough, a relatively small portion of the molecules in the neutral gas species ionize, creating free electrons, ions and neutral gas species. The free electrons will collide with other neutral gas species creating more ionized molecules and radical gas species. In addition, highly energized ions will occasionally discharge a photon, which creates the characteristic glow of the plasma.

In a simple plasma etcher, an RF source is applied to the electrodes. The substrate is placed on one electrode, and the gases are introduced into the chamber through the other. This method is known as Reactive Ion Etching (RIE). In Inductively Coupled Plasma (ICP) Etching, an additional coil is placed around the vacuum chamber. A schematic of this is shown in Figure 2.9. When an RF source is applied to the ICP coil,

electric and magnetic fields are created within the plasma chambers; these fields increase the free-election mean path length creating more collisions within the plasma, and increase the amount of ions, free electrons and radicals in the plasma.

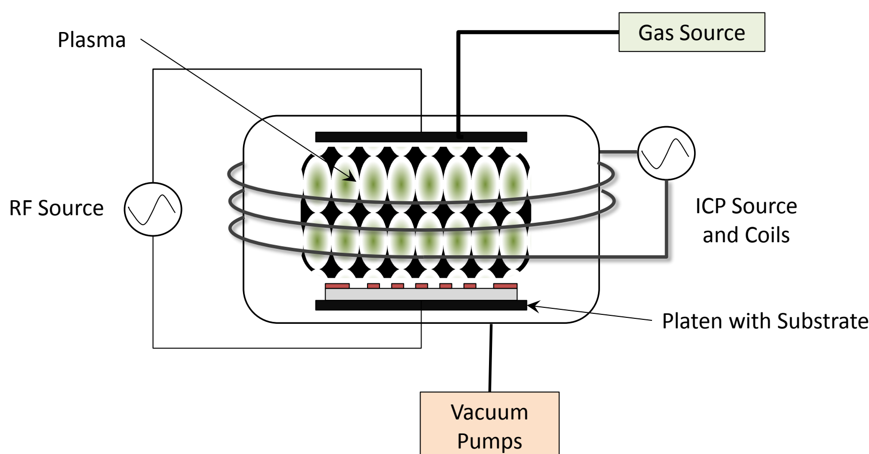


Figure 2.9. A simple schematic diagram of an ICP Etcher

When patterns are etched using this plasma method, the etching is typically anisotropic due to the physical and chemical nature of the etch. Charged ions are directed to the surface of the substrate by the electric field applied to the electrodes. The interaction between the ions and the surface causes the surface to be more reactive to the neutral radicals in the plasma. The reaction of the radicals with the material to be etched needs to produce a volatile chemical, so that it can be pumped out of the chamber with the vacuum pumps. Due to the directionality of the ions, a preferred etch direction and anisotropy are created. Without the ICP coils, this method of plasma etching is typically referred to as Reactive Ion Etching (RIE). In this research, the ICP etcher we use is a Unaxis (Plasma-Therm) Versaline High Powered Oxide Etcher.

Typically, the substrates used in this research are fused silica, and the dielectric films used are Silicon Nitride ($Si_xN_y$) and Silicon Oxide ($SiO_x$). The chemistry used to

etch these materials is a $CHF_3$:$O_2$ gas mixture. $CHF_3$ provides $CF_x$ reactive radicals used to etch and $O_2$ provides $O_2^+$ ions that help to prevent polymers from depositing during the etching. The addition of oxygen into the plasma will also etch organic polymers such as photoresist. A common recipe for etching fused silica and $SiO_x$ films has an ICP power of 500 W, a RIE power of 50 W, a $CHF_3$ flow of 70 sccms, a chamber pressure of 10 mTorr and $O_2$ flow of 5 sccms. This produces an etch rate of approximately 180 nm/min in fused silica and an etch rate of 130 nm/min in photoresist. The duration of the etch is then used to etch to a specific depth.

2.5.1. Selectivity

Selectivity is the term applied to the ratio of the etch rate of the targeted material to the etch rate of the mask material. For example, the recipe described above would correspond to a selectivity of 1.4:1. When etching binary patterns such as gratings, the selectivity will determine the minimum thickness of the masking layer required to achieve the target etch depth. Also, because the etch is anisotropic, and the etching chemistry provides an etching mechanism for both the photoresist masking layer and the substrate materials, it is possible to transfer more complex three-dimensional structures into the substrate or other materials. In this case, the selectivity will determine how much a three-dimensional pattern is stretched or compressed in the vertical direction. Thus, the selectivity will determine the required height of a three-dimensional pattern in photoresist to achieve a targeted structure is some other material.

Given that the $CHF_3$ gas provides the predominate etching mechanism for the fused silica substrate and $O_2$ does the same for photoresist, the selectivity appears to be adjustable by altering the relative oxygen content of the plasma. Figure 2.10 shows the

relationship between the oxygen content and the selectivity. The etch had an ICP power of 800 W, and RIE power of 80 W, a pressure of 10 mTorr, and the flow rate was kept nearly constant at 75 sccm. With this process, the selectivity can be varied between 1.2:1 and approximately 0.195:1.

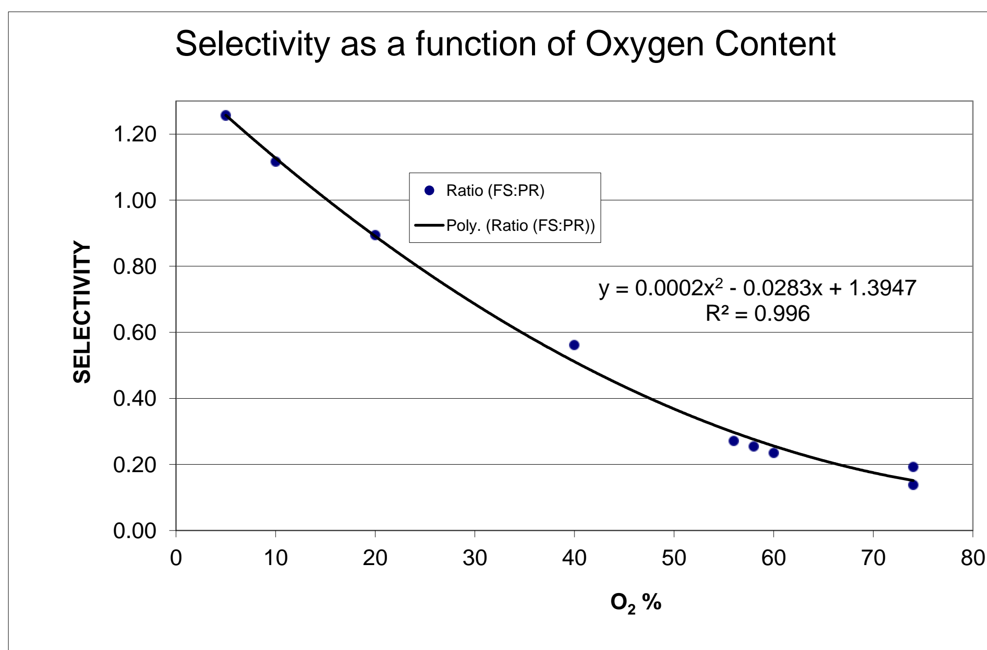


Figure 2.10. Selectivity between fused silica substrate and photoresist as a function of oxygen content

## 2.6. Material Deposition

As with all other areas of microfabrication, there are numerous ways to deposit materials onto a substrate. All of these methods fall into two main categories: Physical Vapor Deposition (PVD) and Chemical Vapor Deposition (CVD). PVD deposits material through a physical reaction such as thermal evaporation, where a material is heated in a low vacuum chamber to the point that it forms a vapor that will coat any surface it comes into contact with. CVD techniques involve the deposition of materials

through a chemical reaction. Typically, two or more gases enter a vacuum chamber; through a complex reaction that varies with the type of CVD, a solid thin film is deposited onto the substrate [44]. The thin films deposited during this research were done using the plasma enhanced chemical vapor deposition technique (PECVD).

Similar to the plasmas described above, PECVD techniques use RF generated plasma to deposit thin films on a substrate. Combinations of gases are introduced into the chamber, and the radicals created in the plasma react to form the desired material and adhere to the substrate. Typically, the substrates are heated to high temperatures (~300$^{o}$C) to promote adhesion of the thin film to the substrate. In addition, the films deposited are not strictly stoichiometric; that is, when Silicon dioxide is created, it is $SiO_x$ rather than $SiO_2$. This is a result of ion bombardment on the thin film from the plasma during the deposition. The system used in this research is an STS PECVD. This tool is capable of depositing silicon oxides ($SiO_x$), silicon nitrides ($Si_xN_y$), and silicon oxynitrides. Figure 2.11 depicts a dispersion curve for the PECVD $SiO_x$ used in this research and Figure 2.12 shows the dispersion curve for the $Si_xN_y$. Figure 2.11 also shows the dispersion curve for fused silica. These curves were found by experimentally determining the Sellmeier Coefficients for the PECVD films and the Cauchy constants for the fused silica substrate. The thin films were characterized on a Woollam Ellipsometer.

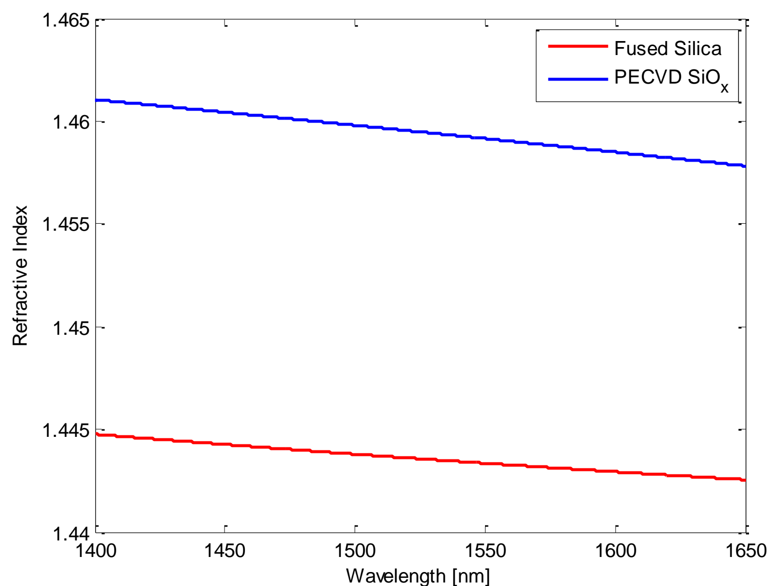


Figure 2.11: Dispersion Curve for Fused Silica and PECVD SiOx

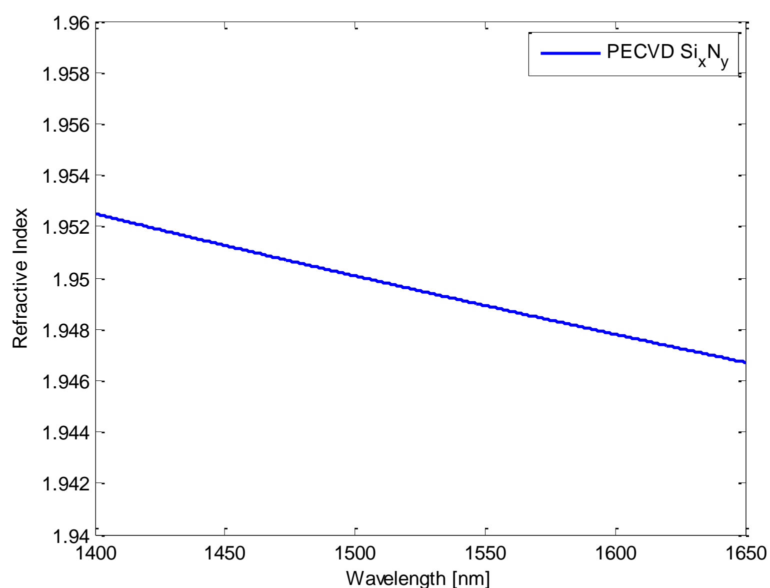


Figure 2.12: Dispersion Curve for PECVD SixNy

## 2.7. 16-Level Optical Vortex

One example of an application of three-dimensional lithography is the creation of optical vortices. The optical vortices discussed in this dissertation are phase functions where the phase varies linearly with the azimuthal angle between 0 and $m2\pi$, where $m$,

referred to as the topological charge of the vortex element and is an integer [51, 52]. Optical vortices have many applications such as optical tweezers [53, 54], microscopy [55], and astronomy [56]. Figure 2.13, shows an analog vortex element on the left, and a 16-level additive vortex on the right. The vortex on the right is an example of the type of element that can be made with additive lithography.

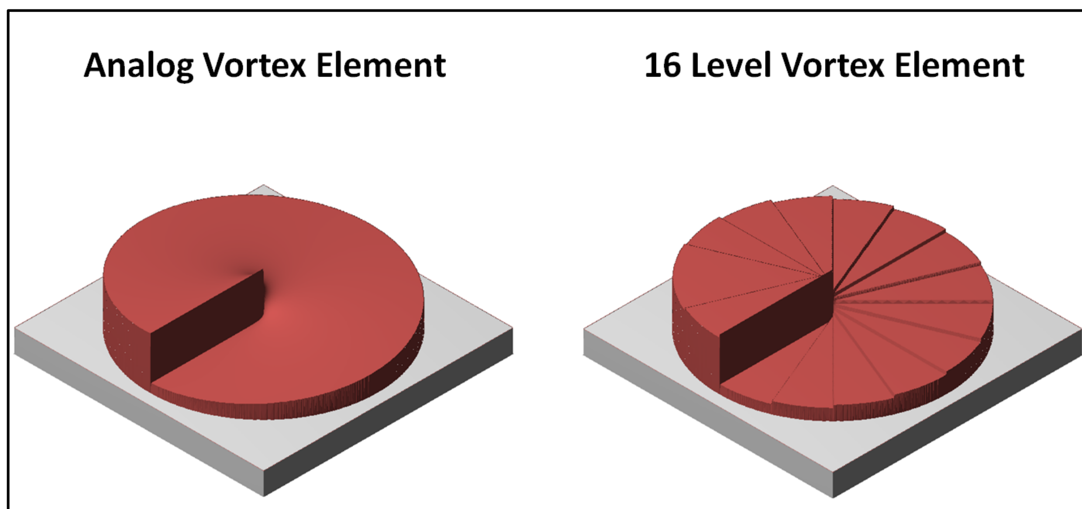


Figure 2.13: (Left) An Analog Vortex Element (Right) a multilevel Vortex Element

The vortices described above were designed and fabricated to be used in fused silica and operate at a wavelength of 800 nm. The index of refraction of fused silica at that wavelength is n=1.4536. The total height of the device corresponds to a 2π phase depth is given by Equation 2.6. The resulting 2π phase depth is 1.764μm in fused silica.

$$d_{2\pi} = \frac{\lambda}{n-1} \qquad 2.6$$

The device was created in photoresist using additive lithography, and subsequently transferred into the fused silica substrate via plasma etch. In order to obtain the correct height in the substrate, an etch selectivity is assumed from previous results.

The selectivity of the process previously used was 1.1:1, corresponding to a device with a desired height of 1.603 μm in photoresist. Shipley 1813, as shown in 2.1, has a maximum thickness of ~1.1μm, so a thicker photoresist was necessary. To this end, SPR220-7.0 was spin-coated onto fused silica substrates at 4000 rpms, to a total thickness of 6.34 μm. Even though SPR220 typically has a non-linear response, there is a large enough region of the photoresist response curve that is linear to fabricate this device using additive lithography.

In order to use the linear portion of the photoresist response, a bias dose of 0.73 seconds was used, to remove ~2.6 μm of photoresist. The fabricated devices will be an N=4, or 16 level system with a target height of 1.603 μm. This target height corresponds to a total additive exposure of 0.27 s. The additive doses were as follows: Mask #1 had a dose of 0.144 s; Mask #2 had a dose of 0.072 s; Mask #3 had a dose of 0.036 s and Mask #4 had a dose of 0.018 s. Figure 2.14 shows the mask set that was used to create the vortex lens described here.

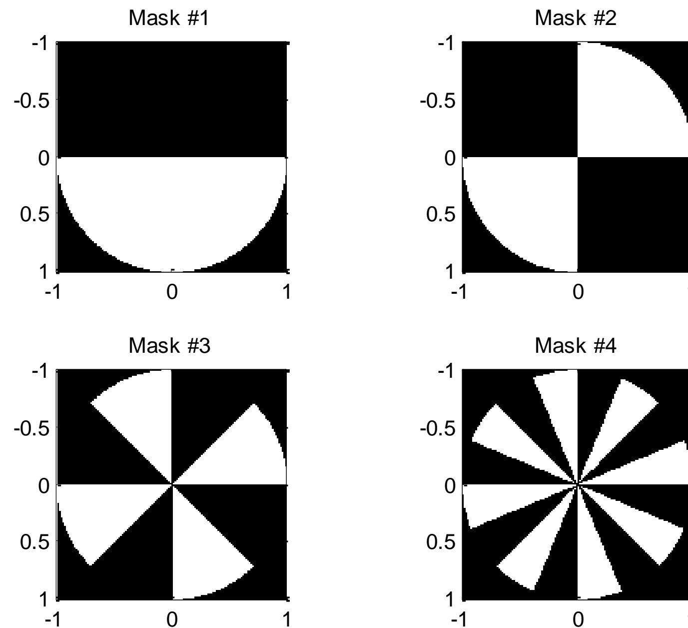


Figure 2.14. The mask set used to make a 16-level optical vortex.

After the vortices were patterned in photoresist, they were imaged using an Olympus LEXT three-dimensional Confocal Microscope. Figure 2.15 shows the 16 level vortices in photoresist on the left and in fused silica on the right. The height of the photoresist was determined to be 1.73 µm. The expected height of the vortices in photoresist was 1.6 µm. In order to achieve the desired height of 1.764 µm in fused silica, the etch selectivity was modified. After the vortices were imaged using the three-dimensional Confocal microscope, they were etched using a Unaxis Versaline High Powered Oxide etcher. Figures 2.15 and 2.16 show the fabricated vortex devices. Figure 2.16 shows circular profiles in both photoresist and fused silica. The total height was measured to be 1.76 µm in fused silica. This is within measurement error of the desired height.

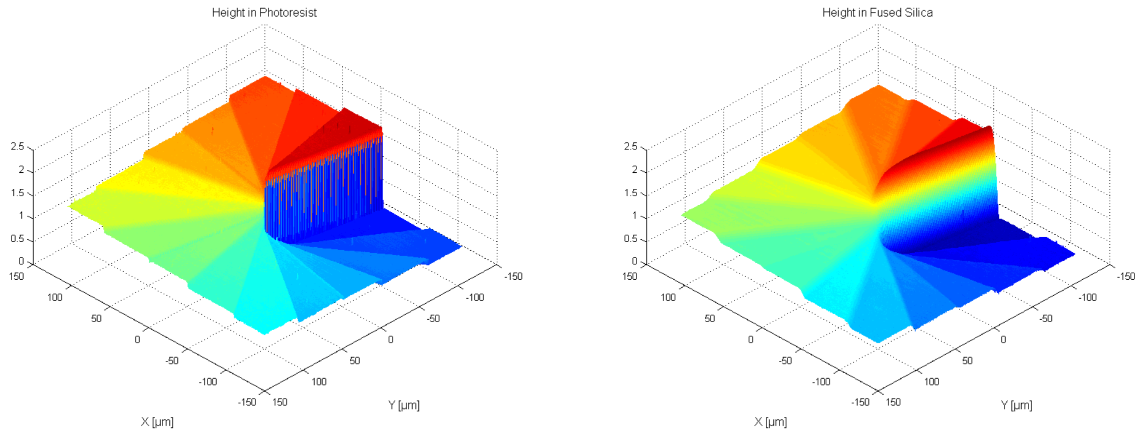


Figure 2.15. three-dimensional images of the 16 level optical vortices in photoresist (LEFT) and in fused silica (RIGHT)

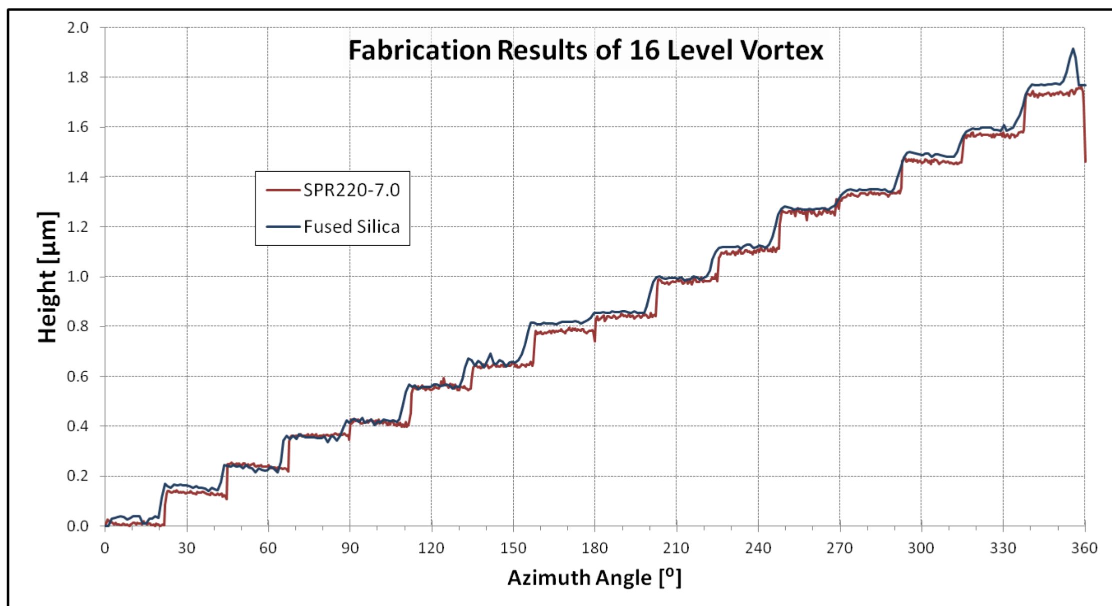


Figure 2.16. Circular profile of a 16 Level Vortex in Photoresist (SPR220-7.0) and Fused Silica

In [57], the authors use a combination of optical vortices and axicons to create a bi-helical optical beam. Our research group fabricated the vortex elements used in their experiment to create a bi-helical beam.

The experiment the authors used requires the use of two optical vortices with charges +1 and -1. Even though the vortices are collinear, their phase functions do not

overlap. The first vortex is annular in shape, while the second vortex has a conventional pupil shape. Both of the vortices were fabricated using the same mask set, an outer vortex and an inner vortex. The inner portion of the vortex element was given an additional dose to make the outer vortex, while the outer portion of the element was given an additional dose to fabricate the inner vortex. The charges between the vortices could be reversed, by simply reversing one of the elements in the optical setup.

## 2.8. Variable Fill Fraction Periodic Structures

Space variant periodic structures have applications to different types of optical elements. One example of space variant periodic structure would be a varying fill fraction subwavelength grating (SWG). In this instance, the variable fill fraction would give rise to a spatially varying effective refractive index. It is possible to create space variant optical elements of this type using the microfabrication techniques discussed in this chapter.

Previously, our research group has combined the use of analog lithography and patterning of binary periodic structures in order to create space variant grating structures [58]. The spatially varying fill fraction was created by first exposing a non-varying lattice into the photoresist, then applying an additional analog exposure to the pattern before development. Projection lithography was used for this, and the period was chosen to be close to the resolution limit of the lithographic system. This approach makes use of the imperfect imaging properties of lithographic systems. When the lattice is close to the resolution limits of the lithographic system, the image of the lattice is not strictly binary; the edges of the holes have a non-vertical slope that leads to partially exposed sidewalls. Figure 2.17 shows a simplified pictorial diagram of this effect. It should be noted that the

sidewalls are not necessarily linear in slope. If an additional flood exposure is made that is below the threshold of the resist, it will have the effect of widening the holes from an increased sidewall exposure without removing portions of the top of the resist as is seen in the figure.

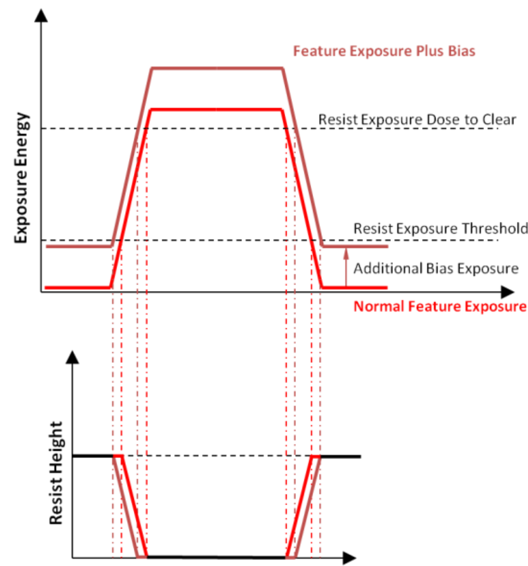


Figure 2.17. Drawing shows the effect of a bias that is less than the threshold of the resist.

Figure 2.18 shows experimental results describing how a lattice’s fill fraction can be altered through additional bias exposures. Notice that the fill fraction increases with increasing bias exposure. If an additional exposure can alter the fill fraction of a grating, then spatially varying bias should be able to create a spatially varying fill fraction. This spatially varying bias exposure is applied using analog lithography and graded index optics can be fabricated using this method.

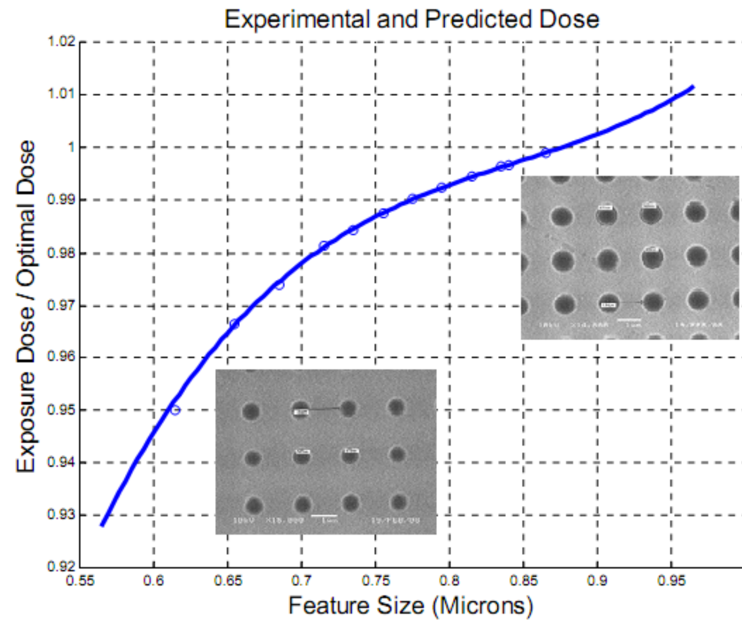


Figure 2.18: Experimental results of varying the fill fraction with an additional exposure [58]

This method of fabrication is advantageous as it allows different types and sizes of lattices to be used with different analog intensity profiles. However, it makes use of the imperfect imaging effects near the resolution limit of the lithographic system; it is not suitable for a wide range of periods. Figure 2.19 shows the effects of the grating period on the modulation of the duty cycles that can be achieved using this fabrication method. As the grating period is increased, the relative size of the sidewall partial exposure decreases. This effect limits the range of duty cycle modulation that can be achieved for longer period devices.

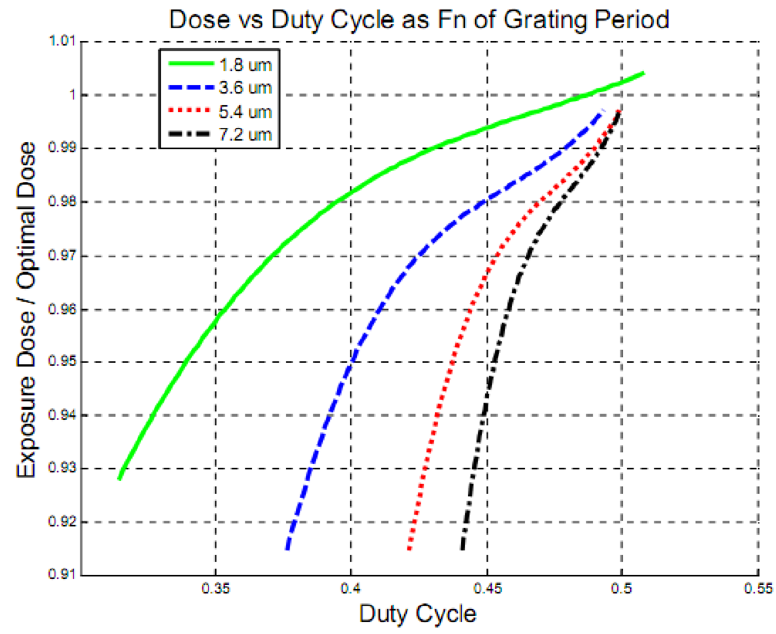


Figure 2.19. Effect of period on duty cycle modulation [58]

# CHAPTER 3: FABRICATED DEVICES

## 3.1. Introduction

In Chapter 1, the concept of a GMRF as a narrowband spectral filter was introduced and explained. The effect of various structural parameters of the device was also studied using rigorous coupled-wave analysis (RCWA). Changes to these structural parameters result in changes to the resonances conditions of the device; the resulting spectrum can be tailored to a desired application through suitable choices in the structural parameters. The sizes and scales of the structural parameters in a GMRF operating at optical wavelengths make it an ideal device to be fabricated using microfabrication technologies and techniques.

The various microfabrication techniques that can be used to create a GMRF were discussed in Chapter 2 of this dissertation. Novel techniques using standard microfabrication systems and tools were also discussed. These techniques offer new, alternative methods of creating three-dimensional structures; as this chapter will show, they can be used to create spatially varying GMRFs.

Standard and conventional GMRFs consist of a subwavelength grating (SWG) combined with a planar slab waveguide. The only spatial variation in the device is the refractive index modulation represented by the SWG. Typically, the period and fill-fraction or duty-cycle of such a device is not varied across the device. The resulting device performs as a spectral filter. Space variant structures can be created so that the

resonance condition changes across the device area. This results in a spectrally and spatially changing reflectance and transmittance profile.

This chapter will focus on the creation, simulation, and testing of space variant GMRFs. Conventional GMRFs will be briefly discussed as an introduction to these more complex devices. The space variant GMRFs proposed here offer an alternative to graded reflectivity mirrors, and it will be shown that unlike conventional GRMs they are not limited to axially symmetric reflection profiles.

Space variant GMRFs have been realized through the spatial modulation of the period and/or fill-fraction of the SWG [32, 33, 59, 60]. However, the fabrication methods used result in limitations in device performance or make them impractical for industry adoption. As such, an alternative method of creating spatially varying resonance conditions is explored. A spatial variation in the thickness of the waveguide layer will also result in a spatial variation in the resonance conditions. The fabrication methods that can be exploited to create a spatially varying waveguide layer were discussed in Chapter 2. Additive and analog lithography are microfabrication techniques that create three-dimensional structures similar to the type of three dimensional structure represented by a spatially varying waveguide thickness.

## 3.2. Conventional Guided Mode Resonance Filters

### 3.2.1. GMRFs for Operation near 1550 nm

GMRFs with resonances located near 1550 nm were fabricated using standard microfabrication techniques. The GMRF consisted of a silicon oxide SWG layer and a silicon nitride waveguide layer on a fused silica substrate. The SWG has a hexagonal

lattice structure for polarization independence at normal incidence. The general GMRF structure is shown in Figure 3.1.

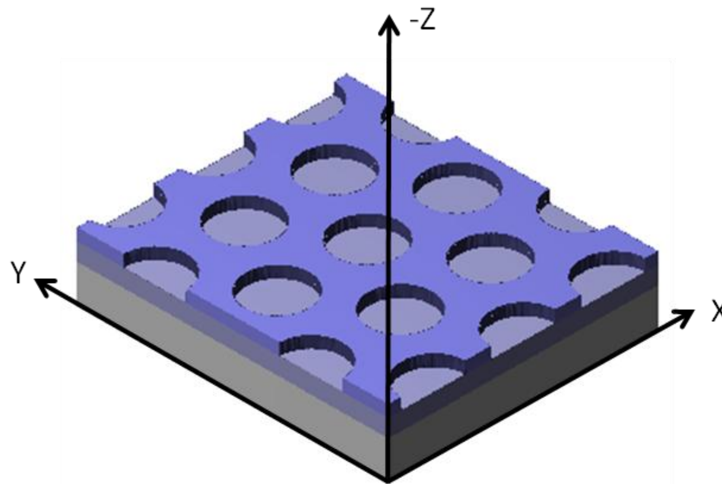


Figure 3.1. Schematic drawing of a Hexagonal GMRF

The GMRF was designed to be polarization independent at normal incidence, operate around 1550nm, and have a sub-nanometer linewidth. Table 3.1 lists the structural parameters chosen for this GMRF. Figure 3.2 displays the simulated spectral response of this GMRF for normal incidence. The resonance is located at 1550 nm with a linewidth of 0.6 nm. A shallow SWG was used to create a narrow linewidth GMRF.

Table 3.1. Structural parameters of Hexagonal GMRF operation near 1550.

| Parameter | Value |
|---|---|
| $d_{WG}$ (Waveguide Thickness) | 405 nm |
| $d_{SWG}$ (SWG Thickness or Etch Depth) | 130 nm |
| $d_{OX}$ (Silicon Oxide Thickness) | 130 nm |
| $\Lambda$ (SWG Period) | 1.15 µm |
| Hole Radii | 350 nm |

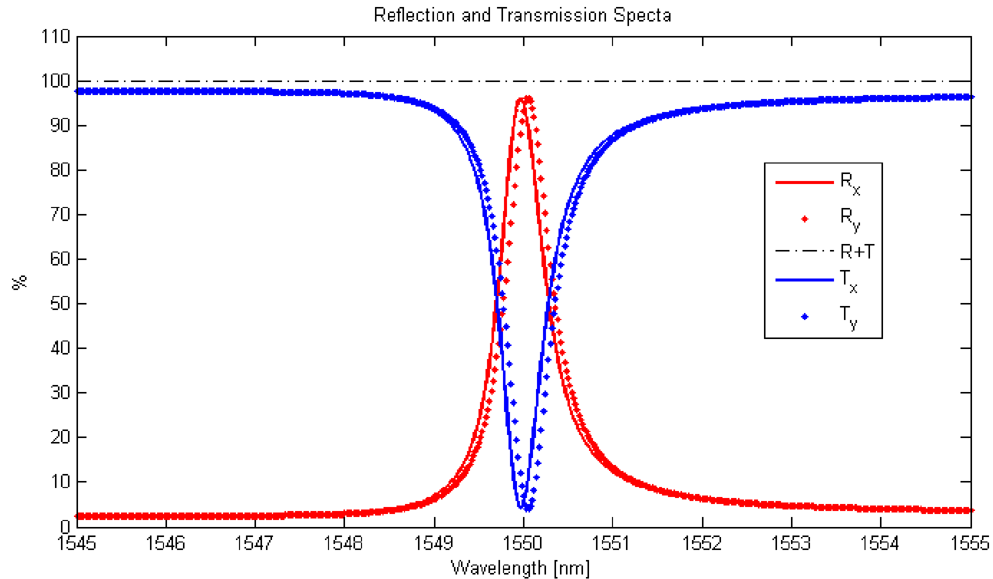


Figure 3.2. RCWA simulation results for a Hexagonal GMRF operating at 1550 nm. The SWG lattice constant is 1.15 µm with hole radii of 350 nm and is etched 130 nm into the Silicon Oxide layer which is 130 nm. The waveguide layer is 405 nm thick.

This GMRF was fabricated using the processes described in Chapter 2. The dielectric layers were deposited onto a 1 mm thick fused silica substrate using the STS PECVD System. The wafer was then treated with a photoresist adhesion promoter, Surpass 3000. Shipley S-1805 positive photoresist was then applied to the substrate at a thickness of 350 nm. The hexagonal lattice structure was then exposed into the photoresist using a quadruple exposure technique on the GCA 6500 g-line Stepper developed for patterning gratings and periods near the resolution limit of this tool [61]. The SWG was then transfer etched unto the silicon dioxide layer using the Unaxis Versaline High Power Oxide etcher. After the remaining photoresist was removed and the wafer was cleaned, it was tested.

Figure 3.3 shows a schematic diagram of the experimental setup used to test the GMRFs. The light source used was an Agilent 8164A Tunable laser with a pigtailed fiber optic output. The light source was connected to the transmission port of fiber optic

circulator. The output of the circulator was then connected to a pigtailed fiber optic collimator; it had an output beam diameter of approximately 350 µm. The GMRF was mounted on a stage with three axes of translation movement and two axes of rotation movement. The fiber collimator was also on a stage with 2-axes of rotational movement and three axes of translational movement. The beam that was reflected off of the GMRF was re-coupled by the collimator into the fiber optic circulator. The fiber optic circulator then transmits the reflected light into a fiber optic cable plugged into the detector module on the tunable laser.

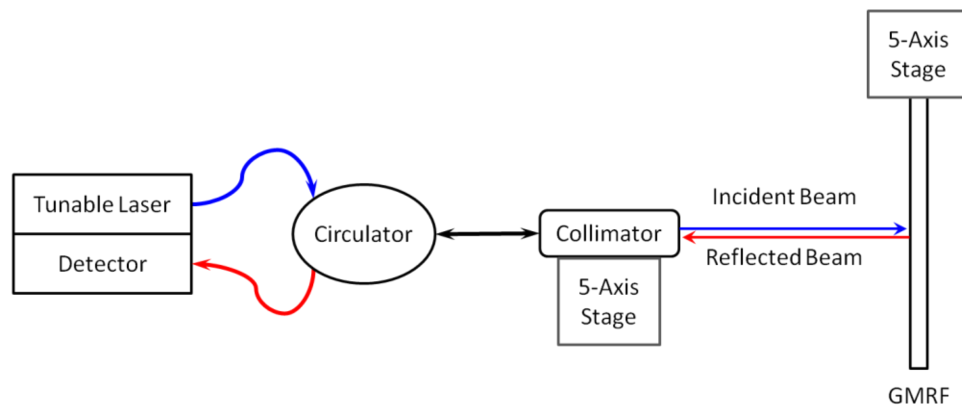


Figure 3.3. Schematic Diagram showing the experimental setup using to test the GMRFs at 1550 nm.

Figure 3.4 shows the measured reflections of two different devices fabricated to operate near 1550 nm. The difference between the two devices is the etch depth of the SWG. The first device had the SWG etched to 170 nm, which is 40 nm into the silicon nitride layer, while the second device was etched to 140 nm which is 10 nm into the silicon nitride layer. Device #1 had a resonance located at 1524.4 nm with a linewidth (FWHM) of 3.1 nm and a peak reflection of 94.8%. Device #2 had a resonance located at 1540.8 nm with a linewidth of 1.1 nm and a peak reflection of 86.8%.

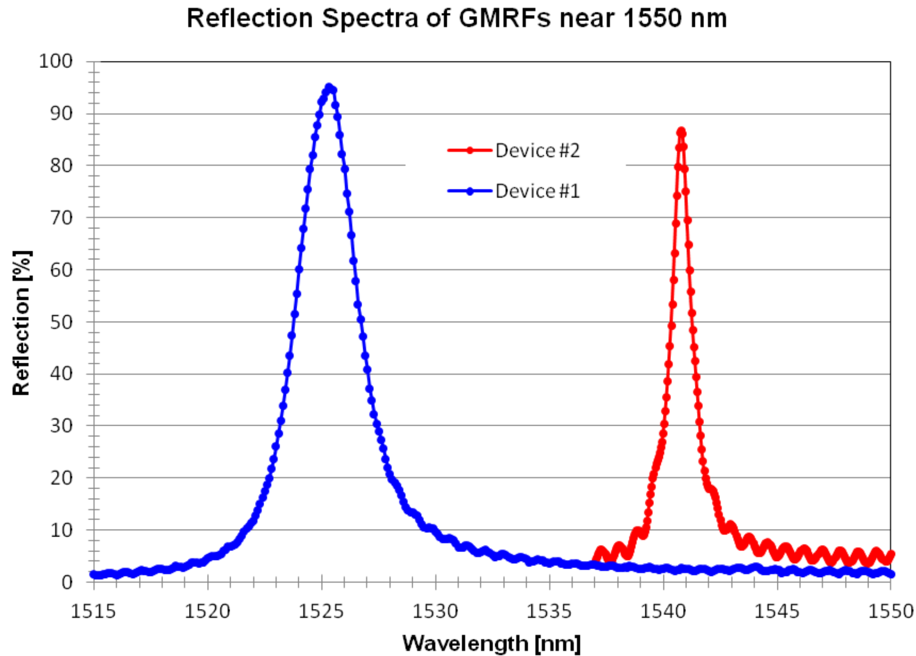


Figure 3.4. Measured reflection spectra for two GMRF devices fabricated to operate near 1550 nm.

In Chapter 1, the effect of the various structural parameters of a GMRF was discussed, including the effect of the SWG thickness. As the SWG thickness decreases, the linewidth of the resonance can also be expected to decrease. From a design perspective, this can be exploited to design narrow linewidth GMRFs, as was the case for this 1550 nm GMRF. This designed called for the SWG to be etched through the entire silicon oxide layer, and not to encroach into the silicon nitride layer. The etch process used is capable of etching both the silicon nitride and silicon oxide materials. Therefore, it is advantageous to simulate the effect of the etch depth on the resonance conditions. Figure 3.5 is an RCWA simulation of the effect of SWG etch depth into the structure described in this section. The silicon oxide and silicon nitride layers are kept at constant thicknesses of 130 nm and 405 nm, respectively, for the simulation, while the SWG etch depth is varied from 120 nm to 180 nm. This corresponds to a variation from 10 nm of

under-etch, where the silicon oxide is not fully etched, to 50 nm of over-etch, where the silicon oxide is fully etched and the SWG is etched into the silicon nitride layer. From Figure 3.5, it can be seen that as the etch depth is increased it causes the resonance to blue shift and increase in linewidth. This is the effect that is seen in the experimental results shown in Figure 3.4.

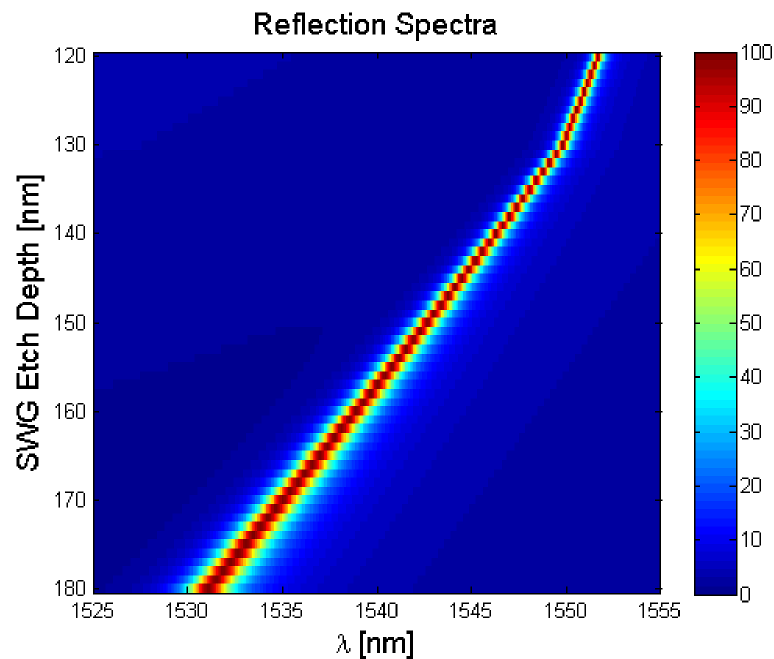


Figure 3.5. RCWA simulation results for a Hexagonal GMRF operating at 1550 nm. The SWG lattice is 1.15 μm with hole radii of 350 nm. The silicon oxide layer is 130 nm. The waveguide layer is 405 nm thick. The etch depth of the SWG is varied from 120 nm to 180 nm.

### 3.2.1. Over-Coated GMRF for Operation near 980 nm

In addition to GMRFs at 1550 nm, devices that operate near 980 nm were also fabricated and tested. The structure for these GMRFs is shown in Figure 3.6. This structure differs from the structures previously mentioned in that the SWG is etched into the substrate and the dielectric layers are then deposited onto the etched substrate. The

period of SWG needed for resonance near 980 nm is beyond the capabilities of the tools used for the fabrication of the GMRFs at 1550 nm. Therefore it was necessary to have the SWG patterned using an ASML 193 nm Stepper-Scanner System at North Carolina State University (NCSU). The ASML system that was used patterns wafers that are 0.5 mm thick with a diameter of 150 mm. The tools used for the deposition and etching of the previous GMRFs are not capable of processing 150 mm wafers. In order to fabricate a device for operating at 980 nm, it was then necessary to alter the design so that the SWG can be patterned first, and then deposit the dielectric layers. Figure 3.6 shows a three-dimensional schematic drawing of an over-coated GMRF.

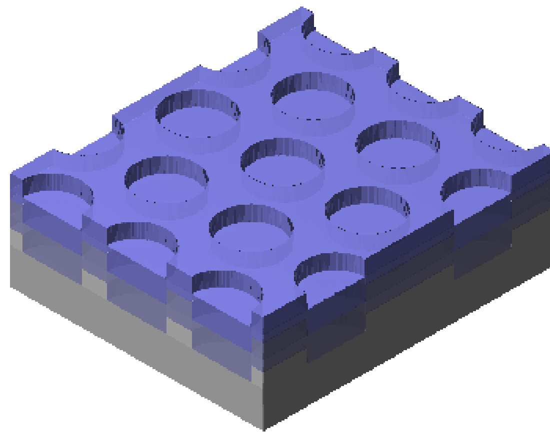

Figure 3.6. Schematic drawing of a Hexagonal GMRF where the SWG is etched into the substrate, and the dielectric layers are deposited onto it. This structure is referred to as an over-coated structure.

Table 3.2 lists the structural parameters of the over-coated GMRF designed to operate near 980 nm. Figure 3.7 shows the simulated spectral response of the GMRF. The simulations predict a resonance located at 968 nm with a linewidth of 15.6 nm.

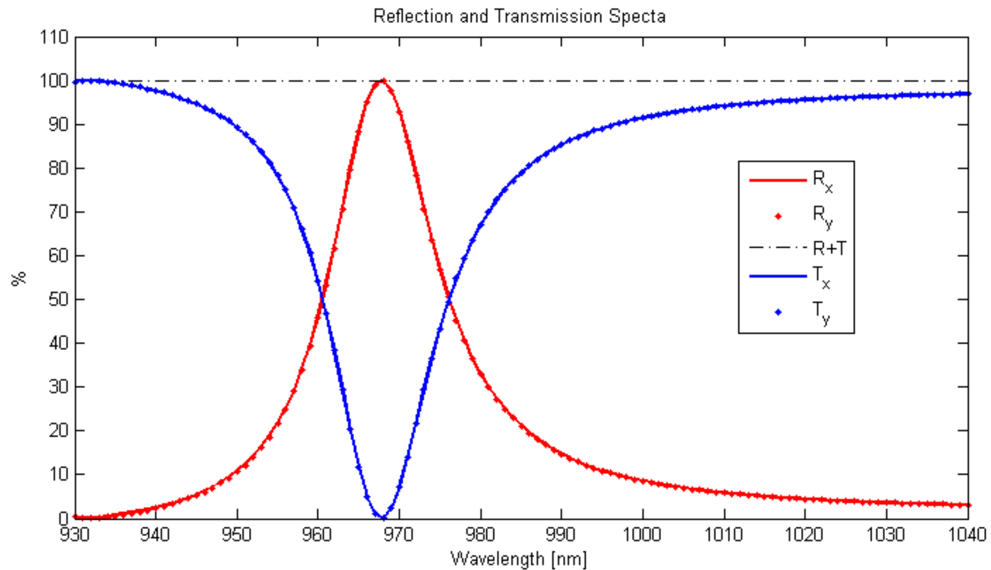


Figure 3.7. RCWA simulation results for an over-coated hexagonal GMRF operating at 980 nm. The SWG lattice constant is 720 nm with hole radii of 190 nm and is etched 150 nm into the fused silica substrate. 145 nm of silicon nitride followed by 150 nm of silicon oxide are on top of the SWG.

Table 3.2. Structural parameters of an over-coated hexagonal GMRF operation near 980 nm.

| Parameter | Value |
|---|---|
| $d_N$ (Silicon Nitride Thickness) | 145 nm |
| $d_{SWG}$ (SWG Thickness or Etch Depth) | 150 nm |
| $d_{OX}$ (Silicon Oxide Thickness) | 150 nm |
| $\Lambda$ (SWG Period) | 720 nm |
| Hole Radii | 190 nm |

The SWG was patterned at NCSU and transfer etched into a 0.5 mm thick, 150 mm diameter fused silica wafer. The wafer was then diced into smaller samples at UNCC. A sample containing two GMRF devices was then mounted on a 1 mm thick, 100 mm diameter silicon wafer so that it could be processed in the STS PECVD tool. A 145 nm thick silicon nitride layer was deposited onto the device, followed by a 150 nm silicon oxide layer. The deposition rates used were calibrated for a 100 mm diameter, 1 mm thick fused silica wafer.

The transmission spectrum of this device was measured with a Woollam Ellipsometer. The device was measured at normal incidence and for both orthogonal polarization states. The results of this are shown in Figures 3.8 and 3.9. Figure 3.8 shows the measured transmission spectrum at normal incidence for the s-polarization. The resonance is located at 978.5 nm with a linewidth of 6.5 nm. Figure 3.9 shows the measures spectrum from 300 nm to 1700 nm, with the range from 1350 nm to 1450 nm omitted. This graph shows that the response of the GMRF is polarization independent at normal incidence. At the resonance location, the notch in the transmission drops to 2.9%; assuming no absorption and all of the energy is in the 0$^{th}$ diffracted order, this corresponds to a reflection peak of 97.1%.

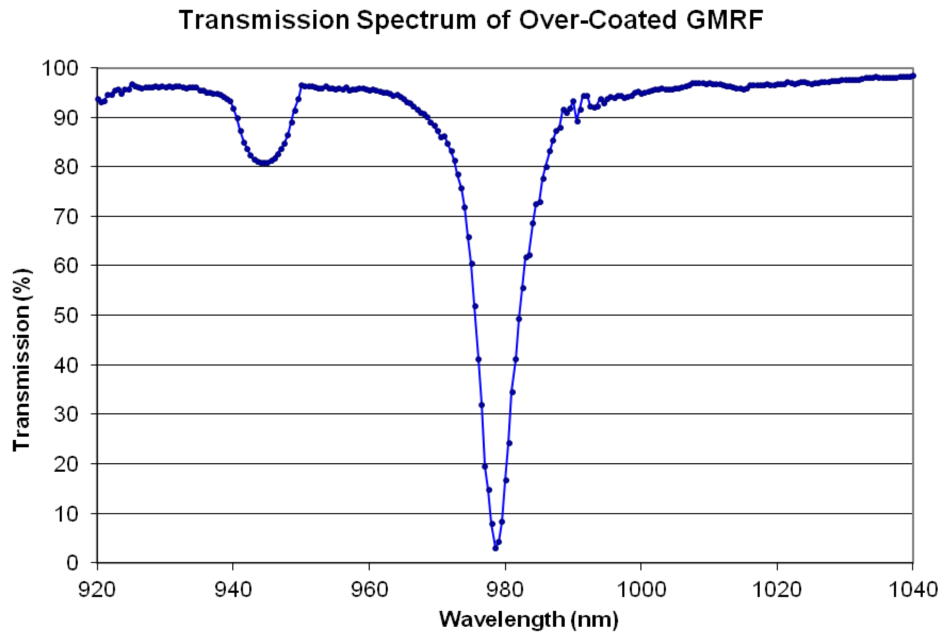


Figure 3.8. Measured transmission spectrum for over-coated GMRF. The resonance is located at 978.5 nm. The s-polarization was used.

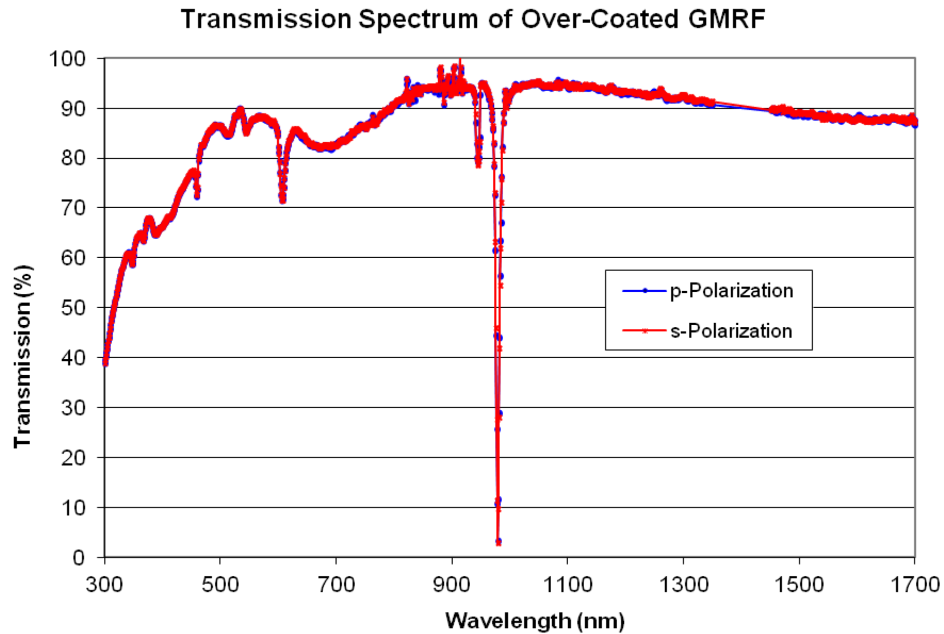


Figure 3.9. Measured transmission spectrum for over-coated GMRF. The resonance is located at 978.5 nm. The s and p polarizations were measured.

The structure that was simulated assumed uniform coating over the SWG with the silicon nitride and silicon oxide as can be seen in Figure 3.6. However, it is possible that the as the layers were deposited, some planarization occurred. Also, the deposition rates that were used were found for a 100 mm diameter, 1 mm thick fused silica wafer. These factors could explain the difference between the measured and predicted spectra.

## 3.3. Variable SWG Fill Fraction Space Variant GMRF

### 3.3.1. Concept

Space-variant GMRFs have been previously presented as an alternative to conventional GRMs [59, 60]. Space variant GMRFs represent new and novel optical elements that can control the spectral, spatial and, potentially, the polarization properties of optical beams. Previous work has demonstrated GMRF based GRMs with axially symmetric reflectivity [59, 60]. It will be demonstrated that these optical devices are also capable of non-axially symmetric structural profiles.

The standard and novel micro-fabrication techniques discussed in Chapter 2 were used to fabricate these optical devices. The structural parameters of a standard GMRF can be varied in three dimensions across the device volume to create a spatially variant GMRF and hence a GRM. A space variant GMRF can be realized by slowly varying the lattice properties, modifying the resonant response as a function of spatially localized parameters. The conceptual performance of such a device is shown in Figure 3.10. The device discussed in this section will vary the fill fraction of the SWG as a function of angle about the axial center of the device. The transmission and reflection of this device will then be a function of local position within the SWG and the incident wavelength.

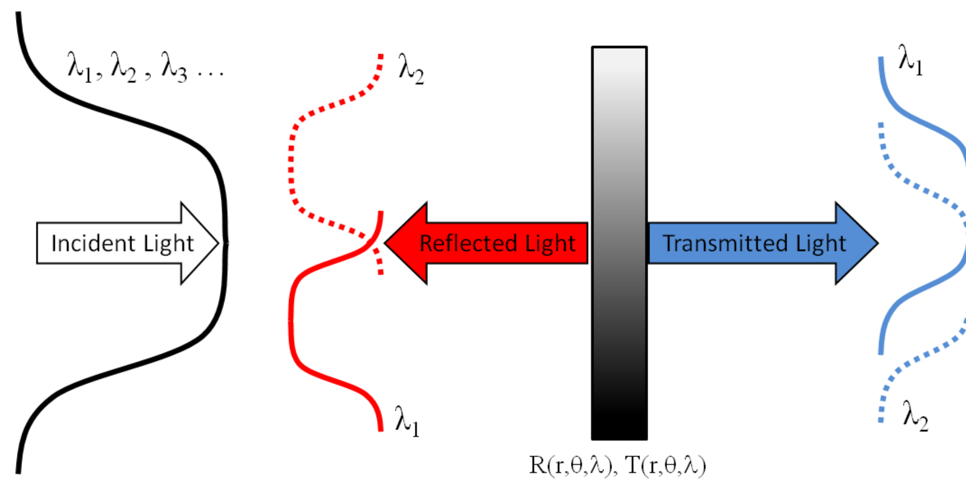


Figure 3.10. Conceptual diagram showing a spectrally and spatially varying optical element

The grating structure used for this device is a hexagonal lattice, so that the resonance conditions of the GMRF are polarization independent (see Chapter 1), for normal incidence of the light wave. The waveguide and SWG layers are composed of silicon nitride and silicon oxide, respectively. A three-dimensional representation of a

conventional GMRF, with a fixed spatial period and grating duty cycle, is shown in Figure 3.11. Table 3.3 lists the values of the structural parameters.

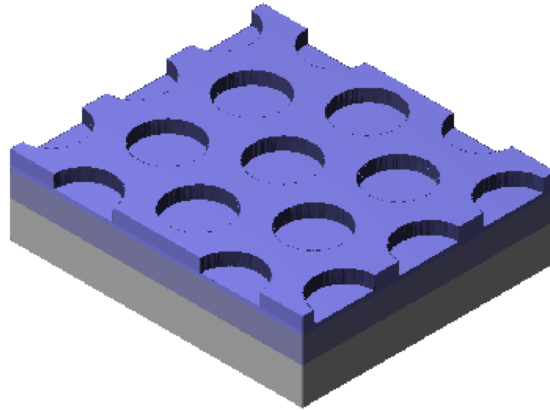

Figure 3.11. Schematic drawing of a Hexagonal GMRF where the SWG is partially etched through the Silicon Oxide Layer

Table 3.3. Structural parameters of Hexagonal GMRF for variable fill fraction GMRF.

| Parameter | Value |
|---|---|
| $d_{WG}$ (Waveguide Thickness) | 375 nm |
| $d_{SWG}$ (SWG Thickness) | 170 nm |
| $d_{OX}$ (Silicon Oxide Thickness) | 240 nm |
| $\Lambda$ (SWG Period) | 1150 nm |
| Hole Radii | 400 nm |

Figure 3.12 shows the RCWA results for a GMRF described above with a 400 nm hole radius. The resonance is located at 1546 nm with a full-width at half-maximum (FWHM) linewidth of 0.57 nm. The simulation shows a slight separation between the two orthogonal polarization states, this is most likely due to a pixilation of the SWG lattice in the RCWA model.

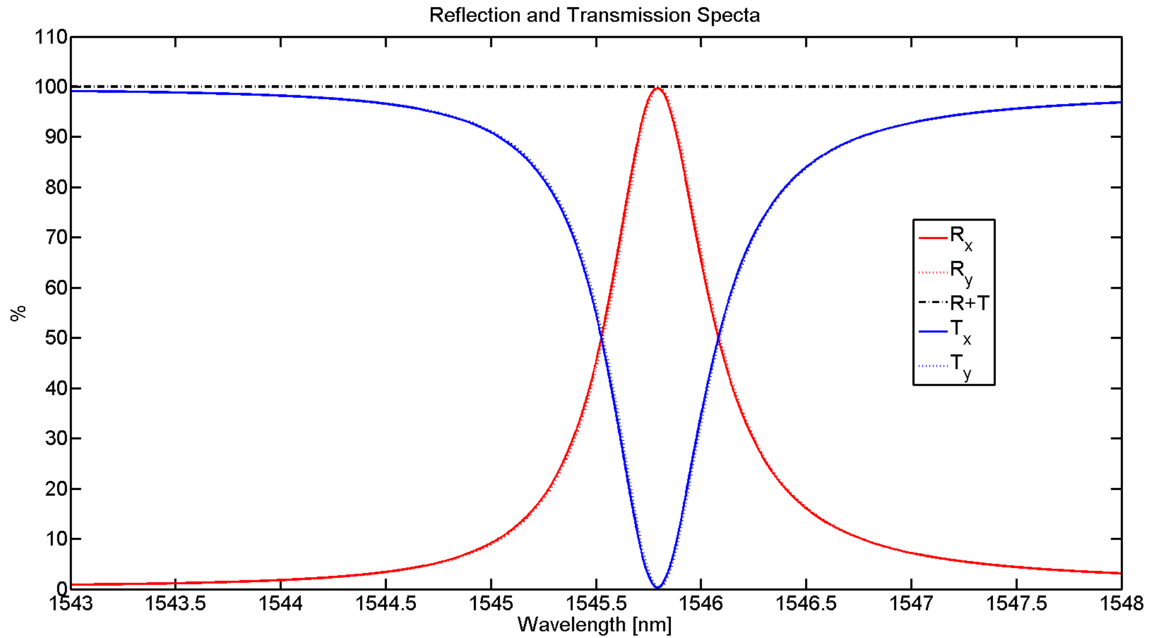


Figure 3.12. RCWA simulation results for a Hexagonal GMRF. The SWG lattice constant is 1.15 µm with hole radii of 400 nm and is etched 170 nm into the Silicon Oxide layer. The waveguide layer is 375nm thick.

As stated previously, the resonance condition for a GMRF is a function of the many structural and optical parameters of the device. In order to achieve a spatial variation of the resonance condition, one or more of these parameters needs to be spatially modulated. For this device, the fill fraction or the diameter of the holes in the GMRF lattice was chosen as the parameter variable. It is assumed and it will be shown, that the resonance condition is a function of the local structural properties across the entire surface of the device. Under this assumption, the impact of the spatial modulation can be investigated. Chapter 1 discussed the effects on the fill fraction or duty cycle of the SWG on the resonance conditions of a GMRF. Figure 3.13 shows the RCWA results from varying the fill fraction of the structure described in Table 3.3. The hole radii are varied between 300 nm and 500 nm, which corresponds to a fill fraction change between 25% and 69%. This results in a continuous resonance shift from 1555 nm to 1538 nm.

The figure also shows that the linewidth of the resonance decreases as the hole radii increase.

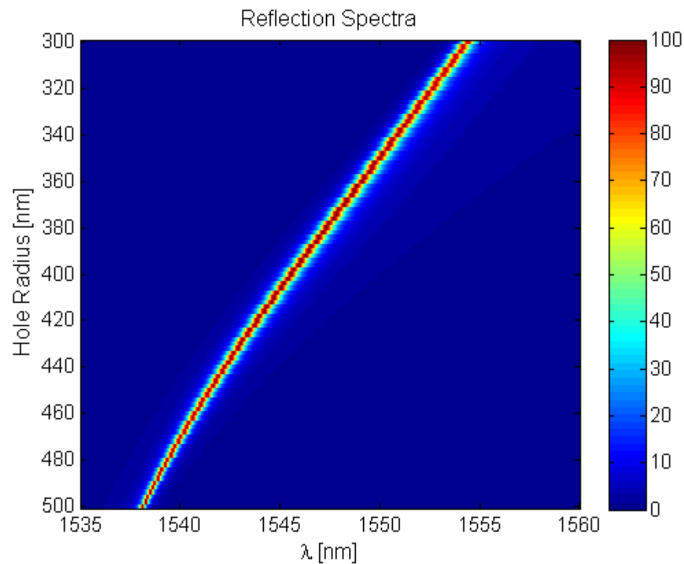


Figure 3.13. RCWA simulation results for a Hexagonal GMRF. The SWG lattice constant is 1.15 μm with hole radii of 400 nm and is etched 170 nm into the Silicon Oxide layer. The hole radii are varied between 300 nm and 500nm.

Accordingly, a spatial modulation of the fill fraction, under the above assumption should create a spatially and spectrally varying reflectivity and transmissivity. Figure 3.14 shows the conceptual drawing of a GMRF with a spatially varying fill fraction.

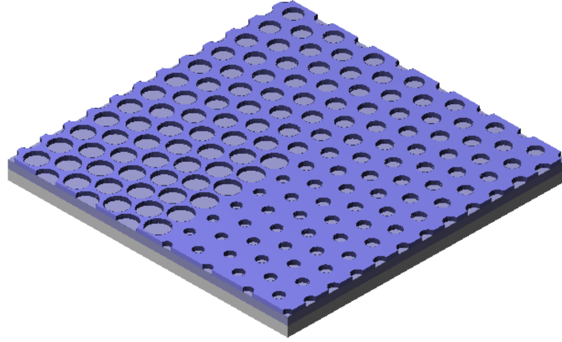

Figure 3.14. Schematic drawing of an azimuthally varying fill fraction GMRF

3.3.2. Device Fabrication

This device was fabricated using processes that are compatible with standard micro-fabrication techniques. These techniques are discussed in more detail in Chapter 2. Figure 3.15 shows the process flow for the fabrication of a GMRF with a spatially varying fill fraction. The dielectric layers were deposited onto a fused silica substrate using an STS PECVD system. The silicon nitride and silicon oxide were deposited to thicknesses of 375 nm and 240 nm, respectively.

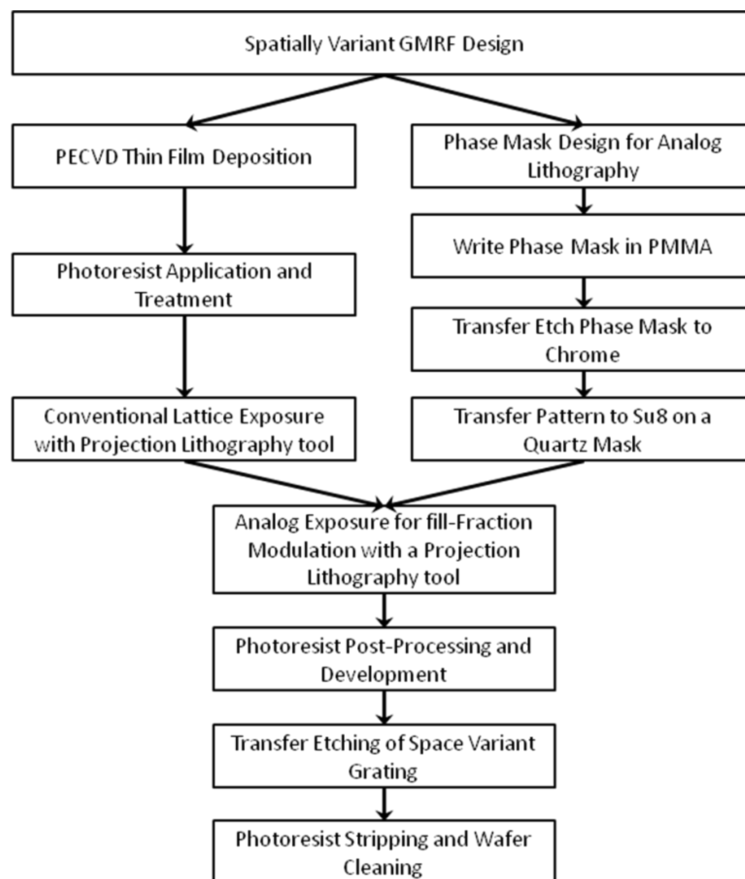


Figure 3.15. Process flow of the fabrication of the spatially varying fill fraction GMRF

The azimuthal pattern distribution was accomplished using the novel analog/binary exposure technique with a projection lithography stepper discussed in Section 2.8. A g-line GCA projection stepper was used to pattern the grating lattice as well as the fill fraction variation. A constant fill fraction SWG is first exposed in Shipley S-1805 positive tone photoresist, using a binary amplitude mask. A quadruple exposure method was used to increase the fidelity of the holes patterned [61]. The fill-fraction variation was achieved via an additional analog exposure. The process of achieving the space variant fill-fraction is further outlined in Section 2.8.

The space variant grating in the resist was then transfer etched into the SWG by the use a Unaxis Versaline High Power Oxide Etcher. The recipe used for this process

was a mixture of freon ($CHF_3$) and oxygen ($O_2$). The SWG was etched to a depth of 170 nm in the silicon oxide layer.

As previously discussed, the azimuthal variation was accomplished using the phase mask technology described in Section 2.8. For this device, an analog intensity distribution in the wafer plane was needed. A phase mask with the appropriate pattern was fabricated. The phase mask pattern was first written in PMMA on chrome on Quartz photomask plate. This initial patterning was done by the Center for Research and Education in Optics and Lasers (CREOL) at the University of Central Florida (UCF) using the LEICA EBPG 5000 tool. The pattern in the PMMA was then transfer etched into the chrome using a commercial chrome wet etchant creating a binary amplitude photomask. The photomask was then used to create the phase mask used for this work. The binary amplitude mask was used as the photomask in a Quintel i-line Contact Mask Aligner. The pattern was transferred into SU8 on a Quartz photomask with the proper thickness for a phase mask. The SU8 serves as the material for the phase grating in the phase mask that is used to create the azimuthally varying fill fraction for this GMRF. Figure 3.16 shows the desired analog intensity distribution next to the center of a hexagonal SWG with an azimuthally varying hole radii. This spatially variation was created using the phase mask described above.

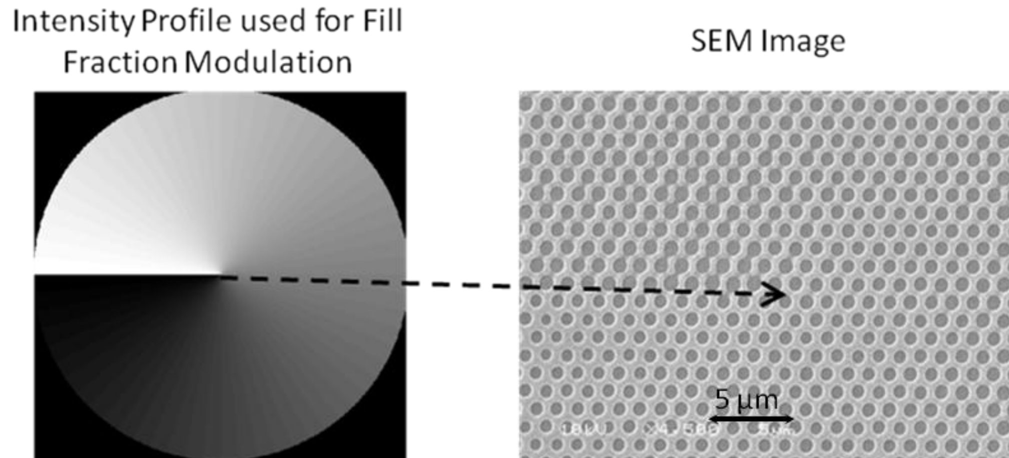


Figure 3.16. (LEFT) Desired analog intensity (RIGHT) SEM of an hexagonal grating with an azimuthal fill fraction variation

After the phase mask was fabricated, the feature sizes were measured on an Olympus LEXT three-dimensional Confocal Microscope. It was found that during the fabrication procedure, the fill fraction of the phase mask had an additional bias that created a non-linear analog exposure profile. Figure 3.17 shows an image from the three-dimensional confocal microscope. The square pillars were measured using this microscope at various azimuth angles. These features sizes were used in Equation 2.5 in Section 2.4 to create the graph shown in Figure 3.18. This graph shows the designed analog intensity profile, analog with the one calculated from measured fill fractions in the phase mask. It shows that the intensity profile should be expected to be non-linear with the azimuth angle.

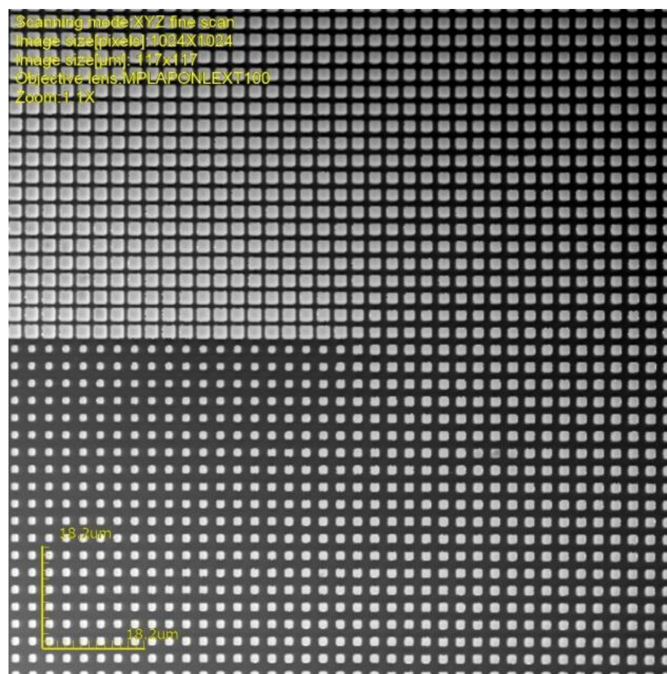


Figure 3.17 Intensity image of the phase mask taking using a Confocal Microscope

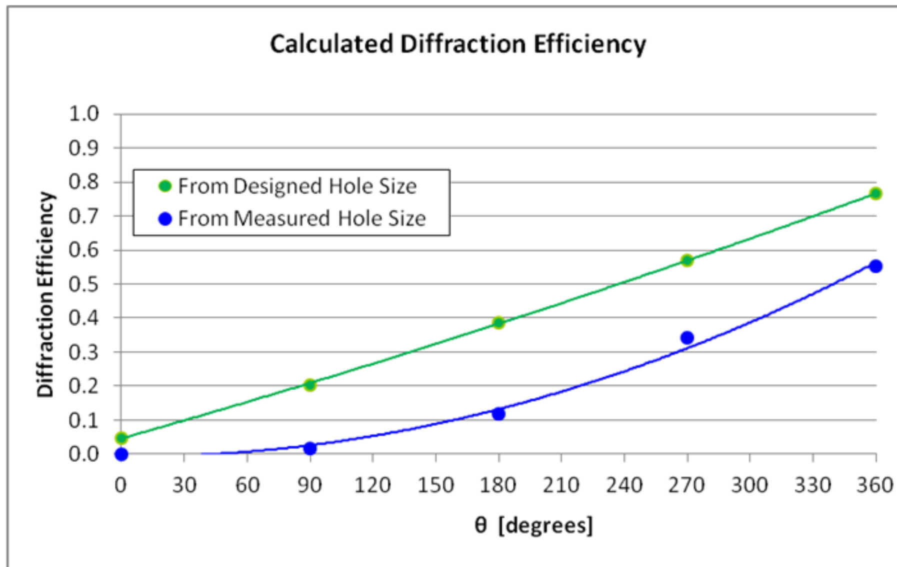


Figure 3.18 Intensity image of the phase mask taking using a Confocal Microscope

After the space variant GMRF was fabricated, the hole size variation was measured using a JEOL Scanning Electron Microscope. Figure 3.19 is a graph displaying the spatial variation in hole size. The spatial variation was found to vary non-

linearly with azimuth angle. The hole radii ranged from 297 nm to 415 nm. From Figure 3.19 and from Figure 3.13, we can expect 10.5 nm of resonance shift across $360^0$ of azimuthal angle change.

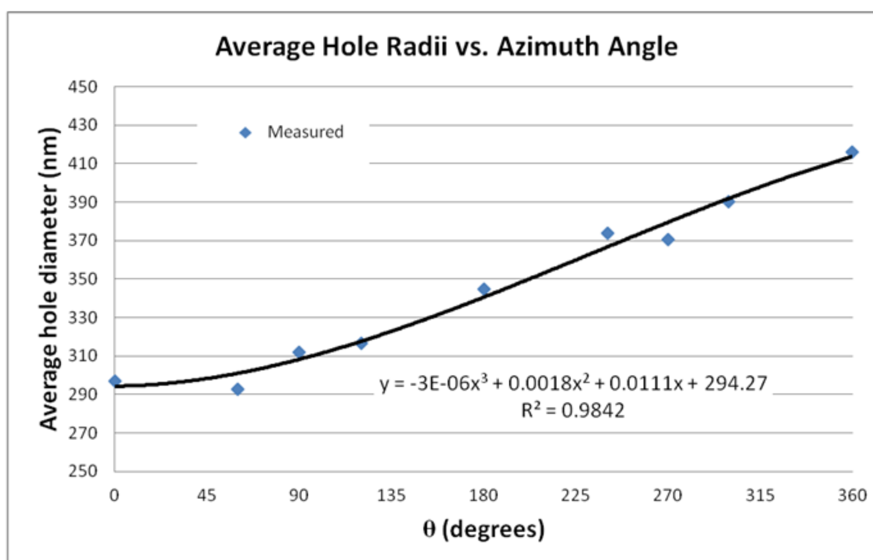


Figure 3.19 Measured hole radii variation across the azimuthally varying GMRF

### 3.3.3. Simulated Beam Profiles

Figure 3.13 showed the effect of the hole radii on the spectra of the GMRF. Figure 3.20 is a reproduction of that figure, but with the new hole radii limits of 290 nm and 420 nm. It shows a more linear change in the resonance with the hole radii.

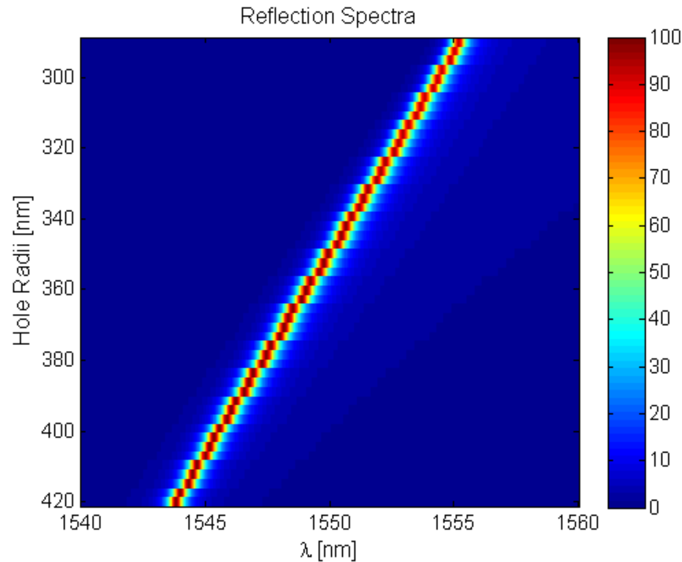


Figure 3.20. RCWA simulation results for a Hexagonal GMRF. The SWG lattice constant is 1.15 μm with hole radii of 400 nm and is etched 170 nm into the Silicon Oxide layer. The hole radii are varied between 290 nm and 420 nm.

The data shown in Figure 3.20 can be used to generate simulated profiles of the transmitted and reflected beams. It was assumed that the spatially and spectrally varying transmitted and reflected beams are a function of the local resonance conditions. It has already been shown in Chapter 1 that the reflection and transmission spectra are a function of the many structural and optical parameters of a GMRF. Equations 3.1 and 3.2 show this general relationship, where $T$ is the transmittance and $R$ is the reflectance.

$$T = T(\lambda, r_h, \Lambda, d_{SWG}, d_{WG}, d_{Ox}) \quad 3.1$$

$$\mathrm{R} = \mathrm{R}(\lambda, r_h, \Lambda, d_{SWG}, d_{WG}, d_{Ox}) \quad 3.2$$

If all of the structural parameters are kept constant other than $r_h$, the hole radii, then Equations 3.1 and 3.2 become functions of only λ and $r_h$. The fit from Figure 3.19 is given in Equation 3.3. This equation gives the hole radii, $r_h$, in nanometers as a function of the azimuth angle, θ, in degrees. This is a fit from the measured data.

$$r_h(\theta) = (-2.6 \times 10^{-6}) \cdot \theta^3 + (1.8 \times 10^{-3}) \cdot \theta^2 + (1.1 \times 10^{-2}) \cdot \theta + 294 \quad 3.3$$

Equation 3.4 shows the relationship between *R*, the reflectivity, and the spatial variations. For example, Figure 3.20 is an example of the function $R(\lambda, r_h)$. This relationship shows the reflectivity as a function of the wavelength and azimuth angle.

$$R(\lambda, r_h) \rightarrow R(\lambda, r_h(\theta)) \rightarrow R(\lambda, \theta) \quad 3.4$$

$$T(\lambda, r_h) \rightarrow T(\lambda, r_h(\theta)) \rightarrow T(\lambda, \theta) \quad 3.5$$

Equation 3.3 can also be used to create a two-dimension plot of the hole radii as a function of the spatial parameters. Figure 3.21 shows the results of this plot. The center of the plot represents the center of the device. The start of the variation was rotated to better match the orientation of the device in the lab.

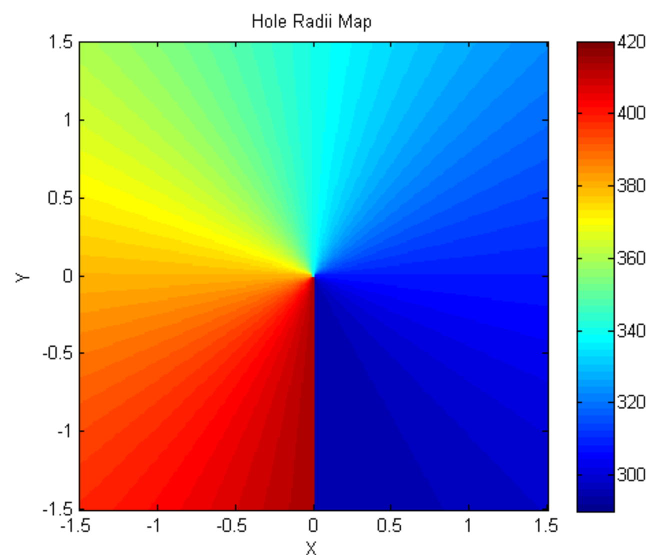


Figure 3.21. Spatial variation of the hole radii in the GMRF.

Using the information from Figures 3.19 and 3.20 a graph showing the expected resonance wavelength versus azimuth angle was created. This was done using the results

from the simulation in Figure 3.20 and the data shown in Figure 3.19 to create the graph shown in Figure 3.22. This graph shows that the resonance can be expected to shift 10 nm with a 360$^o$ rotation in the azimuth angle. The resonance does not shift linearly with the azimuth angle, which is expected from the non-linear hole radii variation shown in Figure 3.19.

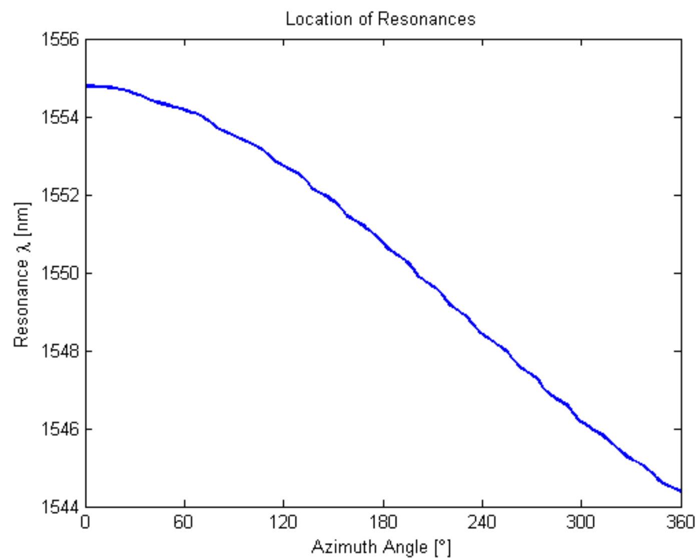


Figure 3.22. Expected resonance wavelength versus azimuth angle.

The spatial profile of the hole radii variation shown in Figure 3.21 and the simulation results shown in Figure 3.20 can be used with the relationship shown in Equation 3.4 to create an expected spatially and spectrally varying reflectance and transmittance profile. Each reflectance and transmittance profile was created for a single, separate wavelength. The simulation results shown in Figure 3.20 were used to determine the reflectance and transmittance as a function of hole radii for each wavelength. The reflectance values were then mapped to the two-dimensional hole size variation shown in Figure 3.21. MATLAB's cubic interpolation routines were used to fill

in the reflectance values for hole radii that were not simulated, but appear in the spatial variation.

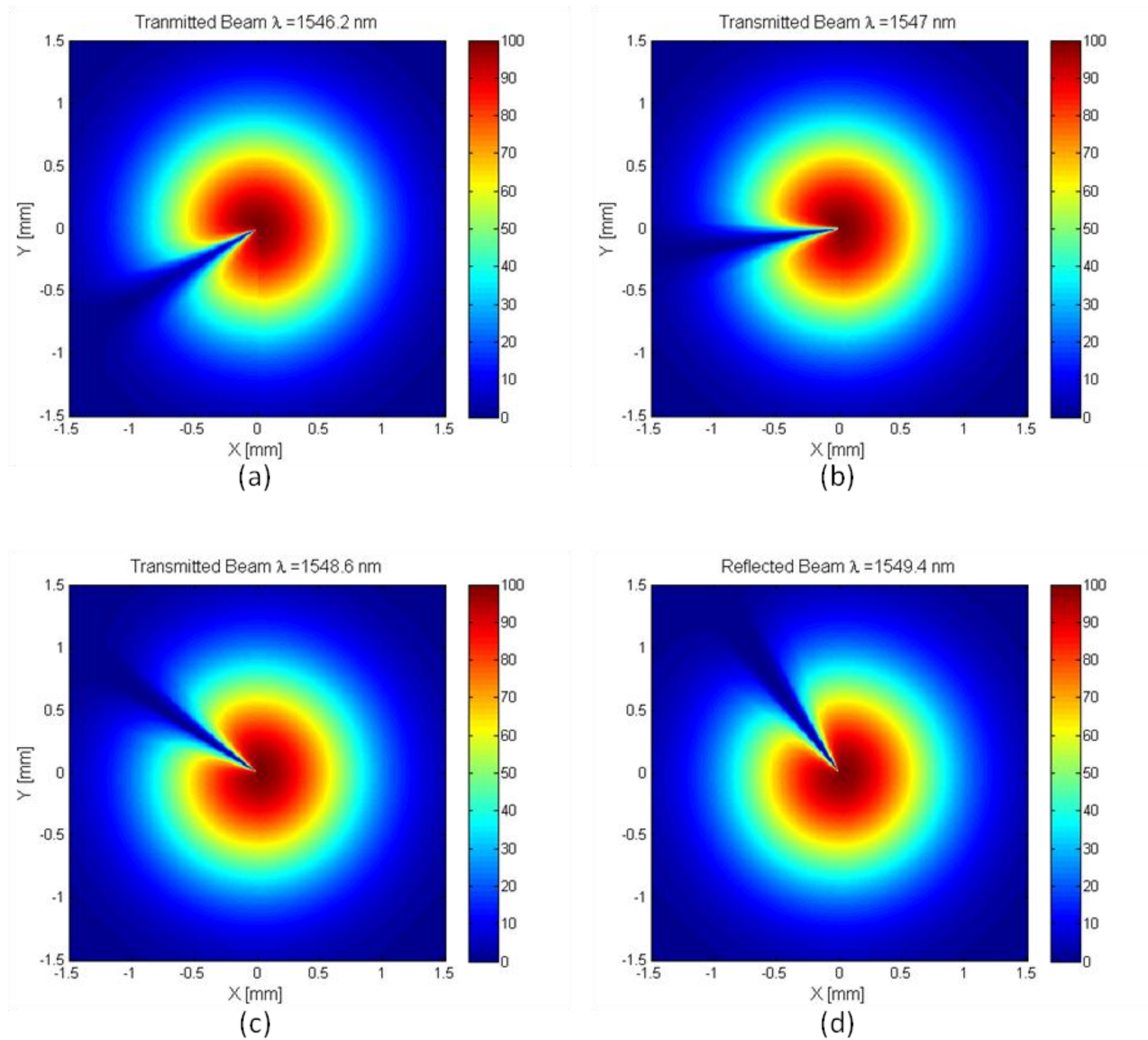


Figure 3.23. Simulated Transmitted Beam profiles of a hexagonal GMRF with an azimuthally varying fill fraction for four different wavelengths: (a) 1546.2 nm, (b) 1547.0 nm, (c) 1548.6 nm, and (d) 1549.4 nm.

### 3.3.4. Experimental Results

The space variant GMRF was interrogated with a fiber tunable laser and a CCD camera. The experimental setup is shown in Figure 3.24. An Agilent 8164A Tunable

Laser was used as the source for the experimental setup. The source was collimated using a Micro Laser Systems FC5 collimator with an FC connector. A SP-1550M Spiricon CCD was used to capture images of the transmitted beam. The beam expander and collimator were located 5 cm before the GMRF and the initial beam waist diameter was 2.4 mm.

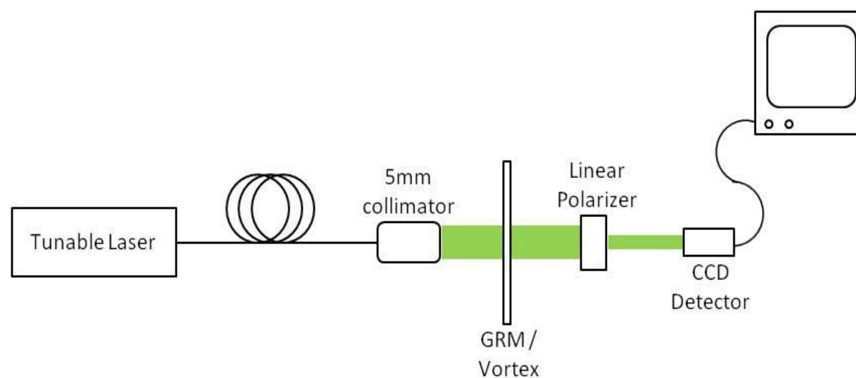


Figure 3.24 Measured hole radii variation across the azimuthally varying GMRF

Figure 3.24 also shows a linear polarizer after the GMRF. During the testing of the GMRF, it was found that the linear polarizer increased the image quality of the transmitted beam. This is most likely due to slight alignment errors during the patterning of the lattice. Figure 3.25 shows the transmitted beam profiles at four different wavelengths: 1533.0 nm, 1535.4 nm, 1533.8 nm and 1536.2 nm. From these images we can estimate that the resonance shifts approximately 3.2 nm over a $90^{0}$ change in azimuth angle, giving the resonance change at 28 degrees/nm. This corresponds to roughly 12 nm of resonance shift for a $360^{0}$ change in azimuth angle, which is similar to the expected results of 10.5 nm of resonance shift. There was also a noticeable blue shift of approximately 3 nm from the expected results. This could be from slight variations from

the desired silicon oxide thickness, silicon nitride thickness, and the SWG etch depth. The images shown in Figure 3.25 include interference fringes across the beam profiles, which are caused by diffraction from the linear polarizer in the setup.

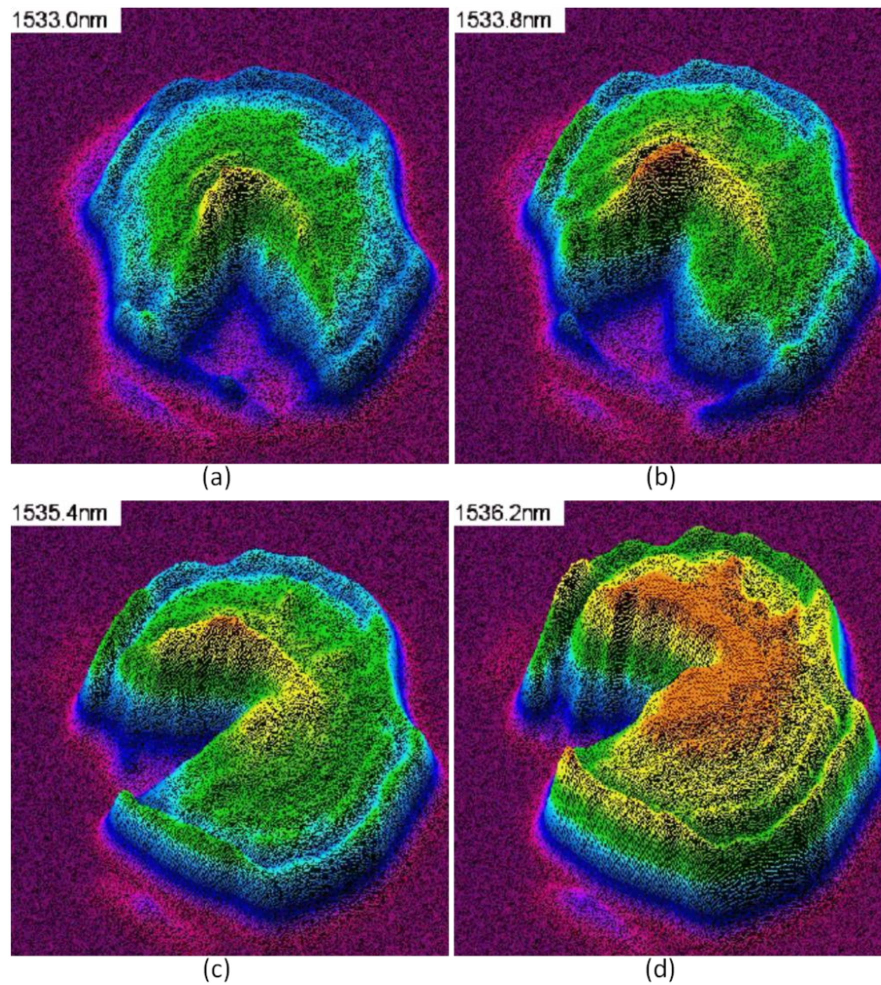


Figure 3.25. Measured Transmitted Beam profiles of a Hexagonal GMRF with an azimuthally varying fill fraction for four different wavelengths: (a) 1533.0 nm, (b) 1533.8 nm, (c) 1535.4 nm, and (d) 1536.2 nm.

## 3.4. Variable Waveguide Thickness Space Variant GMRF

### 3.4.1. Motivation and Concept

Previous efforts to create a spatially varying GMRF all focused on a spatial modulation of the SWG [32, 33, 59, 60]. These methods either require direct writing a SWG with a varying duty cycle and period via e-beam technology (see Chapter 2), or spatially varying fill fraction of the SWG using analog lithography (see Chapter 2). Devices fabricated using e-beam technology cannot typically be produced in mass quantities needed for industry adoption. Also, the method of using analog lithography to spatially varying the fill fraction of the SWG is limited to a narrow range of periods, and thus is limited to a narrow range of wavelength regimes. Consequently, an alternative approach using the fabrication methods discussed in Chapter 2 is presented here as an alternative to previous methods of creating a spatially varying GMRF.

In Chapter 1, it was shown that the resonance condition of a GMRF is a function of the various structural and optical parameters of the device. It should then be possible to create a spatially varying GMRF though a spatial modulation of one of these parameters. A possible candidate for this would be the waveguide thickness. Figure 3.26 shows a three-dimensional representation of the type of GMRF structure with a spatially varying waveguide layer. The fabrication methods that can be used to create a variable thickness waveguiding layer have been previously explained (see Chapter 2). The spatially varying waveguide structure used in this proposed device could be fabricated using analog lithography to create a continuous profile or with additive lithography to create a multilevel structure. This dissertation will focus on a structure with an azimuthally varying waveguide thickness.

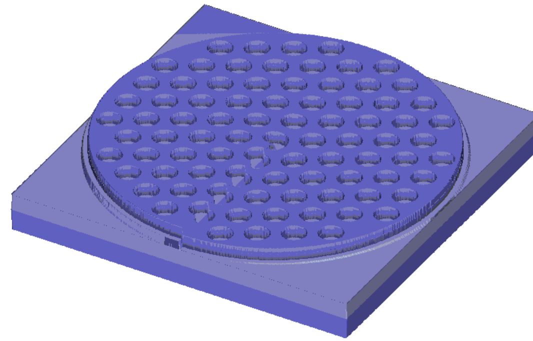

Figure 3.26. Schematic drawing of a GMRF with an azimuthally varying waveguide layer

### 3.4.2. Over-Coated Silicon Nitride on Fused Silica SWG GMRF

In order to study the effect of the waveguide thickness on the resonance conditions of GMRFs, a simple experiment was performed. In the typical structures that are fabricated, the waveguide layer is normally deposited during the first fabrication step. However, with the over-coated structures described in Section 3.2.1, the SWG is first etched into the substrate, and then the dielectric layers are deposited. This fabrication process makes it possible to measure the reflection or transmission spectra for several dielectric layer thicknesses for the same device. Furthermore, if the structure used has only a single layer deposited on the SWG etched into the fused silica substrate, then the spectra can be measured for one nitride thickness, then more silicon nitride can be deposited and the device can be re-measured. This process can be repeated to observe the effects of the silicon nitride thickness on the resonance conditions. In this structure, the silicon nitride provides the high index material necessary for the core of the waveguide.

Figure 3.27 shows cross sectional of the structure used for this device. The device was designed to have resonances around 1.0 μm. The period of the SWG is 720 nm; the hole radii is 170 nm; and the SWG is etched 150 nm into the substrate. A layer of silicon nitride provides the higher refractive index material needed to create a guided mode.

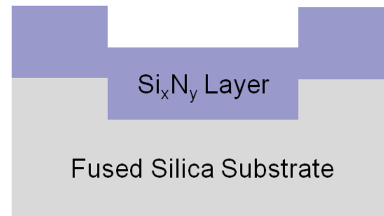


Figure 3.27. Cross-section drawing of an over coated GMRF with a single silicon nitride layer

Figure 3.28 shows an RCWA simulation of the device shown above. The silicon nitride thickness for this device is 220 nm. This design contains two resonances that are separated by approximately 60 nm. The resonance that will be discussed in this dissertation is the resonance at the longer wavelength with the larger linewidth. It shows a resonance at 993.5 nm with a linewidth of 25 nm. The simulations were run with the source at normal incidence to the device, and as can be seen from the graph, the spectral response is independent of polarization.

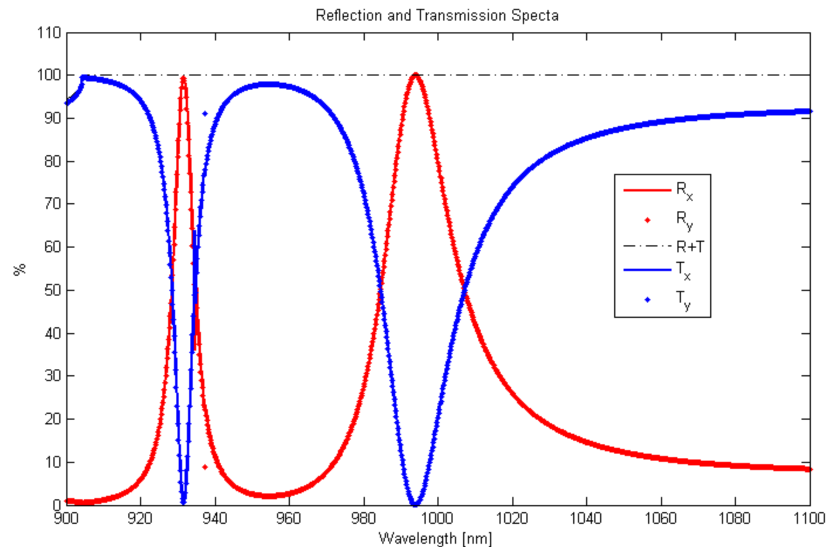


Figure 3.28. RCWA simulation results of an over-coated GMRF with a single silicon nitride layer. The SWG period is 720 nm; the hole radii is 170 nm; and the silicon nitride layer is 200 nm.

Figure 3.29 shows the RCWA simulation results of varying the thickness of the silicon nitride layer. This shows that the resonance shifts linearly with increasing silicon nitride thickness at a rate of 0.7583 nm/nm.

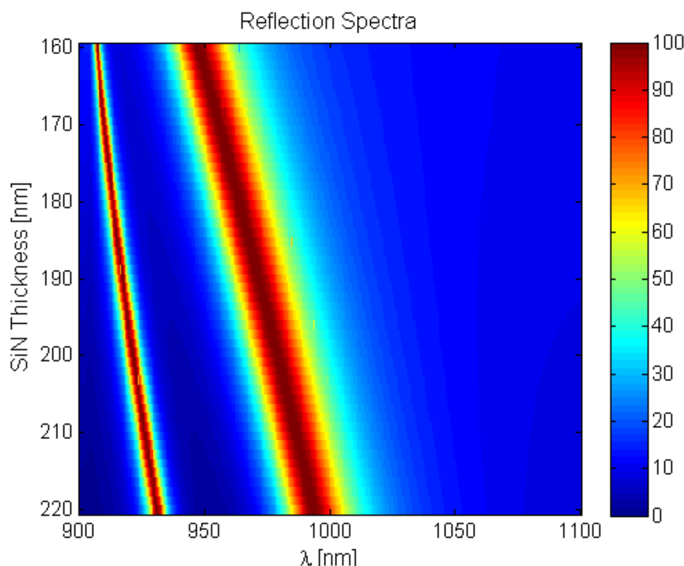


Figure 3.29. RCWA simulation results of an over-coated GMRF with a single silicon nitride layer. The SWG period is 720 nm; the hole radii is 170 nm; and the silicon nitride layer is varied between 160 nm and 220nm.

The device was fabricated using facilities at North Carolina State University and the University of North Carolina at Charlotte. The SWG was patterned on an ASML 193nm Stepper-Scanner at NCSU. The SWG was also transfer etched into the substrate at NCSU using a Trion Reactive Ion Etching system. The substrate was a 6" fused silica wafer with a thickness of 0.5 mm; because this wafer size is incompatible with the systems at UNCC, the patterned wafer was diced into smaller samples. A sample containing two devices was mounted on a 1 mm thick, 4 in. diameter silicon wafer so that it could be processed in the STS PECVD deposition system.

Initially, only 160 nm of Silicon Nitride was deposited on the sample. The transmission spectrum was then measured using a Woollam Ellipsometer at normal incidence. The results of this are shown in Figure 3.30. After the spectrum was measured, and addition 20 nm of silicon nitride were deposited onto the wafer for a total thickness of 180 nm and the spectrum was re-measured. This was repeated for silicon nitride total thickness of 200 nm and 220 nm. The results are shown in Figure 3.30. The spectrum for the 220 nm thickness silicon nitride shows a noticeable double peak in the resonance.

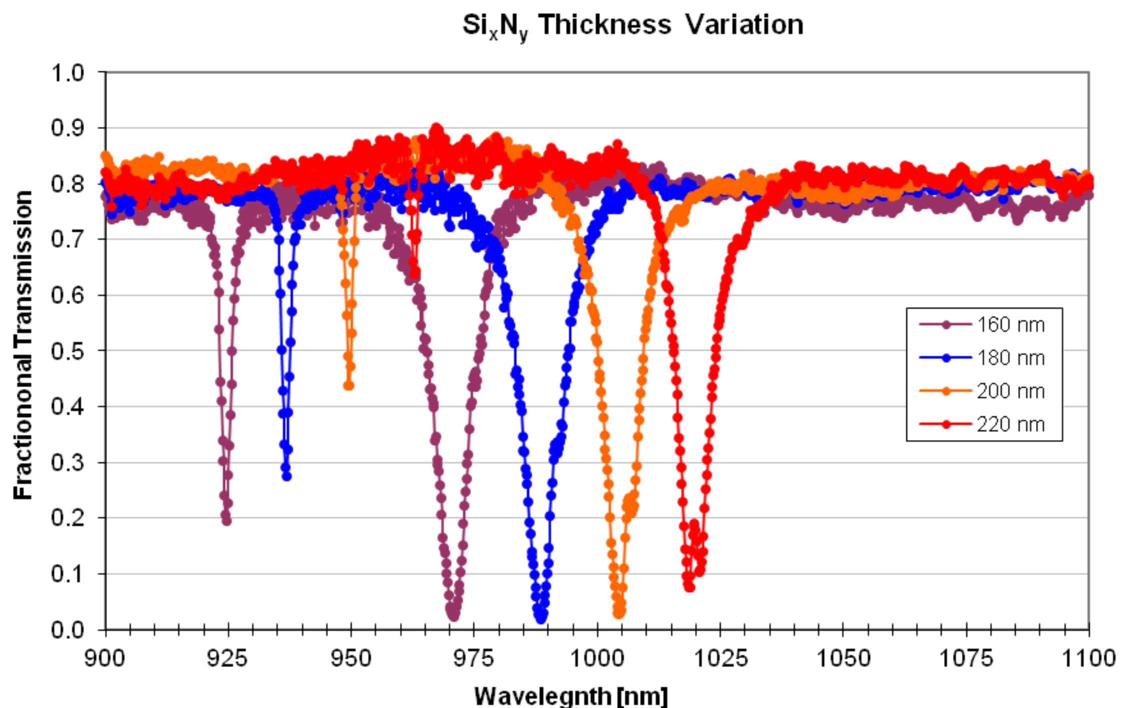


Figure 3.30. Experimental results of an over-coated GMRF with resonance near 1.0 µm. The transmission spectra were measured for the same device after varying the silicon nitride thickness between 160 nm and 220nm.

The spectra that are shown in Figure 3.30 display two resonances for each silicon nitride thickness in the wavelength regime between 900 nm and 1100 nm. The resonance

at the shorter wavelength has a narrower linewidth and a less efficient resonance. The efficiency of the resonance is affected by the light source of the ellipsometer. The Woollam ellipsometer used in this experiment uses a broad band source and a monochrometer to filter the wavelengths. The result is that while a narrowband of light is incident upon the sample, the linewidth is not much smaller than the narrow linewidth of the GMRF. The measured spectrum is a convolution of the GMRF resonance and the spectrum of the light source. This effectively reduces the efficiency of the resonance as well as broadening it.

Figure 3.31 shows the measured resonance location and the linewidth of each resonance. The resonance location was determined by finding the minimum the transmission spectrum. The linewidth was determined by first calculating the reflection (*1-T*) spectrum, assuming no absorption, from the transmission spectrum, then finding the FWHM of the resulting peaks. This data shows that the resonance location increases linearly with increasing silicon nitride thickness. The resonance shifts at a rate of 0.796 nm/nm, while the predicted rate was 0.767 nm/nm. Also, all of the resonance locations are red-shifted from the predicted values by 25 nm. This is most like due to planarization of the silicon nitride coating during deposition.

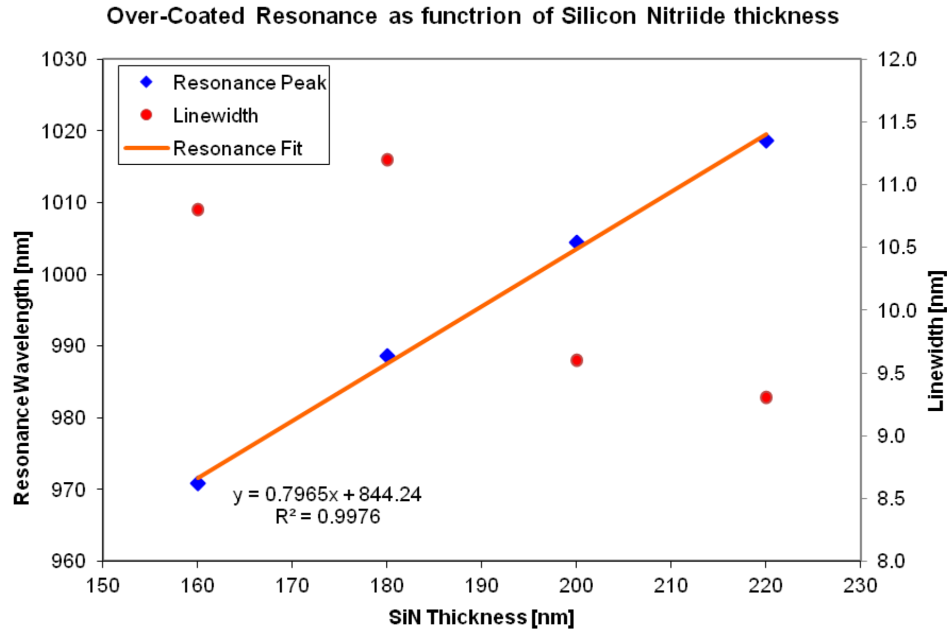


Figure 3.31. Experimental results of an over-coated GMRF with resonance near 1.0 µm. This graph shows the resonance location and linewidth as a function of the silicon nitride thickness.

### 3.4.3. Silicon Oxide SWG with Silicon Nitride Waveguide Layer

Conventional designs previously used by this research group for GMRFs have primarily used a silicon oxide/silicon nitride/fused silica material system. This material system allows for resonances with narrow linewidths. Figure 3.1 shows the non-varying lattice that will be used for this design. The waveguide layer for this device would be constructed from silicon nitride while the SWG would be constructed from silicon oxide. Section 3.3 showed that a spatially varying GMRF can be created by taking this conventional structural and spatially varying the fill fraction of the SWG. Section 3.4.2 showed that the resonance of a GMRF can be altered by varying the silicon nitride layer in the GMRF device. This section will show the simulated results from varying the waveguide thickness of a conventional GMRF.

Table 3.4 shows the structural parameters for the non-varying structure that the space variant structure is based on. Figure 3.32 shows the spectral response of this non-varying structure. The resonance is located at 1548.8 nm with a linewidth of 1.6 nm.

Table 3.4. Structural parameters of Hexagonal GMRF operation near 1550.

| Parameter | Value |
|---|---|
| $d_{WG}$ (Waveguide Thickness) | 240 nm |
| $d_{SWG}$ (SWG Thickness or Etch Depth) | 150 nm |
| $d_{OX}$ (Silicon Oxide Thickness) | 150 nm |
| Λ (SWG Period) | 1150 nm |
| Hole Radii | 350 nm |

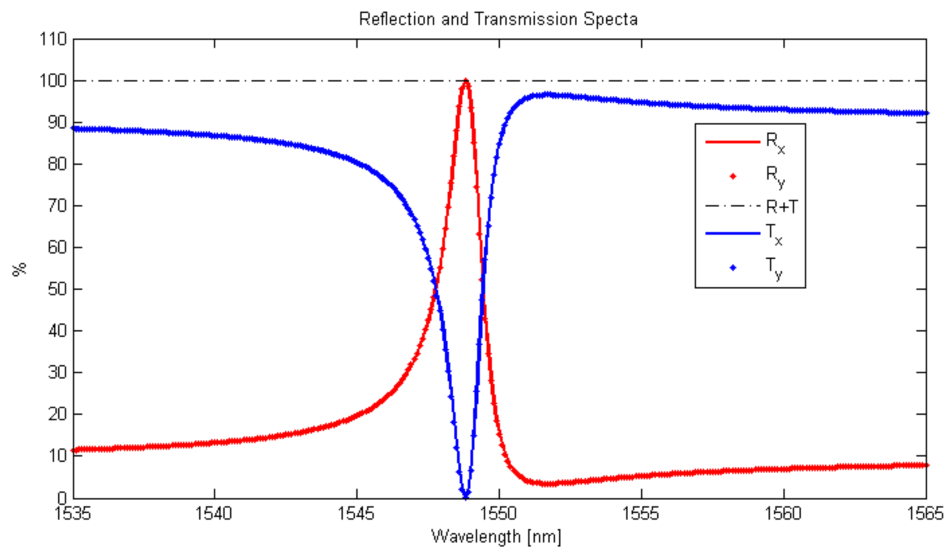


Figure 3.32. RCWA simulation results for a hexagonal GMRF. The SWG lattice constant is 1.15 µm with hole radii of 350 nm and is etched 150 nm into the Silicon Nitride layer. The waveguide layer is 240nm.

Section 3.4.2 showed that the thickness of the silicon nitride layer can be varied to change the location of the resonance. Figure 3.33 shows how the reflection spectra of the GMRF changes with a change in the waveguide thickness. The thickness of the waveguide was varied from 200 nm to 300 nm, which resulted in the location of the

resonance changing from 1514 nm to 1596 nm. This corresponds to linear rate of 0.82 nm/nm (resonance shift/waveguide thickness change).

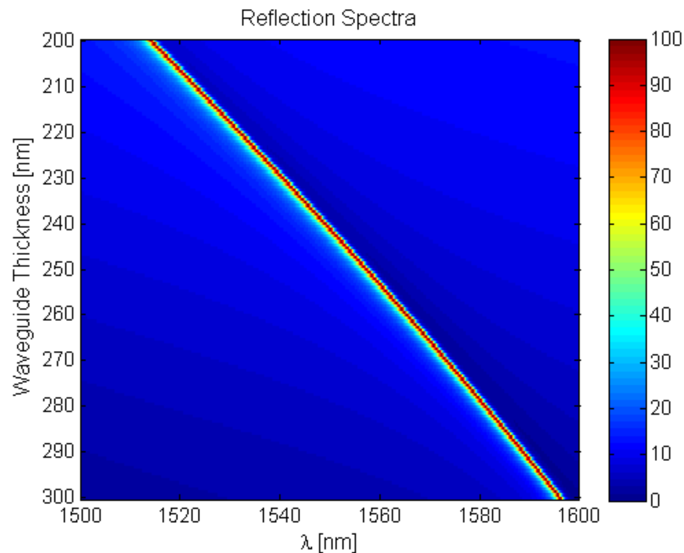


Figure 3.33. RCWA simulation results for a hexagonal GMRF. The SWG lattice constant is 1.15 μm with hole radii of 350 nm and is 150 nm thick. The waveguide layer is varied between 200 nm and 300nm.

Figure 3.34 shows a conceptual drawing of an azimuthally varying GMRF using this convention structure. Figure 3.35 shows the specific waveguide thickness variation used to simulate the beam profiles. The variation of the waveguide layer is 200 nm to 300 nm. This variation is not continuous, and represents the type of variation that would be expected from using additive lithography to create the spatially varying waveguide structure. This structure has 16 levels.

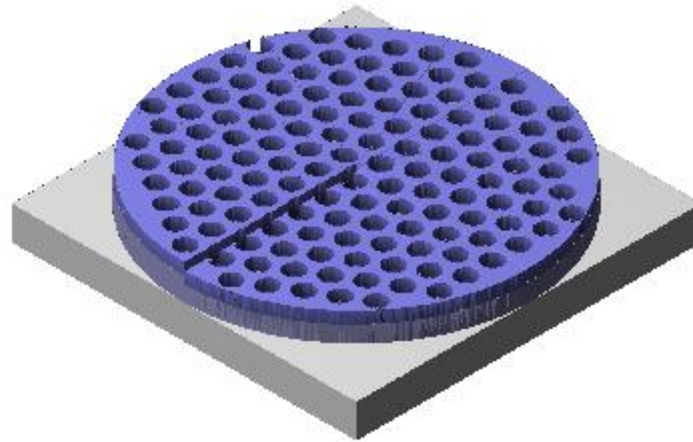

Figure 3.34. Schematic drawing of a GMRF with an azimuthally varying waveguide layer. The SWG is silicon oxide and the waveguide layer is silicon nitride.

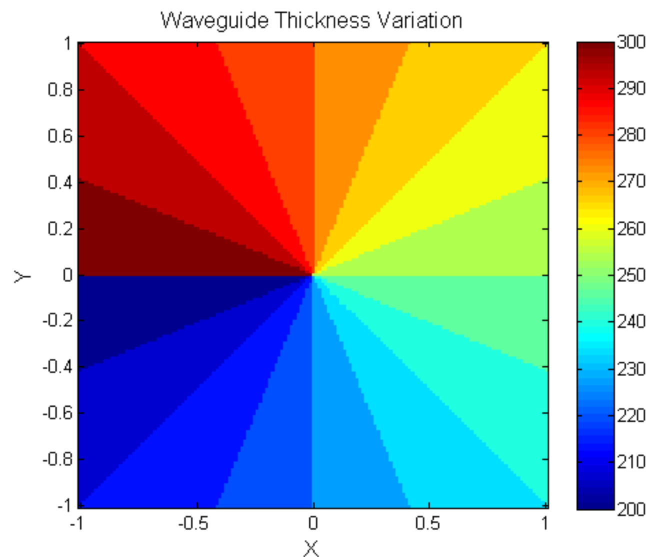


Figure 3.35. Waveguide thickness variation used to simulate the beam profiles for the azimuthally varying GMRF with a silicon oxide SWG and a silicon nitride waveguide layer. X and Y axis are in millimeters, color scale is in nanometers.

The waveguide thickness variation shown in Figure 3.35 was used to simulate the transmitted beam profiles shown in Figure 3.36. The transmitted beam profiles are shown for four different wavelengths: 1514.2 nm, 1537.7 nm, 1560.0 nm, and 1581.2 nm. The beam profiles shown are the taken at the device. The input was a Gaussian beam

with a beam waist of radius 1.2 mm located 15 cm before the azimuthally varying GMRF. The method used to calculate these profiles is the same as in Section 3.3.3. These profiles show that with increasing wavelength the pie wedge in the transmission profile rotates counter-clockwise around the center of the device, assuming that the direction of propagation is into the page.

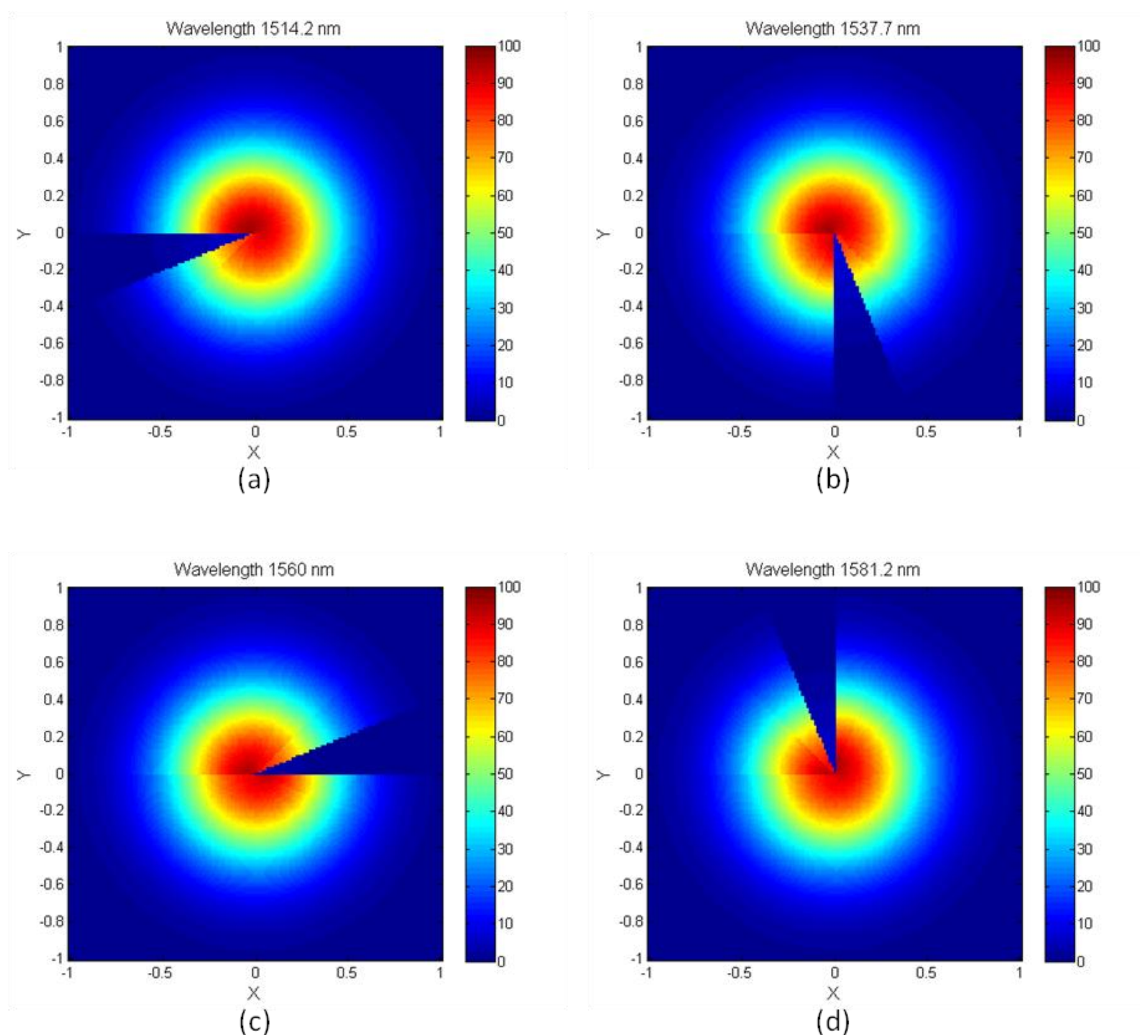


Figure 3.36. Simulated transmitted beam profiles for an azimuthally varying GMRF. X and Y axis are in arbitrary units. The waveguide and SWG are constructed from silicon nitride and silicon oxide, respectively. The incident wavelengths are: (a) 1530 nm, (b) 1550 nm, (c) 1570 nm, and (d) 1590 nm.

3.4.4. Silicon Nitride SWG with Silicon Nitride Waveguide Layer

The previous section focused on a typical three-material system for the general GMRF structure. The fabrication of that design would require a material deposition to occur after the three-dimensional waveguide structure is patterned and etched. While this is not necessarily an issue in microfabrication, it does create additional fabrication steps that can be avoided. If the SWG layer is comprised of Silicon Nitride and the waveguide layer is also comprised of Silicon Nitride, then fabrication steps could be eliminated. This device will be comprised of only partially etched Silicon Nitride layer on a Fused Silica substrate. Figure 3.37 shows a three-dimensional representation of a conventional GMRF that is comprised of only two materials.

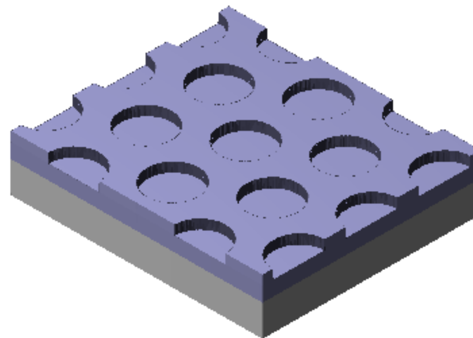

Figure 3.37. Schematic drawing of a Hexagonal GMRF with a SWG and waveguide of the same material

Figure 3.38 shows the RCWA simulation results for the non-varying structure shown above. The lattice constant is 1.15 μm, the SWG thickness is 150 nm, the waveguide thickness is 195 nm, and the hole radii in the SWG are 350 nm. This structure gives a polarization independent reflection and transmission spectra with resonance located at 1550 nm with a linewidth of 12 nm. This linewidth is noticeable larger than previous GMRFs discussed. In this structure, silicon nitride is used as the material for

the SWG as opposed to silicon oxide in the previous examples. This has the effect of increasing the index contrast of the SWG, which increases the linewidth of the GMRF.

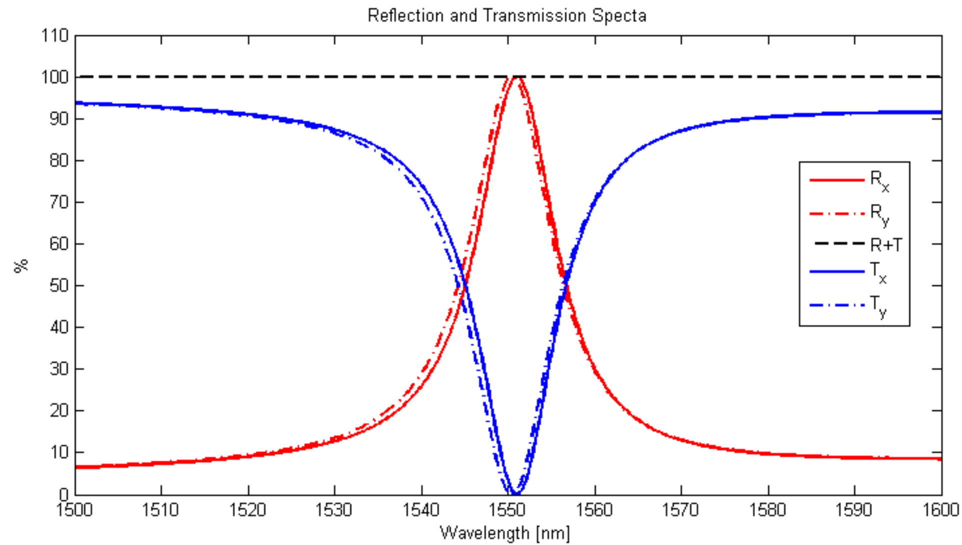


Figure 3.38. RCWA simulation results for a hexagonal GMRF. The SWG lattice constant is 1.15 µm with hole radii of 350 nm and is etched 150 nm into the Silicon Nitride layer. The waveguide layer is 195nm.

As discussed previously, the thickness of the waveguiding layer can be used to vary the resonance conditions of the GMRF. Figure 3.39 shows the effects of varying the silicon nitride thickness for this structure. As the thickness of the waveguide layer is increased from 160 nm to 260, the resonance location is increased from 1520 nm to 1604 nm at a linear rate of 0.84 nm/nm (resonance shift/waveguide thickness change).

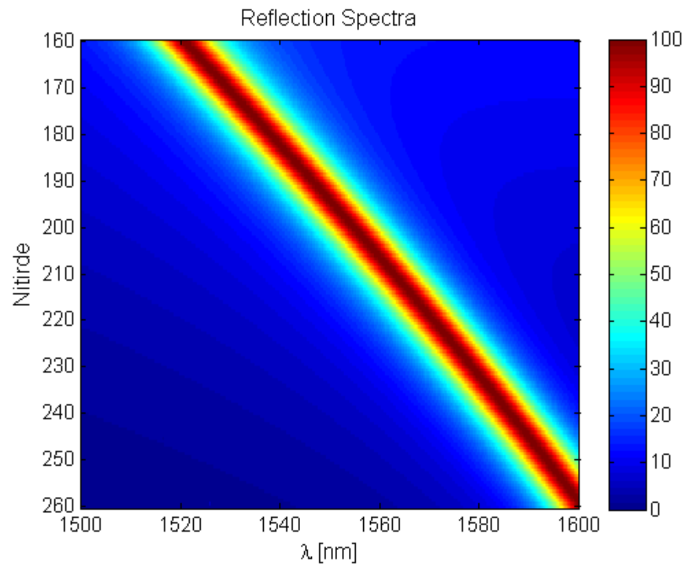


Figure 3.39. RCWA simulation results for a Hexagonal GMRF. The SWG lattice constant is 1.15 µm with hole radii of 350 nm and is 150 nm thick. The waveguide layer is varied between 160 nm and 260nm. The SWG and waveguide layers are both Silicon Nitride

Figure 3.40 shows a conceptual drawing of an azimuthally varying GMRF made using only single nitride on a fused silica substrate. Figure 3.41 shows the specific waveguide thickness variation used to simulate the beam profiles. The variation of the waveguide layer is 160 nm to 260 nm. The variation in the waveguide layer is continuous, and represents the type of structure that would be fabricated using analog lithography.

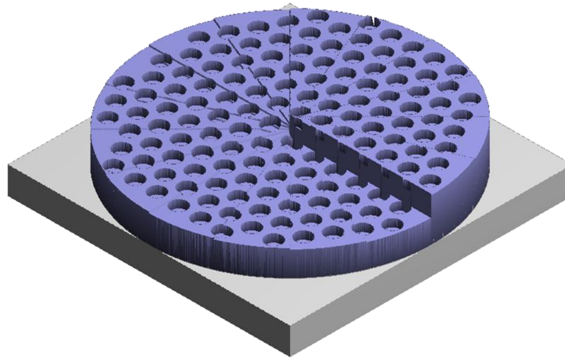

Figure 3.40. Schematic drawing of a GMRF with an azimuthally varying waveguide layer. The SWG and the waveguide are the same material.

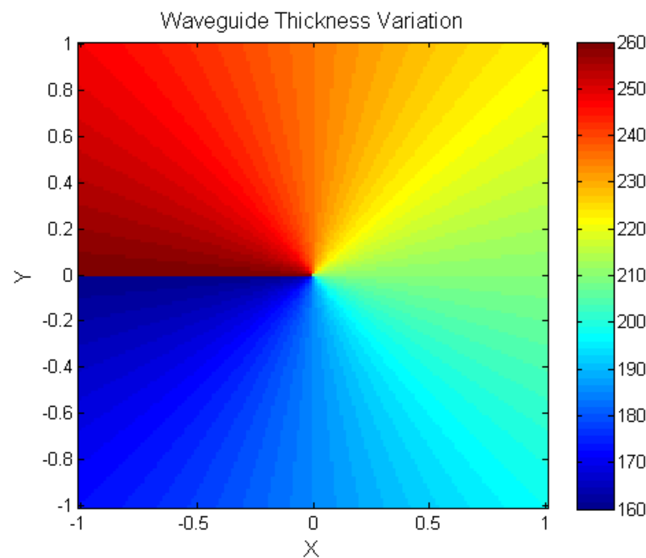


Figure 3.41. Waveguide thickness variation used to simulate the beam profiles for the azimuthally varying silicon nitride only GMRF. X and Y axis are in millimeters, color scale is in nanometers.

The waveguide thickness variation shown in Figure 3.41 was used to simulate the transmitted beam profiles shown in Figure 3.42. The transmitted beam profiles are shown for four different wavelengths: 1530 nm, 1550 nm, 1570 nm, and 1590 nm. The beam profiles shown are located in the plane of the device. The input was a Gaussian beam with a beam waist of radius 1.2 mm located 15 cm before the azimuthally varying

GMRF. The method used to calculate these profiles is the same as in Section 3.3.3. These profiles show that with increasing wavelength, the pie wedge in the transmission profile rotates counter-clockwise around the center of the device, assuming that the direction of propagation is into the page.

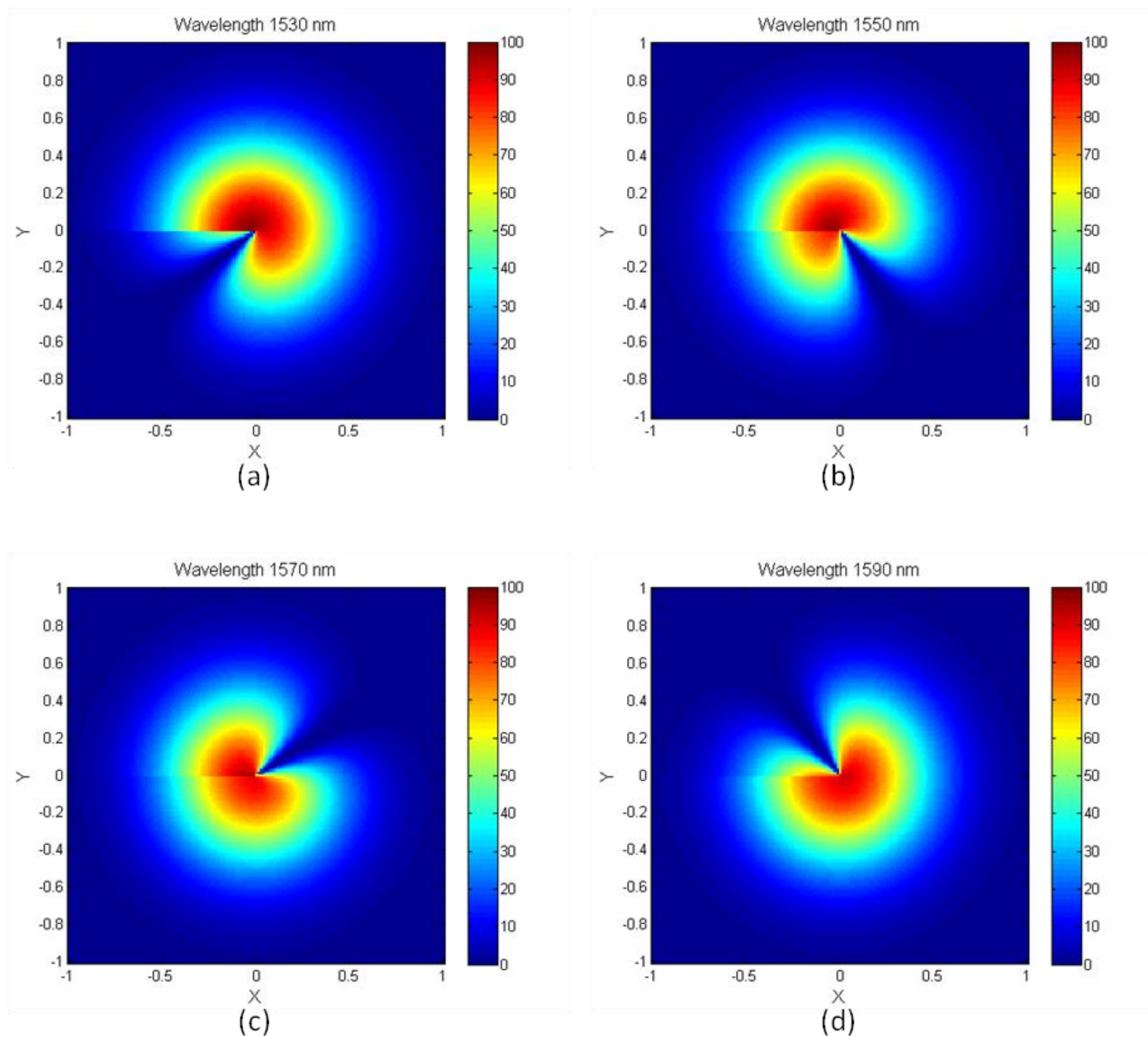


Figure 3.42. Simulated transmitted beam profiles for an azimuthally varying GMRF. X and Y axis are in arbitrary units. The waveguide and SWG are both constructed from silicon nitride. The incident wavelengths are: (a) 1530 nm, (b) 1550 nm, (c) 1570 nm, and (d) 1590 nm.

# CHAPTER 4: CONCLUSION

Guided mode resonance filters (GMRF) represent a class of optical filters that can be utilized to create spectrally and spatially varying optical elements. It has been shown that through modulation of the structural properties of these devices that spatially varying reflection and transmission profiles can be created. Conventional and novel microfabrication techniques were employed to create the novel three-dimensional structures necessary for these types of devices.

Chapter 1 discussed the theory behind the operation of GMRFs, as well as the effects the structural parameters can have on the spectral characteristics of these devices. Chapter 2 described the technologies and techniques that were utilized to create not only GMRFs but also the three-dimensional structures required to realize a space variant GMRFs. In Chapter 3, the design, fabrication, and testing of GMRF devices was explained. In addition, it was shown that spatial modulation of the fill-fraction of the subwavelength grating (SWG) could be used to realize an azimuthally varying GMRF. This type of variation is not possible with convention graded reflectivity mirrors, and space variant GMRFs offer a possible alternative method of realizing a spatially varying reflectivity.

The method used to create a spatially varying fill-fraction grating limits the range of periods that can be modulated. Also, the effect of the fill-fraction variation has on the resonance conditions is limited; the resonance conditions have a limited dynamic range

with this type of variation. As a result of these limitations, an alternate method of creating a spatially varying GMRF was proposed. This involved the modulation of the waveguiding layer of a GMRF to create the spatially varying resonance conditions. It was shown that varying the thicknesses of the higher refractive index material used in the GMRFs in this dissertation does create varying resonance conditions. The effects of these variations were simulated, and these simulations were used to predict potential beam profiles that could be created using this technique.

Future research would focus on the realization of a spatially varying waveguide layer in a GMRF to create a spectrally and spatially varying optical element. Previous researchers have shown that spatially varying phase profiles can be created using space variant GMRFs [32, 33]. In addition, it may be possibly to create a spatially varying GMRF to control the phase-front and amplitude of the reflection and transmission profiles. In Chapter 1, it was shown the type of lattice structure used determines the polarization properties of a GMRF. Therefore, an optical element that controls the phase-front, amplitude profile, and polarization field could be created by using a three-dimensionally varying guided mode resonance filter.

# BIBLIOGRAPHY

1. Wang, S.S. and R. Magnusson, *Theory and applications of guided-mode resonance filters.* Appl. Opt., 1993. **32**(14): p. 2606-2613.

2. Wood, R.W., On a Remarkable Case of Uneven Distribution of Light in a Diffraction Grating Spectrum. Proceedings of the Physical Society of London, 1902. **18**(1): p. 269.

3. Rayleigh, L., *On the Dynamical Theory of Gratings.* Proceedings of the Royal Society of London. Series A, Containing Papers of a Mathematical and Physical Character, 1907. **79**(532): p. 399-416.

4. Hessel, A. and A.A. Oliner, *A New Theory of Wood's Anomalies on Optical Gratings.* Appl. Opt., 1965. **4**(10): p. 1275-1297.

5. Wang, S.S., R. Magnusson, J.S. Bagby, and M.G. Moharam, *Guided-mode resonances in planar dielectric-layer diffraction gratings.* J. Opt. Soc. Am. A, 1990. **7**(8): p. 1470-1474.

6. Sharon, A., D. Rosenblatt, A.A. Friesem, H.G. Weber, H. Engel, and R. Steingrueber, *Light modulation with resonant grating-waveguide structures.* Opt. Lett., 1996. **21**(19): p. 1564-1566.

7. Tibuleac, S. and R. Magnusson, *Reflection and transmission guided-mode resonance filters.* J. Opt. Soc. Am. A, 1997. **14**(7): p. 1617-1626.

8. Rosenblatt, D., A. Sharon, and A.A. Friesem, *Resonant grating waveguide structures.* Quantum Electronics, IEEE Journal of, 1997. **33**(11): p. 2038-2059.

9. Magnusson, R., D. Shin, and Z.S. Liu, *Guided-mode resonance Brewster filter.* Opt. Lett., 1998. **23**(8): p. 612-614.

10. Sharon, A., D. Rosenblatt, and A.A. Friesem, *Resonant grating-waveguide structures for visible and near-infrared radiation.* J. Opt. Soc. Am. A, 1997. **14**(11): p. 2985-2993.

11. Shokooh-Saremi, M. and R. Magnusson, *Wideband leaky-mode resonance reflectors: Influence of grating profile and sublayers.* Opt. Express, 2008. **16**(22): p. 18249-18263.

12. Norton, S.M., T. Erdogan, and G.M. Morris, *Coupled-mode theory of resonant-grating filters.* J. Opt. Soc. Am. A, 1997. **14**(3): p. 629-639.

13. Moharam, M.G. and T.K. Gaylord, *Rigorous coupled-wave analysis of planar-grating diffraction.* J. Opt. Soc. Am., 1981. **71**(7): p. 811-818.

14. Peng, S. and G.M. Morris, Efficient implementation of rigorous coupled-wave analysis for surface-relief gratings. J. Opt. Soc. Am. A, 1995. **12**(5): p. 1087-1096.

15. Peng, S. and G.M. Morris, *Resonant scattering from two-dimensional gratings.* J. Opt. Soc. Am. A, 1996. **13**(5): p. 993-1005.

16. Magnusson, R. and Y. Ding, *MEMS tunable resonant leaky mode filters.* Photonics Technology Letters, IEEE, 2006. **18**(14): p. 1479-1481.

17. Song, H.Y., S. Kim, and R. Magnusson, *Tunable guided-mode resonances in coupled gratings.* Opt. Express, 2009. **17**(26): p. 23544-23555.

18. Chang, A.S.P., K.J. Morton, T. Hua, P.F. Murphy, W. Wei, and S.Y. Chou, *Tunable Liquid Crystal-Resonant Grating Filter Fabricated by Nanoimprint Lithography.* Photonics Technology Letters, IEEE, 2007. **19**(19): p. 1457-1459.

19. Brückner, F., S. Kroker, D. Friedrich, E.-B. Kley, and A. Tünnermann, *Widely tunable monolithic narrowband grating filter for near-infrared radiation.* Opt. Lett., 2011. **36**(4): p. 436-438.

20. Shokooh-Saremi, M. and R. Magnusson, Particle swarm optimization and its application to the design of diffraction grating filters. Opt. Lett., 2007. **32**(8): p. 894-896.

21. Niederer, G., H.P. Herzig, J. Shamir, H. Thiele, M. Schnieper, and C. Zschokke, *Tunable, Oblique Incidence Resonant Grating Filter for Telecommunications.* Appl. Opt., 2004. **43**(8): p. 1683-1694.

22. Szeghalmi, A., M. Helgert, R. Brunner, F. Heyroth, U. Gösele, and M. Knez, *Tunable Guided-Mode Resonance Grating Filter.* Advanced Functional Materials, 2010. **20**(13): p. 2053-2062.

23. Brundrett, D.L., E.N. Glytsis, T.K. Gaylord, and J.M. Bendickson, *Effects of modulation strength in guided-mode resonant subwavelength gratings at normal incidence.* J. Opt. Soc. Am. A, 2000. **17**(7): p. 1221-1230.

24. Lemarchand, F., A. Sentenac, and H. Giovannini, Increasing the angular tolerance of resonant grating filters with doubly periodic structures. Opt. Lett., 1998. **23**(15): p. 1149-1151.

25. Sentenac, A. and A.-L. Fehrembach, *Angular tolerant resonant grating filters under oblique incidence.* J. Opt. Soc. Am. A, 2005. **22**(3): p. 475-480.

26. Fehrembach, A.L., O. Gauthier-Lafaye, K.C.S. Yu, A. Monmayrant, S. Bonnefont, E. Daran, P. Arguel, F. Lozes-Dupuy, and A. Sentenac, *Measurement and modeling of 2D hexagonal resonant-grating filter performance.* J. Opt. Soc. Am. A, 2010. **27**(7): p. 1535-1540.

27. Fehrembach, A.-L., D. Maystre, and A. Sentenac, *Phenomenological theory of filtering by resonant dielectric gratings.* J. Opt. Soc. Am. A, 2002. **19**(6): p. 1136-1144.

28. Mehta, A.A., R.C. Rumpf, Z.A. Roth, and E.G. Johnson, *Guided Mode Resonance Filter as a Spectrally Selective Feedback Element in a Double-Cladding Optical Fiber Laser.* Photonics Technology Letters, IEEE, 2007. **19**(24): p. 2030-2032.

29. Sims, R.A., C.C. Willis, P. Kadwani, T.S. McComb, L. Shah, V. Sudesh, Z.A. Roth, M.K. Poutous, E.G. Johnson, and M. Richardson. *Spectral Beam Combining of 2 μm Tm Fiber Laser Systems*. 2010: Optical Society of America.

30. Sims, R.A., Z. Roth, T. McComb, L. Shah, V. Sudesh, P. Menelaos, E. Johnson, and M.C. Richardson. *Guided Mode Resonance Filters as Stable Line-Narrowing Feedback Elements for Tm Fiber Lasers*. 2009: Optical Society of America.

31. Sims, R.A., Z.A. Roth, C.C.C. Willis, P. Kadwani, T.S. McComb, L. Shah, V. Sudesh, M. Poutous, E.G. Johnson, and M. Richardson, *Spectral narrowing and stabilization of thulium fiber lasers using guided-mode resonance filters.* Opt. Lett., 2011. **36**(5): p. 737-739.

32. Fattal, D., J. Li, Z. Peng, M. Fiorentino, and R.G. Beausoleil, *Flat dielectric grating reflectors with focusing abilities.* Nat Photon, 2010. **4**(7): p. 466-470.

33. Lu, F., F.G. Sedgwick, V. Karagodsky, C. Chase, and C.J. Chang-Hasnain, *Planar high-numerical-aperture low-loss focusing reflectors and lenses using subwavelength high contrast gratings.* Opt. Express, 2010. **18**(12): p. 12606-12614.

34. Ganesh, N., A. Xiang, N.B. Beltran, D.W. Dobbs, and B.T. Cunningham, *Compact wavelength detection system incorporating a guided-mode resonance filter.* Applied Physics Letters, 2007. **90**(8).

35. Boye, R.R., R.W. Ziolkowski, and R.K. Kostuk, *Resonant Waveguide-Grating Switching Device with Nonlinear Optical Material.* Appl. Opt., 1999. **38**(24): p. 5181-5185.

36. Szeghalmi, A., E.B. Kley, and M. Knez, *Theoretical and Experimental Analysis of the Sensitivity of Guided Mode Resonance Sensors.* The Journal of Physical Chemistry C, 2010. **114**(49): p. 21150-21157.

37. Fang, Y., A.M. Ferrie, N.H. Fontaine, J. Mauro, and J. Balakrishnan, *Resonant Waveguide Grating Biosensor for Living Cell Sensing*. Biophysical Journal, 2006. **91**(5): p. 1925-1940.

38. Lavigne, P., N. McCarthy, and J.-G. Demers, *Design and characterization of complementary Gaussian reflectivity mirrors.* Appl. Opt., 1985. **24**(16): p. 2581-2586.

39. Piegari, A., Coatings with graded-reflectance profile: conventional and unconventional characteristics. Appl. Opt., 1996. **35**(28): p. 5509-5519.

40. Cusumano, P., G. Lullo, A. Mangione, and C. Arnone, *Graded Reflectivity Micromirror Arrays.* Appl. Opt., 2002. **41**(1): p. 143-147.

41. Morin, M., *Graded reflectivity mirror unstablelaser resonators.* Optical and Quantum Electronics, 1997. **29**(8): p. 819-866.

42. Duplain, G., P.G. Verly, J.A. Dobrowolski, A. Waldorf, and S. Bussiére, *Graded-reflectance mirrors for beam quality control in laser resonators.* Appl. Opt., 1993. **32**(7): p. 1145-1153.

43. Emiliani, G., A. Piegari, S. De Silvestri, P. Laporta, and V. Magni, *Optical coatings with variable reflectance for laser mirrors.* Appl. Opt., 1989. **28**(14): p. 2832-2837.

44. Madou, M.J., Fundamentals of microfabrication : the science of miniaturization. 2nd ed. 2002, Boca Raton: CRC Press. 723 p.

45. Pitchumani, M., H. Hockel, W. Mohammed, and E.G. Johnson, *Additive lithography for fabrication of diffractive optics.* Appl. Opt., 2002. **41**(29): p. 6176-6181.

46. Johnson, E.G., M. Pitchumani, H. Hockel, J. Sung, W. Mohammed, and L. Vaissie. *Additive lithography for micro-optics fabrication*. 2002: Optical Society of America.

47. Pitchumani, M., J. Brown, W. Mohammed, and E.G. Johnson, *Micro-Optic Fabrication with Subdomain Masking.* Appl. Opt., 2004. **43**(8): p. 1676-1682.

48. Pitchumani, M., W.S. Mohammed, H. Hockel, and E.G. Johnson. *Presculpting of photoresists using additive lithography*. 2004. San Jose, CA, USA: SPIE.

49. Sung, J., H. Hockel, and E.G. Johnson, Analog micro-optics fabrication by use of a two-dimensional binaryphase-grating mask. Opt. Lett., 2005. **30**(2): p. 150-152.

50. Wong, A.K.-K., *Resolution enhancement techniques in optical lithography*. Tutorial texts in optical engineering v. TT 47. 2001, Bellingham, Wash.: SPIE Press. xvii, 214 p.

51. O'Neil, A.T., I. MacVicar, L. Allen, and M.J. Padgett, *Intrinsic and Extrinsic Nature of the Orbital Angular Momentum of a Light Beam.* Physical Review Letters, 2002. **88**(5): p. 053601.

52. Swartzlander, J.G.A., *The Optical Vortex Lens.* Opt. Photon. News, 2006. **17**(11): p. 39-43.

53. Gahagan, K.T. and J.G.A. Swartzlander, *Optical vortex trapping of particles.* Opt. Lett., 1996. **21**(11): p. 827-829.

54. Grier, D.G., *A revolution in optical manipulation.* Nature Photonics, 2003. **424**(6950): p. 810-816.

55. Fürhapter, S., A. Jesacher, S. Bernet, and M. Ritsch-Marte, *Spiral phase contrast imaging in microscopy.* Opt. Express, 2005. **13**(3): p. 689-694.

56. Lee, J.H., G. Foo, E.G. Johnson, and G.A. Swartzlander, Jr., *Experimental Verification of an Optical Vortex Coronagraph.* Physical Review Letters, 2006. **97**(5): p. 053901.

57. Barbieri, N., M. Weidman, G. Katona, M. Baudelet, Z. Roth, E. Johnson, G. Siviloglou, D. Christodoulides, and M. Richardson, *Double helical laser beams based on interfering first-order Bessel beams.* J. Opt. Soc. Am. A, 2011. **28**(7): p. 1462-1469.

58. Srinivasan, P., Z.A. Roth, M.K. Poutous, and E.G. Johnson, *Novel method for the fabrication of spatially variant structures.* Journal of Micro/Nanolithography, MEMS and MOEMS, 2009. **8**(1): p. 013010-8.

59. Poutous, M.K., A.J. Pung, P. Srinivasan, Z.A. Roth, and E.G. Johnson, *Polarization selective, graded-reflectivity resonance filter, using a space-varying guided-mode resonance structure.* Opt. Express, 2010. **18**(26): p. 27764-27776.

60. Srinivasan, P., M.K. Poutous, Z.A. Roth, Y.O. Yilmaz, R.C. Rumpf, and E.G. Johnson, *Spatial and spectral beam shaping with space-variant guided mode resonance filters.* Opt. Express, 2009. **17**(22): p. 20365-20375.

61. Poutous, M.K., Z. Roth, K. Buhl, A. Pung, R.C. Rumpf, and E.G. Johnson. Correlation of fabrication tolerances with the performance of guided-mode-resonance micro-optical components. in Proceedings of the SPIE. 2009. San Jose, CA, USA: SPIE.

# APPENDIX A: PARAMETERS OF VARIOUS FABRICATION PROCESSES

This Appendix provides specific details related to the fabrication process of the micro-optical devices in this dissertation.

Table A.1 lists the process parameters used to deposit silicon nitride ($Si_xN_y$) on fused silica substrates using the STS PECVD system. During the fabrication process of a conventional GMRF, the dielectric layers a first deposited using the STS PECVD. The silicon nitride layer serves as the waveguide layer for the devices in this dissertation.

Table A.1. Process Parameters for Silicon Nitride ($Si_xN_y$) deposition on STS PECVD.

| Parameter | Value |
|---|---|
| Chamber Pressure | 900 mT |
| HF(High Frequency) RF Power | 20 W |
| 2% Silane (SiH4) Flow Rate | 1980 sccm |
| Ammonia (NH3) Flow Rate | 55 sccm |
| Deposition Rate | 0.15833 nm/s |
| Deposition Rate | 9.5 nm/min |

Table A.2 lists the process parameters used to deposit silicon oxide ($SiO_x$) on fused silica substrates using the STS PECVD system. The devices presented in this dissertation, typically use silicon dioxide as the material for the SWG.

Table A.2. Process Parameters for Silicon Oxide ($SiO_x$) deposition on STS PECVD.

| Parameter | Value |
|---|---|
| Chamber Pressure | 900 mT |
| HF(High Frequency) RF Power | 30 W |
| 2% Silane ($SiH_4$) Flow Rate | 400 sccm |
| Nitrous Oxide ($N_2O$) Flow Rate | 1420 sccm |
| Deposition Rate | 0.75 nm/s |
| Deposition Rate | 45 nm/min |

Table A.3 lists the parameters used to pattern the SWG in photoresist. This is typically done after dielectric layers are deposited. The exposure dose will vary

depending on the thicknesses of the dielectric layers used due to reflections from the thin film stack.

Table A.3. Lithographic process parameters for patterning the SWG.

| Parameter | Value |
|---|---|
| Photoresist | Shipley S-1805 |
| Target Thickness | 350 nm |
| Spin Speed | 3500 rpms |
| Post Application Bake | 60s @ 115$^{o}$C |
| Exposure Dose (g-line GCA Stepper) | ~1.0s |
| Post Exposure Bake | 60s @ 115$^{o}$C |
| Developer | MF-319 |
| Development | 60s Immersion |
| Hardbake (Preparation for Etch) | 60s @ 115$^{o}$C |

Table A.4 lists the recipe used in the Unaxis Versaline High Powered Oxide Etcher to etch the subwavelength gratings (SWG) in this dissertation. The selectivity is the ration of the etch rate in silicon oxide to the photoresist used. In this case, it is the etch rate of the SWG pattern in silicon oxide.

Table A.4. Process Parameters for standard SWG etch using Unaxis Versaline Hi Powered Oxide Ether.

| Parameter | Value |
|---|---|
| Chamber Pressure | 10 mTorr |
| ICP Power | 500 W |
| RF (RIE) Power | 50 W |
| $O_2$ Flow Rate | 70 sccm |
| $CHF_3$ Flow Rate | 5 sccm |
| Helium Cooling Pressure | 4500 mT |
| Selectivity (FS:PR) | ~1.1:1.0 |
| Fused Silica Etch Rate | 170 nm/min |

Table A.5 lists the process parameters used to achieve a low selectivity etch. This is the type of etch that is needed to achieve a spatial variation in the waveguide layer of a GMRF.

Table A.5. Process Parameters Low-Selectivity etch using Unaxis Versaline Hi Powered Oxide Ether.

| Parameter | Value |
| --- | --- |
| Chamber Pressure | 10 mTorr |
| ICP Power | 800 W |
| RF (RIE) Power | 80 W |
| $O_2$ Flow Rate | 30 sccm |
| $CHF_3$ Flow Rate | 20 sccm |
| Helium Cooling Pressure | 6000 mT |
| Selectivity (FS:PR) | 0.2:1.0 |

# APPENDIX B: MATLAB CODE

This appendix lists the MATLAB scripts that were used in the various simulations used in this dissertation. The following script is an example of the code used to simulate the effects of the structural parameters on the spectra of a one-dimensional GMRF. This code does not include the rigorous coupled wave analysis (RCWA) kernel.

```
%%EFFECT OF STRUCTURAL PARAMETERS OF GMRF ON RESONANCE
%% INITIALIZE MATLAB
close all; clc;
clear all;

%% SAVE AS..
savedata=0;
if savedata==1;
    [filename, floc] = uiputfile('*.mat', 'Save Resulting Workspace
as');
    fname=[floc, filename] %#ok<NOPTS>
    save(fname)
end

%% UNITS
microns = 1;             %Determine Scale of Units
global micrometers nanometers deg nm um mm cm meters degrees;
%#ok<NUSED>
zunits(microns)          %Assign Units

%% INITIAL PARAMETERS
% SOURCE
LAMBDA = [1450:0.05:1700] * nanometers;
NLAM    = length(LAMBDA);
ginc    = [0;0;1];
theta=0;
phi=0;
% NUMBER OF HARMONICS
M=11;
N=1;

% BASELINE GMR/DEVICE/MATERIAL PARAMETERS
[nSiN, nSiO2, nFS]=index_disp(1.550);
nAir  = 1.0;
nSi=3.518;
a  = 1000 * nanometers;
r  = 500 * nm;
dN = 250 * nanometers;
dO = 500 * nanometers;
dE = 500 * nm;
Lx=a;
r=a/2;
% GRID PARAMETERS
```

```
Nx = 32;
Ny = 1;

%% SETUP LOOP
ParV='Waveguide Thickness [nm]';
V1   = 200 * nanometers;
V2   = 500 * nanometers;
NPV = 151;
PV=linspace(V1,V2,NPV);
SFV=1/nm;

%% INITIALIZE MATRICES
Rmat=zeros(NPV,NLAM);
Rmaty=zeros(NPV,NLAM);
phRX=zeros(NPV,NLAM);
phRY=zeros(NPV,NLAM);
phTX=zeros(NPV,NLAM);
phTY=zeros(NPV,NLAM);

%% RUN LOOP
tic
for vcnt=1:NPV
    % DEVICE PARAMETERS
    dN=PV(vcnt);     %Horizontal or X parameter
    [ginc TE TM]=findVectorsTPf(theta, phi);
    Ly=Ny/Nx*Lx;
    if dE > dO
        [gratN]=make1Dgrat(Nx,Ny,Lx,r,nAir^2,nSiO2^2);
        GRAT.ER = gratN;
        [gratN]=make1Dgrat(Nx,Ny,Lx,r,nAir^2,nSiN^2);
        GRAT.ER(:,:,2) = gratN;
        GRAT.ER(:,:,3) = nSiN^2;
        GRAT.DZ = [dO dE-dO dO+dN-dE]';

    elseif dE<dO
        [gratN]=make1Dgrat(Nx,Ny,Lx,r,nAir^2,nSiO2^2);
        GRAT.ER = gratN;
        GRAT.ER(:,:,2) = nSiO2^2;
        GRAT.ER(:,:,3) = nSiN^2;
        GRAT.DZ = [dE dO-dE dN]';

    else
        [gratN]=make1Dgrat(Nx,Ny,Lx,r,nAir^2,nSiO2^2);
        GRAT.ER = gratN;
        GRAT.ER(:,:,2) = nSiN^2;
        GRAT.DZ = [dE dN]';
    end

    % SET MATERIALS AT REFLECTION AND TRANSMISSION REGIONS
    GRAT.er1 = nAir^2;
    GRAT.er2 = nFS^2;

    % GRAT
    GRAT.t1  = [Lx;0];
    GRAT.t2  = [0;Ly];
```

```
    GRAT.res = [Lx Ly] ./ [Nx Ny];

    % BUILD SOURCE 'kinc' INPUT ARGUMENT
    K0             = 2*pi./LAMBDA;
    SRC.KINC       = K0*sqrt(GRAT.er1)*ginc(1);
    SRC.KINC(2,:)  = K0*sqrt(GRAT.er1)*ginc(2);
    SRC.KINC(3,:)  = K0*sqrt(GRAT.er1)*ginc(3);
    SRC.KINC       = [  SRC.KINC       ,  SRC.KINC ];
    SRC.EP         = [  TM(1)*ones(1,NLAM)   , TE(1)*ones(1,NLAM);  ...
                        TM(2)*ones(1,NLAM)   , TE(2)*ones(1,NLAM);  ...
                        TM(3)*ones(1,NLAM)   , TE(3)*ones(1,NLAM)   ];

    % OPTS
    OPTS.disp = 0;
    OPTS.M    = M;
    OPTS.N    = N;
    OPTS.Ra   = 1;
    OPTS.Ta   = 1;
    OPTS.Rde   =1;
    OPTS.Tde =1;

    % RUN SIM
    [R,T] = rcwa3d_rep(GRAT,SRC,OPTS);
    clc;
    toc
    Percent_Done=(vcnt)/(NPV)*100
    % RECORD RESULTS
    M0=(M+1)/2;
    N0=(N+1)/2;
    rxx(1,1:NLAM)=R.x(M0,N0,1:NLAM);
    tyy(1,1:NLAM)=T.y(M0,N0,NLAM+1:2*NLAM);
    txx(1,1:NLAM)=T.x(M0,N0,1:NLAM);
    tyy(1,1:NLAM)=T.y(M0,N0,NLAM+1:2*NLAM);
    ryy(1,1:NLAM)=R.y(M0,N0,NLAM+1:2*NLAM);
    RX(1,1:NLAM)=R.de(M0,N0,1:NLAM);
    RY(1,1:NLAM)=R.de(M0,N0,NLAM+1:2*NLAM);
    TX(1,1:NLAM)=T.de(M0,N0,1:NLAM);
    TY(1,1:NLAM)=T.de(M0,N0,NLAM+1:2*NLAM);
    phRX(vcnt,:)=angle(rxx);
    phRY(vcnt,:)=angle(ryy);
    phTX(vcnt,:)=angle(txx);
    phTY(vcnt,:)=angle(tyy);

    Rmat(vcnt,:)   = RX*100;
    Rmaty(vcnt,:)  = RY*100;
    [LWIDTH,WPEAK,PMAX]=findFWHM(LAMBDA,RX*100);
    FWHM(vcnt)=LWIDTH;
    WP(vcnt)=WPEAK;
    Pwr(vcnt)=PMAX;
    [LWIDTHY,WPEAKY,PMAXY]=findFWHM(LAMBDA,RY*100);
    FWHMY(vcnt)=LWIDTHY;
    WPY(vcnt)=WPEAKY;
    PwrY(vcnt)=PMAXY;
end
clc;
toc
```

```
%% TIMESTAMP
TDV=clock;
yyyy=num2str(TDV(1));
mim=num2str(TDV(2));
dd=num2str(TDV(3));
hh=num2str(TDV(4));
ms=num2str(TDV(5));
ss=num2str(TDV(6));

dstamp=[hh,ms,'_',mim,dd,yyyy];

%% SAVE DATA
if savedata==1
    fname %#ok<NOPTS>
    save(fname)
end
%% PLOT SPECTRA
figure(1)
subplot(2,1,1)
imagesc(LAMBDA/nm,PV*SFV,abs(Rmaty))
xlabel('\lambda [nm]')
ylabel(ParV)
title('Reflection Spectra TE')
colorbar
caxis([0 100])
subplot(2,1,2)
imagesc(LAMBDA/nm,PV*SFV,abs(Rmat))
xlabel('\lambda [nm]')
ylabel(ParV)
title('Reflection Spectra TM')
colorbar
caxis([0 100])

%% PLOT FWHM
figure(2)
plot(PV*SFV,FWHM,'r','LineWidth',2); hold on;
plot(PV*SFV,FWHMY,'b','LineWidth',2);
ylabel('FWHM [nm]')
xlabel(ParV)
title('Linewidth of Resonances')
legend('TM','TE')
```

The following is the code used to determine the full-width half-maximum linewidth of the reflection peaks of the GMRFs modeled.

```
function [LWIDTH,WPEAK,PMAX,wmax]=findFWHM(LAMBDA,SPECTRA)

%This code only works for 1D Specta Matrices with a single Peak
%SPECTRA NEEDS TO BE IN UNITS OF % AND NOT A FRACTIONAL VALUE.

if length(LAMBDA) == length(SPECTRA)
```

```
    L=length(LAMBDA);
else
    error('LAMBDA and SPECTRA must be same length')
end

[PMAX,wmax]=max(SPECTRA);
WPEAK=LAMBDA(wmax);
HM=PMAX/2;
if wmax<2
    wmax=3;
    pw=1;   %stop condition for left-hand side half-peak
    pf=1;
else
    pw=0;
    pf=0;
end
LHW=0;

%% Find Spectral location of the left-side half maximum value
Lcnt=wmax;
while pw==0;
    Lcnt=Lcnt-1;
    P1=SPECTRA(Lcnt-1);
    W1=LAMBDA(Lcnt-1);
    P2=SPECTRA(Lcnt);
    W2=LAMBDA(Lcnt);
    W=abs(W2-W1);
    P=abs(P2-P1);
    if P2>HM
        if P1<=HM
            LHW=W2-W/P*(P2-HM);
            pw=1;
        end
    end
    if Lcnt<=3
        pw=1;
        LHW=0;
    end
end
RHW=LHW;

%% Find Spectral location of the right-side half maximum value
Rcnt=wmax;
while pf==0
    P1=SPECTRA(Rcnt-1);
    W1=LAMBDA(Rcnt-1);
    P2=SPECTRA(Rcnt);
    W2=LAMBDA(Rcnt);
    W=abs(W2-W1);
    P=abs(P2-P1);
    if P1>=HM
        if P2<HM
            RHW=W1-W/P*(P1-HM);
            pf=1;
        end
    end
```

```
    Rcnt=Rcnt+1;
    if Rcnt>=L-2
        if pf==0
            RHW=LHW;
            pf=1;
        end
    end
end

LWIDTH=RHW-LHW

%% Perform some checks so that returned value makes sense.
SWIDTH=abs(LAMBDA(L)-LAMBDA(1))
if LWIDTH>0.85*SWIDTH
    disp('a')
    LWIDTH=0;
end
if wmax<2
    disp('b')
    LWIDTH=0;
end
if PMAX<40
    LWIDTH=0;
end
```

The following MATLAB script was used to simulate the reflected and transmitted beam profiles of the space variant GMRF.

```
%% SIMULATE REFLECTED AND TRANSMITTED BEAMS FOR SPACE VARIANT FILL
FRACTION %GMRF

%% INITIALIZE MATLAB
close all; clc;
clear all;

%% SAVE AS..
savedata=0;
if savedata==1;
    [filename, floc] = uiputfile('*.mat', 'Save Resulting Workspace
as');
    fname=[floc, filename] %#ok<NOPTS>
    save(fname)
end


%% UNITS
microns = 1;            %Determine Scale of Uniters
global micrometers nanometers deg nm um mm cm meters degrees;
%#ok<NUSED>
zunits(microns)         %Assign Units

%% INITIAL PARAMETERS
```

```
% SOURCE
LAMBDA = [1546.2 1547.0 1548.6 1549.4] * nanometers;
NLAM    = length(LAMBDA);
ginc    = [0;0;1];
theta=0;
phi=0;
% NUMBER OF HARMONICS
M=7;
N=7;

% BASELINE GMR/DEVICE/MATERIAL PARAMETERS
[nSiN, nSiO2, nFS]=index_disp(1.550);
nAir  = 1.0;
nSi=3.518;
a  = 1150 * nanometers;
r  = 415 * nm;
dN = 375 * nanometers;
dO = 240 * nanometers;
dE = 170 * nm;
dNa = 0.97*375 * nanometers;
dOa = 0.97*240 * nanometers;
dEa = 170 * nm;
% GRID PARAMETERS
Nx = 1151;
Ny = round(sqrt(3)*Nx);

%% SETUP LOOP
ParV='Percent [%]';
V1  = 290 * nanometers;
V2  = 420 * nanometers;
NPV = 101;
PV=linspace(V1,V2,NPV);
SFV=1/nm;

%% INITIALIZE MATRICES
Rmat=zeros(NPV,NLAM);
Rmaty=zeros(NPV,NLAM);
phRX=zeros(NPV,NLAM);
phRY=zeros(NPV,NLAM);
phTX=zeros(NPV,NLAM);
phTY=zeros(NPV,NLAM);

%% RUN LOOP

tic
for vcnt=1:NPV
    % DEVICE PARAMETERS
    r=PV(vcnt);     %Horizontal or X parameter

    [ginc TE TM]=findVectorsTPf(theta, phi);
    Lx=a;
    Ly=sqrt(3)*Lx;
    if dE > dO
        [gratN]=hexcircgrat(Nx,Ny,Lx,Ly,r,nAir^2,nSiO2^2);
        GRAT.ER = gratN;
        [gratN]=hexcircgrat(Nx,Ny,Lx,Ly,r,nAir^2,nSiN^2);
```

```
    GRAT.ER(:,:,2) = gratN;
    GRAT.ER(:,:,3) = nSiN^2;
    GRAT.DZ = [dO dE-dO dO+dN-dE]';

elseif dE<dO
    [gratN]=hexcircgrat(Nx,Ny,Lx,Ly,r,nAir^2,nSiO2^2);
    GRAT.ER = gratN;
    GRAT.ER(:,:,2) = nSiO2^2;
    GRAT.ER(:,:,3) = nSiN^2;
    GRAT.DZ = [dE dO-dE dN]';

else
    [gratN]=hexcircgrat(Nx,Ny,Lx,Ly,r,nAir^2,nSiO2^2);
    GRAT.ER = gratN;
    GRAT.ER(:,:,2) = nSiN^2;
    GRAT.DZ = [dE dN]';
end

% SET MATERIALS AT REFLECTION AND TRANSMISSION REGIONS
GRAT.er1 = nAir^2;
GRAT.er2 = nFS^2;

% GRAT
GRAT.t1  = [Lx;0];
GRAT.t2  = [Lx/2;Ly/2];
GRAT.res = [Lx Ly] ./ [Nx Ny];

% BUILD SOURCE 'kinc' INPUT ARGUMENT
K0            = 2*pi./LAMBDA;
SRC.KINC      = K0*sqrt(GRAT.er1)*ginc(1);
SRC.KINC(2,:) = K0*sqrt(GRAT.er1)*ginc(2);
SRC.KINC(3,:) = K0*sqrt(GRAT.er1)*ginc(3);
SRC.KINC      = [  SRC.KINC       ,   SRC.KINC ];
SRC.EP        = [  TM(1)*ones(1,NLAM)   , TE(1)*ones(1,NLAM);  ...
                   TM(2)*ones(1,NLAM)   , TE(2)*ones(1,NLAM);  ...
                   TM(3)*ones(1,NLAM)   , TE(3)*ones(1,NLAM)   ];

% OPTS
OPTS.disp = 0;
OPTS.M    = M;
OPTS.N    = N;
OPTS.Ra   = 1;
OPTS.Ta   = 1;
OPTS.Rde   =1;
OPTS.Tde =1;

% RUN SIM
[R,T] = rcwa3d_rep(GRAT,SRC,OPTS);
clc;
toc
Percent_Done=(vcnt)/(NPV)*100

% RECORD RESULTS
M0=(M+1)/2;
N0=(N+1)/2;
```

```
    rxx(1,1:NLAM)=R.x(M0,N0,1:NLAM);
    rxy(1,1:NLAM)=R.y(M0,N0,1:NLAM);
    rxz(1,1:NLAM)=R.z(M0,N0,1:NLAM);
    tyy(1,1:NLAM)=T.y(M0,N0,NLAM+1:2*NLAM);
    txt(1,1:NLAM)=T.t(1:NLAM);
    tyt(1,1:NLAM)=T.t(NLAM+1:2*NLAM);
    rxt(1,1:NLAM)=R.t(1:NLAM);
    ryt(1,1:NLAM)=R.t(NLAM+1:2*NLAM);
    txx(1,1:NLAM)=T.x(M0,N0,1:NLAM);
    tyy(1,1:NLAM)=T.y(M0,N0,NLAM+1:2*NLAM);
    ryy(1,1:NLAM)=R.y(M0,N0,NLAM+1:2*NLAM);
    RX(1,1:NLAM)=R.de(M0,N0,1:NLAM);
    RY(1,1:NLAM)=R.de(M0,N0,NLAM+1:2*NLAM);
    TX(1,1:NLAM)=T.de(M0,N0,1:NLAM);
    TY(1,1:NLAM)=T.de(M0,N0,NLAM+1:2*NLAM);
    phRX(vcnt,:)=angle(rxx);
    phRY(vcnt,:)=angle(ryy);
    phTX(vcnt,:)=angle(txx);
    phTY(vcnt,:)=angle(tyy);

    Rmat(vcnt,:)  = RX*100;
    Rmaty(vcnt,:) = RY*100;
    Tmat(vcnt,:)  = TX*100;
    Tmaty(vcnt,:) = TY*100;
    Rmat2(vcnt,:)  = rxt*100;
    Rmat2y(vcnt,:) = ryt*100;
    [LWIDTH,WPEAK,PMAX]=findFWHM(LAMBDA,RX*100);
    FWHM(vcnt)=LWIDTH;
    WP(vcnt)=WPEAK;
    Pwr(vcnt)=PMAX;
    [LWIDTHY,WPEAKY,PMAXY]=findFWHM(LAMBDA,RY*100);
    FWHMY(vcnt)=LWIDTHY;
    WPY(vcnt)=WPEAKY;
    PwrY(vcnt)=PMAXY;

end
clc;
toc

%% TIMESTAMP
TDV=clock;
yyyy=num2str(TDV(1));
mim=num2str(TDV(2));
dd=num2str(TDV(3));
hh=num2str(TDV(4));
ms=num2str(TDV(5));
ss=num2str(TDV(6));

dstamp=[hh,ms,'_',mim,dd,yyyy];

%% SAVE DATA
if savedata==1
    fname %#ok<NOPTS>
    save(fname)
end
```

```
%%
THETA=linspace(0,2*pi,101);
Rm=-
0.000002645*(THETA*180/pi).^3+0.001843*(THETA*180/pi).^2+0.01111*(THETA
*180/pi)+294.27;
WP2=interp1(PV,WP,Rm*nm);

%% PLOT RESULTS

axes('FontSize',14)

subplot(2,2,1)
imagesc(LAMBDA/nm,PV*SFV,(Rmat))
xlabel('\lambda [nm]','Fontsize',14)
ylabel(ParV,'Fontsize',14)
title('R_x','Fontsize',14)
colorbar
caxis([0 100])

subplot(2,2,2)
imagesc(LAMBDA/nm,PV*SFV,phRX)
xlabel('\lambda [nm]','Fontsize',14)
ylabel(ParV,'Fontsize',14)
title('R_x Phase','Fontsize',14)
colorbar
caxis([-pi pi])

subplot(2,2,3)
imagesc(LAMBDA/nm,PV*SFV,abs(Rmaty))
xlabel('\lambda [nm]','Fontsize',14)
ylabel(ParV,'Fontsize',14)
title('R_y','Fontsize',14)
colorbar
caxis([0 100])

subplot(2,2,4)
imagesc(LAMBDA/nm,PV*SFV,phRY)
xlabel('\lambda [nm]','Fontsize',14)
ylabel(ParV,'Fontsize',14)
title('R_y Phase','Fontsize',14)
colorbar
caxis([-pi pi])

figure(2)
axes('Fontsize',11)
imagesc(LAMBDA/nm,PV*SFV,abs(Rmaty))
xlabel('\lambda [nm]','Fontsize',12)
ylabel(ParV,'Fontsize',12)
title('Reflection Spectra','Fontsize',12)
colorbar
caxis([0 100])

figure(8)
plot(THETA/deg,WP2*1000,'b','LineWidth',2);
ylabel('Resonance \lambda [nm]')
```

```
xlabel('Azimuth Angle [\circ]')
title('Location of Resonances')
xlim([0 360])
set(gca,'XTick',0:60:360)

%%%%%%%%%%%%%%%%%%%%%%%%%%%%%%%%%%%%%%%%%%%%%%%%%%%%%%%%%%%%%%%%%%%%%%%%
%%%%
%%%%%%%%%%%%%%%%%%%%%%%%%%%%%%%%%%%%%%%%%%%%%%%%%%%%%%%%%%%%%%%%%%%%%%%%
%%%%
%%                  MAKE BEAMS
%% Set up Grids
Rout=2.5*mm;
Nb=501;

xy=linspace(-Rout,Rout,301);
[X Y]= meshgrid(xy, xy);
[THETA RHO]=cart2pol(X,Y);
theta=linspace(0,2*pi,Nb);
THETA=THETA+pi;
THETA=rot90(THETA,3);
%Rm already exists it is 1D
RH1D=-
0.000002645*(theta*180/pi).^3+0.001843*(theta*180/pi).^2+0.01111*(theta
*180/pi)+294.27;
RH2D=-
0.000002645*(THETA*180/pi).^3+0.001843*(THETA*180/pi).^2+0.01111*(THETA
*180/pi)+294.27;

%% Choose Wavelengths

NL1=1;
NL2=2;
NL3=3;
NL4=4;
L1=LAMBDA(NL1)
L2=LAMBDA(NL2)
L3=LAMBDA(NL3)
L4=LAMBDA(NL4)


%% Make 1D Azimuthal Prodile Wavelength #1

RL1=Rmat(:,NL1);
RL2=Rmat(:,NL2);
RL3=Rmat(:,NL3);
RL4=Rmat(:,NL4);
TL1=100-RL1;
TL2=100-RL2;
TL3=100-RL3;
TL4=100-RL4;
V1DR1 = interp1(PV,RL1,RH1D*nm,'cubic');
V1DT1 = interp1(PV,TL1,RH1D*nm,'cubic');
V1DR2 = interp1(PV,RL2,RH1D*nm,'cubic');
V1DT2 = interp1(PV,TL2,RH1D*nm,'cubic');
V1DR3 = interp1(PV,RL3,RH1D*nm,'cubic');
```

```
V1DT4 = interp1(PV,TL3,RH1D*nm,'cubic');
V1DR4 = interp1(PV,RL4,RH1D*nm,'cubic');
V1DT4 = interp1(PV,TL4,RH1D*nm,'cubic');

figure(31)
plot(theta/deg,V1DR1,'b','LineWidth',2);hold on;
plot(theta/deg,V1DR2,'r','LineWidth',2);
plot(theta/deg,V1DR3,'g','LineWidth',2);
plot(theta/deg,V1DR4,'k','LineWidth',2); hold off;
ylabel('[%]')
xlabel('Azimuth Angle [\circ]')
title('R & T vs Azimuth')
xlim([0 360])
set(gca,'XTick',0:60:360)
legend(num2str(L1/nm),num2str(L2/nm),num2str(L3/nm),num2str(L4/nm))


%% 2D figure
z=5*cm;
w0=1.2*mm;

[BEAM, Rz, Wz, qz]=GuassBeam2D(X,Y,z,w0,LAMBDA(1));

V2DR1 = interp1(PV,RL1,RH2D*nm,'cubic');
V2DT1 = interp1(PV,TL1,RH2D*nm,'cubic');
V2DR2 = interp1(PV,RL2,RH2D*nm,'cubic');
V2DT2 = interp1(PV,TL2,RH2D*nm,'cubic');
V2DR3 = interp1(PV,RL3,RH2D*nm,'cubic');
V2DT3 = interp1(PV,TL3,RH2D*nm,'cubic');
V2DR4 = interp1(PV,RL4,RH2D*nm,'cubic');
V2DT4 = interp1(PV,TL4,RH2D*nm,'cubic');

RB1=(abs(BEAM).^2).*V2DR1;
RB2=(abs(BEAM).^2).*V2DR2;
RB3=(abs(BEAM).^2).*V2DR3;
RB4=(abs(BEAM).^2).*V2DR4;
TB1=(abs(BEAM).^2).*V2DT1;
TB2=(abs(BEAM).^2).*V2DT2;
TB3=(abs(BEAM).^2).*V2DT3;
TB4=(abs(BEAM).^2).*V2DT4;

%% figures
figure(321)
subplot(311)
imagesc(xy,xy,THETA)
set(gca,'YDir','normal')
axis image
subplot(312)
imagesc(xy,xy,V2DT1.*abs(BEAM))
set(gca,'YDir','normal')
axis image
subplot(313)
imagesc(xy,xy,V2DT2)
set(gca,'YDir','normal')
axis image
```

```
%% 2d profiles transmitted
xa2=xy/mm;
ya2=xy/mm;
figure(422)
imagesc(xa2,ya2,TB1)
ttext=['Tranmitted Beam \lambda =',num2str(LAMBDA(1)*1000),' nm'];
title(ttext,'Fontsize',12)
colorbar
axis xy
axis image
caxis([0 100])
xlabel('X [mm]','Fontsize',12)
ylabel('Y [mm]','Fontsize',12)

figure(424)
imagesc(xa2,ya2,TB2)
ttext=['Transmitted Beam \lambda =',num2str(LAMBDA(2)*1000),' nm'];
title(ttext,'Fontsize',12)
colorbar
axis xy
axis image
caxis([0 100])
axis xy
xlabel('X [mm]','Fontsize',12)
ylabel('Y [mm]','Fontsize',12)

figure(426)
imagesc(xa2,ya2,TB3)
ttext=['Transmitted Beam \lambda =',num2str(LAMBDA(3)*1000),' nm'];
title(ttext,'Fontsize',12)
colorbar
axis xy
axis image
caxis([0 100])
axis xy
xlabel('X [mm]','Fontsize',12)
ylabel('Y [mm]','Fontsize',12)

figure(428)
imagesc(xa2,ya2,TB4)
ttext=['Reflected Beam \lambda =',num2str(LAMBDA(4)*1000),' nm'];
title(ttext,'Fontsize',12)
colorbar
axis xy
axis image
caxis([0 100])
xlabel('X [mm]','Fontsize',12)
```